technische universität dortmund

Fakultät Physik

**Arbeit zur Erlangung des akademischen Grades
Master of Science**

Prompt Atmospheric Muons:
An Analysis Concept with IceCube

Ludwig Neste
geboren in Castrop-Rauxel

2023

astroparticle physics

Fakultät Physik
Technische Universität Dortmund

Abstract

Cosmic rays are highly energetic charged particles accelerated in the cosmos. When interacting with nuclei from Earth's atmosphere, cosmic rays start a cascade of particles called an *extensive air shower*. Muons in these air showers are predominantly created by decaying pions or kaons, they are called *conventional* muons. Heavier, short-lived mesons produce the *prompt* component of the muon flux. Prompt muons follow the cosmic ray energy spectrum, whereas conventional muons have a steeper spectrum. So far, the prompt component has never been significantly verified to exist in experiments and this thesis aims to provide a concept to change that. A method to distinguish the prompt component in the air shower simulation software `CORSIKA7` is developed. Consistent spectra compared to numerical solutions of the cascade equations via MCEq are reported. The open source `python` package PANAMA is developed, providing modern utilities for `CORSIKA7`, including its parallel execution, prompt-tagging and weighting with modern cosmic ray flux models. Using PANAMA, properties and definitions of the prompt component of the muon flux are explored. The proposed analysis is applied to a toy Monte Carlo study for the *IceCube* detector, located deep inside the glacier ice at the South Pole in Antarctica. The Monte Carlo study with ten years of IceCube data results in a 5σ discovery potential of $(3.24 \pm 0.13)\,\%$ of the prompt muon flux predicted by the hadronic interaction model `SIBYLL2.3d`.

Kurzfassung

Kosmische Strahlung besteht aus hochenergetischen geladenen Teilchen, die im Kosmos beschleunigt werden. Bei der Wechselwirkung mit Atomkernen der Atmosphäre lösen kosmische Strahlen eine Kaskade von Teilchen aus, die als *Luftschauer* bezeichnet wird. Die Myonen in diesen Luftschauern werden überwiegend durch zerfallende Pionen und Kaonen erzeugt, die zum *konventionellen* Myonfluss beitragen. Schwerere Mesonen wie die *D*-Mesonen tragen durch ihre Kurzlebigkeit zur *prompten* Komponente des Myonflusses bei. Prompte Myonen folgen dem Energiespektrum der kosmischen Strahlung, während konventionelle Myonen ein steileres Spektrum aufweisen. Bislang wurde die prompte Komponente in Experimenten noch nicht signifikant nachgewiesen. Diese Arbeit schlägt eine Analyse zu diesem Zweck vor. Dazu wird eine Methode zur Identifizierung der prompten Komponente in der Luftschauer-Simulationssoftware `CORSIKA7` entwickelt und übereinstimmende Spektren mit numerischen Lösungen der Kaskadengleichungen mittels MCEq werden präsentiert. Das quelloffene `python`-Paket PANAMA wird entwickelt, das eine Schnittstelle zu `CORSIKA7` darstellt. Diese beinhaltet die parallele Ausführung, das Identifizieren der prompten Myonen, sowie die Gewichtung mit modernen Modellen für das Primärteilchenspektrum. Mit PANAMA werden Eigenschaften und Definitionen der prompten Komponente des Myonenflusses untersucht. Die vorgeschlagene Analyse wird als eine Test-Monte-Carlo-Studie für das *IceCube*-Observatorium ausgeführt. Die Monte-Carlo-Studie für 10 Jahre IceCube-Laufzeit verspricht ein 5σ Entdeckungspotential von $(3.24 \pm 0.13)\,\%$ des prompten Flusses, der vom hadronischem Interaktionsmodell `SIBYLL2.3d` vorhergesagt wird.

Contents

1 Introduction

Astroparticle physics studies particles of astrophysical origin, how they are produced and what they teach about the cosmos. Victor Hess pioneered the field in 1912, when he discovered that the natural radiation, which was then believed to originate only from unstable elements inside the earth, rises on balloon flights with higher altitude. The radiation must therefore come from outer space — he discovered *Cosmic Rays (CRs)* [Hes12]. For that he was awarded the Nobel Prize in 1936.

Since Hess' discovery of cosmic rays, the field of astroparticle physics underwent massive progress, especially in the last decades. With IceCube's discovery of astrophysical neutrinos in 2013 [IC13] and the discovery of gravitational waves by the LIGO and VIRGO experiments in 2015 [LIG16] the era of *multimessenger astronomy* arrived. Humankind is able to observe the universe for the first time without relying on electromagnetic radiation. At last, we start seeing a more complete picture of the most extreme processes in the universe.

The precise origin of CRs themselves remains an open question in current research [Alv+19]. At the highest energies, cosmic rays are so rare that they require tremendous detector areas to observe even a few of them in years. For example, the Pierre Auger Observatory with its $\approx 3000\,\mathrm{km}^2$ observed only 2600 CRs above 32 EeV in 17 years [PA22]. Such detector areas are unfeasible to construct in space. Thus, CR-detectors for the highest energies rely on secondary detection of CRs through particle cascades inside Earth's atmosphere.

The complex interactions inside these CR-induced *extensive air showers (EASs)* need to be understood to interpret the data from a CR observatory. Recently, evidence of systematic underestimation of the number of muons in EAS simulations accumulate — this is known as the *muon puzzle* [Alb+22]. The muon itself is a source of mysteries for particle physicists [MG23; Aoy+20], over eight decades after its unexpected discovery in cosmic radiation [NA37]. The muon puzzle demonstrates the complicated interplay of particle- and astrophysics: To simulate air showers, particle-collisions in Earth's atmosphere must be understood through measurements of particle-collisions in accelerator experiments. The muon puzzle is expected to originate from the parameter space unprobed by current accelerator experiments such as the Large Hadron Collider (LHC) at CERN. Accelerator data shows that most of these muons come from the decay of pions and kaons. At very high energies above 1 PeV muons from decays of other, heavier mesons like charmed or unflavored mesons are expected to dominate, they are called *prompt* muons. These charmed and unflavored mesons are only observed inside accelerators experiments, so far. The discovery of the *prompt* component of the muon flux would prove their existence inside EAS. To this day, no significant discovery of a prompt component has

been reported. To change this, this thesis develops a method for an analysis with the world's largest detector *IceCube*.

The IceCube neutrino observatory displayed in Figure 1.1 was primarily built to detect astrophysical neutrinos, as the name suggests. Located deep inside the antarctic glacier, IceCube successfully achieved its objective: It detected astrophysical neutrinos [IC13], resolved two neutrino point sources [IC18; MM18; IC22] and recently measured neutrinos from our home galaxy [IC23a]. IceCube effectively started the era of neutrino astronomy. But most measured events by IceCube are not neutrino induced. Most of the events are atmospheric muons. High energy muons can penetrate the $1.5\,\text{km}$ of ice and reach the $1\,\text{km}^3$ volume, which is instrumented with 5160 Digital Optical Modules (DOMs) [IC17]. A DOM contains a photomultiplier, which measures Cherenkov light from energy losses of the particles inside the detector. Hence, IceCube is also very suited as a high energy muon detector.
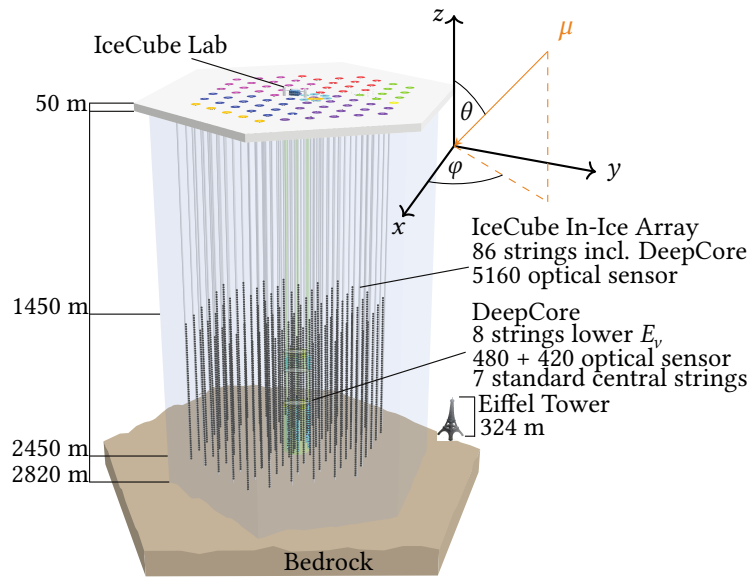

Figure 1.1: The IceCube Neutrino Observatory located deep inside the antarctic glassier ice at the South Pole is sketched. The typical coordinate system including the zenith angle θ as well as the azimuth angle φ is shown as well. Modified from [Rei20].

This thesis studies a possible method to verify the existence of this prompt component of the muon flux with the IceCube detector. Chapter 2 explains how muons are created in extensive air showers. Chapter 3 establishes how prompt muons can be differentiated from other muons in the current Monte Carlo (MC) EAS simulation software CORSIKA7. Chapter 4 then applies this method to a potential analysis with IceCube and reports the expected results, before Chapter 5 summarizes the results of this thesis and explains the prospects of the significant discovery of prompt leptons.

2 Cosmic Rays and Extensive Air Showers

This chapter explains the physics from Cosmic Rays (CRs) on top of Earth's atmosphere down to the *conventional* and *prompt* muons they produce in extensive air shower (EAS). This thesis develops a way to distinguish individual muons in Monte Carlo (MC) simulation as prompt or conventional. Nevertheless, it is important to understand their predicted behavior from a theoretical point of view. While MC simulations track individual particles and their interaction, in theory the central quantity to communicate the abundance of particles is the *flux ϕ*, which is defined as the number N of particles passing through an area A, per time t, per solid angle Ω

$$\phi = \frac{\mathrm{d}N}{\mathrm{d}A\,\mathrm{d}\Omega\,\mathrm{d}t}.$$

It is commonly necessary to treat energies differently, and for that the particle flux is further expressed differentially in energy E

$$\Phi = \frac{\mathrm{d}N}{\mathrm{d}A\,\mathrm{d}\Omega\,\mathrm{d}t\,\mathrm{d}E}.$$

2.1 Cosmic Ray Flux Models

Cosmic ray particles are ionized nuclei with high energies — mostly protons (ca. 90 %) but also alpha particles (ca. 9 %) and heavier particles [GER16, p. 1]. Figure 2.1 shows their measured flux across 10 orders of magnitude in energy. Ultra high energy cosmic rays are more energetic than any human made accelerated particle. The highest energy cosmic ray ever observed, the so called *Oh-My-God particle*, had $(320 \pm 90)\,\mathrm{EeV}$ of energy. It was observed by the *Fly's Eye* fluorescence camera in Utah in 1991 [Bir+95]. Their origin and acceleration-mechanism is the driving question in the field of astroparticle physics and despite large progress in the last decade, these questions remain only partially answered [Hal22]. While the exact acceleration-mechanisms remain illusive, models like Fermi acceleration of first and second kind [Fer49; GER16], suggest a stepwise acceleration mechanism with an energy proportional gain in each acceleration step. Fermi predicts an exponential acceleration of particles. If a constant probability of leaving the acceleration process per step is assumed, naturally a power law spectrum for cosmic rays arises

$$\Phi_{\mathrm{N}}(E_{\mathrm{N}}) = NE_{\mathrm{N}}^{-\gamma} \approx 1.7 \times 10^4 \left(\frac{E_{\mathrm{N}}}{\mathrm{GeV}}\right)^{-2.7} \frac{\mathrm{nucleons}}{\mathrm{m}^2\,\mathrm{s}\,\mathrm{sr}\,\mathrm{GeV}}. \tag{2.1}$$

The given numbers are taken from [GER16] and agree with the observed data up to $3\,\mathrm{PeV}$ to $5\,\mathrm{PeV}$. This is the simplest model for the CR flux and describes the flux in nucleons. This is
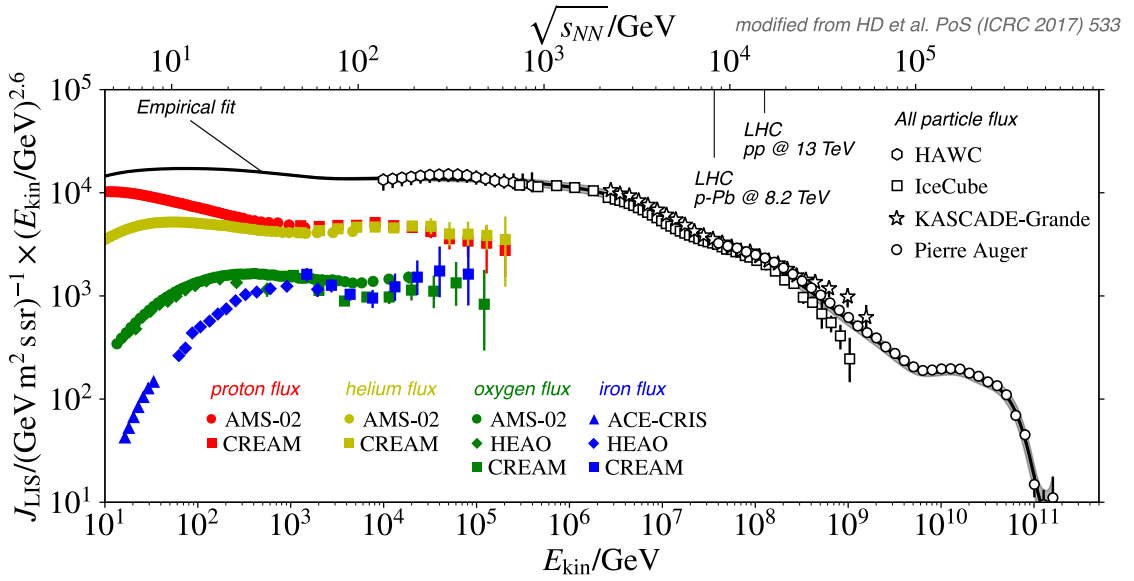
Figure 2.1: CR flux measurements and the Global Spline Fit (GSF) [Dem+17] over 11 orders of magnitude in energy is shown. The flux is given differentialy in rigidity to make the different nuclei comparable. The flux is scaled with the energy to the power of 2.6, to see the fine features in the flux curve, like the knee, the second knee and the ankle. The labels on the upper *x*-axis show the corresponding center of mass (COM) collision energies, which are the relevant energies for collider experiments. Taken from [Alb+22].

justified by the superposition model, which describes for example an alpha particle as just four nucleons[1]. Due to the power law nature of the CR flux, it is customary to scale the flux with E^{γ} when plotting it, as in Figure 2.1. This allows to see deviations from the power law and observe fine features of the spectrum.

Most of the cosmic rays in this energy region are believed to be accelerated by supernova remnants (SNRs) in our own galaxy. After 3 PeV to 5 PeV the spectral index of the CR flux changes slightly, a phenomenon named "the knee" of the spectrum. Thunman, Ingelman and Gondolo introduced a "broken" power-law model of the CR flux, modelling the "knee" [TIG96]

$$\Phi_{N}(E) = \begin{cases} 1.7 \times 10^4 \left(E_N/\text{GeV}\right)^{-2.7} & \text{for } E < 5\,\text{PeV} \\ 174 \times 10^4 \left(E_N/\text{GeV}\right)^{-3} & \text{for } E > 5\,\text{PeV} \end{cases} \frac{\text{nucleons}}{\text{m}^2\,\text{s sr GeV}}.$$

It is assumed that most CRs beyond the knee are accelerated through other mechanisms than SNRs inside our galaxy. The knee can not only be explained by the maximum energy of SNR acceleration in the galaxy, but also by less efficient confinement inside the galaxy [Alv+19]. Another primary flux parameterizations modeling the knee is the *poly-gonato*[2] model [Hör03].

---

[1] If the difference of the neutron and the proton in hadronic interactions is neglected, it can be described as four protons.

[2] Greek for "many knees".

Unlike neutrinos or electromagnetic radiation, cosmic rays do not propagate through the cosmos in straight — to be exact geodesic — lines. They are charged and are thus deflected by electric and magnetic fields in the cosmos, and are therefore not the optimal messenger to resolve the emission from a point source. Although recently evidence of a slight anisotropy of CRs above a certain energy threshold is accumulating [PA07] — probably originating from nearby galaxies — CRs are highly isotropic.

While electric fields in the cosmos are usually very weak because the net electric charge in the universe is zero, magnetic fields extend throughout whole galaxies, as in our own, the Milky Way [GER16; JF12]. The galactic magnetic field is on the order of µG and can therefore bend the charged cosmic rays. If the gyro radius of a CR is smaller than the size of the magnetic field, the CR becomes trapped. That is the reason why only the highest energetic cosmic rays can originate from other galaxies. Below a certain energy threshold, they become trapped in their source galaxy. To estimate the gyro radius r_g of a relativistic particle with energy $E = \sqrt{p^2 c^2 + m^2 c^4}$ with the charge $Z \cdot e$ and mass m, a homogeneous magnetic field of strength B is assumed. The particle moves perpendicular to the magnetic field lines. The equation of motions can then be reduced to the equality of the centrifugal and magnetic force, since they are parallel:

$$\frac{p^2}{m r_g} = Z e \frac{p}{m} B \Rightarrow r_g = \frac{p}{ZeB} = \frac{\sqrt{E^2/c^2 - m^2 c^2}}{ZeB} \overset{E \gg mc^2}{=} \frac{E}{ZeBc}.$$

This means that the particle's properties changing the gyro radius are only given by E/Z. For this reason the rigidity

$$R = \frac{pc}{Ze} \overset{E \gg mc^2}{=} \frac{E}{Ze}$$

of a particle, measured in volts, is introduced. It fully determines the strength of deflection in the magnetic field for a particle. The equation for the gyro radius then reduces to $r_g = {}^R/_{Bc}$.

The Milky Way has magnetic fields on the order of $3\,\mu G$ [GER16, p. 187] and a thickness of roughly $300\,pc$. Therefore, it traps particles on the magnitude of about $400\,PV$. If the Milky Way is somewhat typical in the universe, an extra-galactic component of CRs is expected to appear on the order of hundreds PeV in energy. They are coming from protons escaping other galaxies. And indeed, the spectral index rises around EeV — the region is named "the ankle".

The rigidity argument not only works for confinement of CRs inside the galaxy, but also for acceleration mechanisms: Iron can be accelerated to 26 times the energy of protons by the same magnetic field. Therefore, a "second knee" appears somewhere around 26 times the energy of the first knee — it is also called the "iron knee" [Alv+19]. These rigidity-dependent cutoffs were first introduced by Peters [Pet61], and they are often referred to as "Peters cycles".

There are multiple models for the CR flux describing all three features of the spectrum: the knee, the second knee and the ankle. The first are the *Gaisser-Hillas* models [Gai12] where the spectrum of a nucleon i has the form

$$\Phi_i(E) = \sum_{j=1}^{3} N_{i,j} E^{-\gamma_{i,j}} \exp\left(\frac{E}{Z_i e R_{c,j}}\right). \tag{2.2}$$

The index j enumerates three different populations, a proposal made by Hillas [Hil06]. The three populations correspond to the features described earlier, population one being of galactic origin with SNR as the accelerator, population two being a different galactic component (sometimes called "Component B") and the third population originating from outside the galaxy. The cutoffs for the three components depend on the rigidity in the last exponential term and are parametrized by the cutoff rigidity of the component $R_{c,j}$. Each population can have a different chemical composition and the zoo of elements are boiled down to five components: p, He, the C, N, O group, the Mg-Si group and Fe. These groups are roughly equidistant in $\ln(A)$, since air shower experiments are sensitive to $\ln(A)$ rather than A. The all-particle spectrum is then given by summing over the particle groups and the nucleon spectrum is given by

$$\Phi_{\mathrm{N}}(E_{\mathrm{N}}) = \sum_i A_i \cdot \Phi_i \left(A \cdot E_{\mathrm{N}} \right).$$

Gaisser's values for $\gamma_{i,j}$, $N_{i,j}$ and $R_{c,j}$ are based on "eye-ball-fits" to data. Gaisser provides two different versions. The first is named *H3a* and has non-zero flux values for all 5 particle groups in the third population, while in the second version — named *H4a* — the third population only consists of protons.

The *Global Fit* model from Gaisser, Stanev and Tilav (GST)[GST13] has the same form (eq. (2.2)) as the Gaisser-Hillas models. The difference lies in the values of the parameters, how they are obtained and that an additional sixth particle group beyond iron is introduced. As the name suggests, the GST Global Fit model uses data from many different CR experiments and fits them to the three population form. An uncertainty in the energy scale of an experiment results in a shifted normalization of the spectrum. GST applies a correction to each used experiment's data to make them comparable.

The idea to actually use data to fit the CR spectrum is taken one step further by the GSF model [Dem+17]. It is fitted to data from 11 different experiments from $10\,\mathrm{GeV}$ to $1 \times 10^{11}\,\mathrm{GeV}$ and takes systematic uncertainties into account. Very few theoretical assumptions are used: only that the fit is performed not in dependence of energy, but the logarithm of rigidity as a variable and an approximate power law around R^3. It then fits cubic B-splines to the data. The GSF model also fits the energy scale offset for the different experiments, rather than hand performing the correction. The B-Splines are freely fitted to four mass-groups of nuclei, where the dominating nucleus is selected to represent the whole group. But all other nuclei are also taken into account by restraining them to have the exact same shape as their leading nucleus, but with a different normalization, which is also fitted. The GSF has the form for each leading element

$$\Phi_i(E) = \sum_j N_{i,j} \cdot (R/\mathrm{GV})^3 \cdot B_j \left(\ln \left(R/\mathrm{GV} \right) \right).$$

Where B_j are the cubic splines and $N_{i,j}$ the normalization constants. The model is more complex than the GST model regarding the number of parameters[3], which are more than 100. To the author's knowledge, the GSF model is the only CR flux model which includes uncertainty

---

[3]Private communication with the authors.

estimations. The uncertainties are not available to the public so far, since the model is not publicly released, although the flux values can be accessed through a web interface[4].

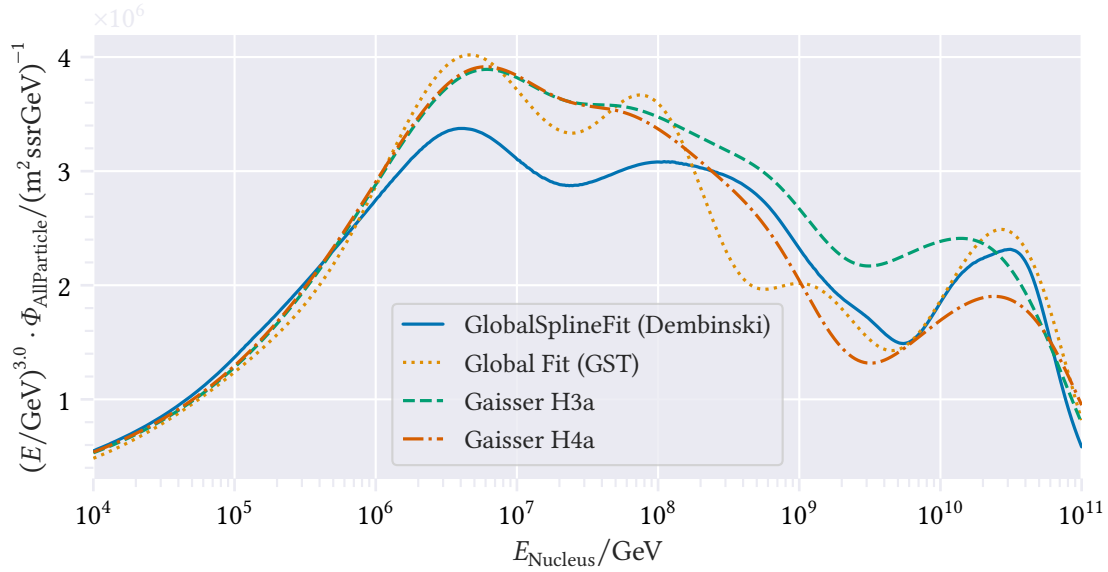The four described models are compared in Figure 2.2.

Figure 2.2: The all particle flux for four different parameterizations of the primary CR flux is shown. The spectrum is weighted with E^3 to make the differences visible. All four models are state of the art and include the knee, second knee and ankle of the CR flux. While H3a, H4a and GST all are models of the power-law with rigidity-cutoff-type, the GSF consists of splines. GST and GSF are fitted to data, while H3a and H4a are "eyeball"-fits by Thomas K. Gaisser.

The models all feature a steep cutoff around 50 EeV. This is no coincidence, since the so called Greisen-Zatsepin-Kuz'min (GZK) effect predicts a cutoff in the CR spectrum due to interactions with the cosmic microwave background (CMB) [Gre66; ZK66]. GZK pointed out that in the boosted reference frame of an extreme energy proton, the CMB becomes blue shifted to energies where photo-nuclear interaction can produce a Δ resonance, which decays into a proton and a pion, effectively decelerating the CR. If this is the case, neutrinos from the decaying pions at these characteristic energies should be measurable — they are called cosmogenic neutrinos. It "disappointingly" may also be the case that these neutrinos do not exist, nor that the GZK cutoff is relevant; the acceleration processes near our galaxy might not be energetic enough to allow acceleration to the GZK limit [ABG11].

---

[4]See www.mpi-hd.mpg.de/personalhomes/hdembins/.

2.2 Extensive Air Showers

Heitler introduced a simple model for electromagnetic cascades [Hei36]. In the Heitler model a photon (γ) splits its energy in half by e^+e^- pair-creation every splitting length λ. The electron or positron splits its energy after λ by radiating off a photon. In cascade theory distances are usually not denoted in length, but in slant depth

$$X = \int_{x_1}^{x_2} \mathrm{d}s \, \rho(\vec{r}).$$

Slant depth is measured in mass per area ($\mathrm{kg/m^2}$) and it is the governing variable of how much a particle interacts with the surrounding material, since it needs to pass through less amount of material to have the same amount of interactions, if the material is denser. In the Heitler model, the number of particles doubles after each splitting length and the energy distributes equally among them, so the energy at a slant depth X is given by

$$E(X) = \frac{E_0}{N(X)} = E_0 2^{-X/\lambda}.$$

Where E_0 is the initial energy and $N(X)$ are the number of particles at a given slant depth. Here the advantage of the slant depth becomes obvious: it's not necessary to specify through which material the electromagnetic cascade travels, the equation is equally valid for air as it is for water. Likewise, it's valid for a vertical and a horizontal air shower, which have different density profiles. The splitting stops after some critical energy $E_c \approx 87\,\mathrm{MeV}$, where the particles do not have enough energy to split any further. Despite its simplicity the Heitler model offers an intuitive explanation for many relations in an air shower without the need for complex MC simulations. It is for example obvious that the number of particles are proportional to energy of the primary particle or that the shower maximum X_{max}, the point in the shower where the most particles exist, is only logarithmically dependent on the primaries' energy.

Matthews extended Heitler's toy model to cascades initiated by a hadron and obtained equally useful approximate relations for these EASs [Mat05]. EAS initiated by a cosmic ray have a greater complexity in the hadronic shower compared to electromagnetic showers: The primary hadronic particle (most commonly a proton), interacts via the strong force with nuclei in the air and initiates a cascade with three components. The hadronic components consists of re-interacting hadrons and feeds the electromagnetic components which originates from neutral pions in the air shower which decay into two photons. When the hadrons (dominantly charged pions and kaons) decay, they produce the muonic component. The Heitler-Matthews model must therefore be more complicated than the simple Heitler model. To follow along the Heitler-Matthews model is illustrated in Figure 2.3. First, the explanation is restricted to only proton as the primary particle, before it's later extended to any kind of nucleus.

The primary proton with energy E_0 interacts with a nucleus in the air which results in the first spray of particles, which are for simplicity all assumed to be pions in this model. This
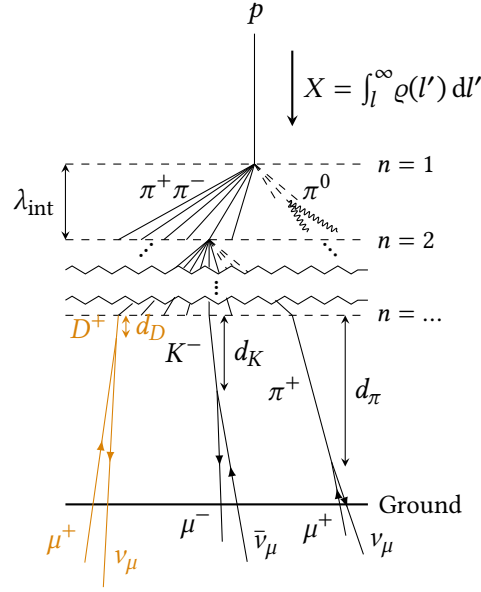
Figure 2.3: Schematic drawing of the Heitler-Matthews model for extensive air-showers [Mat05] is presented. The primary particle p enters the atmosphere and interacts with air on average in one interaction length λ_{int}, measured along the shower axis in grammage X. When the pions reach the region of the critical energy ϵ, decay starts to dominate over re-interaction, which happens on average after one decay-length d. Different particle decays are shown, and the prompt component is highlighted in orange.

interaction (like all subsequent hadronic interactions by the pions) is assumed to result in n_{tot} new particles with the same energy, of which $n_{\text{ch}} = {}^2\!/_3 n_{\text{tot}}$ particles are charged pions and ${}^1\!/_3 n_{\text{tot}}$ are neutral pions. These values are obviously approximate and could be fine tuned, but are useful for the overall argumentation. The total number of produced particles n_{prod} is usually assumed to be 15. It is shown that moderate variation in the value does not change the behavior of the model substantially [Mat05]. The neutral pions instantly decay into 2γ and their energy is transferred to the electromagnetic cascade. The energy of the hadronic component E_{had} and the energy of the electromagnetic component E_{EM} after n generations therefore results in

$$E_{\text{had}} = \left(\frac{2}{3}\right)^n E_0, \qquad E_{\text{EM}} = \left(1 - \left(\frac{2}{3}\right)^n\right) E_0.$$

These equations mean that even after a few generations, most of the energy is carried away by the electromagnetic part of the shower, for example after $n = 6$, the electromagnetic part carries $1 - \left({}^2\!/_3\right)^6 \approx 91\,\%$ of E_0. An important observable for CR experiments is the shower maximum X_{max}, which is derived in this model by assuming that it is dominated by the first electromagnetic cascade. This results in

$$X_{\text{max}}^{\text{had}} = \lambda + X_{\text{max}}^{\text{EM}}\big(E_0/(2n_{\text{tot}})\big) = \lambda + X_0 \ln\left(\frac{E_0}{2n_{\text{tot}}E_c}\right), \tag{2.3}$$

9

where λ is the hadronic interaction length and the factor of 2 accounts for the two photons produced in the pion decay. In the last step, the logarithmic dependency on E_0 of the electromagnetic X_{max} is used, as described at the beginning of this section. After the hadron H falls below some energy threshold ϵ_H, its decay becomes more likely than re-interaction with the atmosphere and they decay into muons and neutrinos, feeding the muonic part of the EAS. Since the energy is equally distributed between all particles, this happens after

$$E = \frac{E_0}{n_{\mathrm{tot}}^n} \overset{!}{=} \epsilon_\pi \Leftrightarrow n = \log_{n_{\mathrm{tot}}}\left(\frac{E_0}{\epsilon_\pi}\right) = \ln\left(\frac{E_0}{\epsilon_\pi}\right)\Big/\ln n_{\mathrm{tot}}$$

steps. The number of muons N_μ produced in the air shower with this model is therefore equivalent to the number of charged hadrons at the critical energy

$$N_\mu = \left(\frac{2}{3}n_{\mathrm{tot}}\right)^n = e^{n\ln 2/3 n_{\mathrm{tot}}} = \left(\frac{E_0}{\epsilon_\pi}\right)^\beta, \quad \text{with} \quad \beta = \frac{\ln 2/3 n_{\mathrm{tot}}}{\ln n_{\mathrm{tot}}}. \tag{2.4}$$

By plugging in reasonable values around 15 for n_{tot}, $\beta \in (0.82, 0.9)$ is estimated [GER16, p. 316].

The obtained equations can be modified to make them valid for primary nuclei consisting of A nucleons using the *superposition* model. Superposition assumes that a shower for example produced by Iron-56 with energy E_0, behaves like 56 independent proton showers with energy $E_0/56$. This assumption gains the validity from the fact that strong interactions are flavor-blind, so there is little difference in the interaction of a proton and a neutron. For the shower-maximum Equation (2.3) is modified to obtain

$$X_{\mathrm{max}}^{\mathrm{had}} = \lambda_{\mathrm{int}} + X_0 \ln\left(\frac{E_0}{A 2 n_{\mathrm{tot}}\epsilon_\pi}\right), \tag{2.5}$$

and for the muon number

$$N_\mu = A \cdot \left(\frac{E_0}{A\epsilon_\pi}\right)^\beta = A^{1-\beta}\left(\frac{E_0}{\epsilon_\pi}\right)^\beta \tag{2.6}$$

is obtained from Equation (2.4).

While these equations may not seem precise, they are important to keep in mind when working with EAS. They give a first feeling of how a cosmic ray observatory can measure different quantities, such as the primary composition and what it is sensitive to. When working with full EAS MC simulations, they provide good approximations for example the runtime, which is proportional to the number of simulated particles, which in turn is proportional to the primary energy E_0 according to the Heitler-Matthews model.

The Heitler-Matthews model also does not include Kaons or charmed hadrons, which are illustrated in Figure 2.3 in orange. The Heitler-Matthews model can also be extended by including further details like effects of the leading particles [GEV18] or the effect of all electromagnetic subshowers, not only the first one [Mon14].

2.3 The Cascade Equations

While the previous section dealt with particle cascades in a simplistic model, EAS can be treated in an analytical way using the *cascade equations*. They are formulated along the shower axis in slant depth X and treat the shower only one-dimensionally[5]. The cascade equations are a set of coupled differential equations relating the particle fluxes Φ_i of different particle types i with each other. They are given by [Fed15, p. 7][6]

$$\frac{\mathrm{d}\Phi_i(E, X)}{\mathrm{d}X} = -\left(\frac{1}{\lambda_i} + \frac{1}{d_i}\right)\Phi_i(E, X) + \sum_j \int_E^\infty \mathrm{d}E_j\, \Phi_j(E_j, X)\left(\frac{1}{\lambda_j}\frac{\mathrm{d}N_{j+\mathrm{air}\to i}}{\mathrm{d}E} + \frac{1}{d_j}\frac{\mathrm{d}N_{j\to i}}{\mathrm{d}E}\right). \quad (2.7)$$

The first "sink"-term accounts for decay of particle i in the decay length d_i and interaction with the atmosphere in interaction length λ_i. On its own the term would produce an exponential absorption form for the flux. The second term is the "source"-term and sums over all possible particle types j, which can either interact with the air to produce particle type i (accounted for by $N_{j+\mathrm{air}\to i}$), or can decay to particle type i (accounted for by $N_{j\to i}$). Since the interaction length in meter is anti-proportional to the density, the interaction length in grammage (kg/m^2)

$$\lambda_i = \frac{m}{\sigma_i^{\mathrm{air}}}$$

has no dependency to the density of the atmosphere; it cancelled out. The mean mass of the target nuclei m in the air can be expressed by $m = Am_p$ with A being the mean number of nucleons of the target and m_p the mass of the proton. The cross section of the particle with air σ_i^{air} has to be obtained by complex Quantum Chromo Dynamics (QCD)-calculations, numerical simulations or measurements. The decay length in meter is independent of the density ρ, which results in density dependency when expressed in kg/m^2

$$d_i = \rho\gamma c\tau_i = \rho\tau_i\frac{E}{mc}. \quad (2.8)$$

Where γ is the Lorentz factor of the particle and τ_i is its lifetime.

Given that there are not only a few, but at least a dozen particles that play a substantial role and the PDG lists hundreds of particles [PDG22], these equations are not easy to solve. The starting conditions $\Phi_i(E, X = 0) = \Phi_i(E)$ for the cascade equations are given by the cosmic ray flux models from Section 2.1. In the given form the cascade equations do not account for energy losses to the atmosphere, which can be introduced by a term $\partial_E\left(\mu(E)\Phi_i(E, X)\right)$.

Approximate analytical solutions to the cascade equations are derived through the spectrum weighted Z-moment method. The equations can be fully solved numerically by the python package MCEq [Fed+15].

---

[5]They can be extended to two and even three dimensions, although the solution becomes even more complicated [KFK23].

[6]Some different forms of the cascade equations exists. For example in the book of Gaisser, Engel and Resconi the form differs and some terms are neglected [GEV18, p. 107].

Consider the cascade equations eq. (2.7) for one particle type, the proton. Then the decay terms vanish, since protons do not decay[7] and left are only the interaction terms in the sink and the source, since protons can produce more protons when interacting in the atmosphere. Still, to be able to solve the equations three further assumptions are needed, which are referred to as *Approximation A*. The first one is, that the particle production term obeys *Feynman scaling*[Fey69]

$$\frac{\mathrm{d}N_{j+\mathrm{air}\to i}(E_i, E_j)}{\mathrm{d}E_i} = \frac{1}{E_j}\frac{\mathrm{d}N_{j+\mathrm{air}\to i}(x)}{\mathrm{d}x}.$$

Where $x = E_i/E_j$ is the Feynman-x, which is the ratio of the incoming to the outgoing particle energy, and thus has $0 < x < 1$. This means that the production spectrum is independent of the energy at which it occurs, as long as the ratio of the incoming and outgoing energies are the same. The second assumption is, that the interaction length λ_p is independent of energy, which is only true approximately. The third assumption is, that the energy dependency and the X-dependency factorize in the solution with a power law for energy

$$\Phi_{\mathrm{p}} = A(X)E^{-\gamma}.$$

With these approximations the cascade equations for protons reduce to

$$\begin{aligned}\frac{\mathrm{d}\Phi_{\mathrm{p}}(E_{\mathrm{p}}, X)}{\mathrm{d}X} &= -\frac{1}{\lambda_{\mathrm{p}}}\Phi_{\mathrm{p}}(E_{\mathrm{p}}, X) + \int_{E_{\mathrm{p}}}^{\infty}\mathrm{d}E'_{\mathrm{p}}\,\Phi_{\mathrm{p}}(E'_{\mathrm{p}}, X)\frac{1}{\lambda_{\mathrm{p}}}\frac{\mathrm{d}N_{\mathrm{p}+\mathrm{air}\to\mathrm{p}}}{\mathrm{d}E_{\mathrm{p}}} \\ &= \frac{\Phi_{\mathrm{p}}(E_{\mathrm{p}}, X)}{\lambda_{\mathrm{p}}}\underbrace{\left(-1 + \int_0^1\mathrm{d}x\, x^{\gamma-1}\frac{\mathrm{d}N_{\mathrm{p}+\mathrm{air}\to\mathrm{p}}(x)}{\mathrm{d}x}\right)}_{Z_{\mathrm{pp}}-1}.\end{aligned}\tag{2.9}$$

All three assumptions are used in the last step. The integral in the last step is called the spectrum weighted Z-moment, and it is similarly defined for all processes $j + \mathrm{air} \to i$ and is then labeled Z_{ij}. By introducing the attenuation length

$$\Lambda_i = \frac{\lambda_i}{1 - Z_{ii}}\tag{2.10}$$

the solution to Equation (2.9) then becomes

$$\Phi_{\mathrm{p}}(E, X) = E^{-\gamma}e^{-X/\Lambda_{\mathrm{P}}}\Phi_{\mathrm{p}}(E = E_0, X = 0).$$

Modern theory papers calculating inclusive lepton fluxes use a semi-analytical treatment, where they lower the assumptions needed in *Approximation A*: The only remaining assumption is the factorization of the X and E dependency in the solutions and not necessarily with a power-law.

---

[7]For sure at least on time scales relevant to EAS.

The basic idea is to perform the same rearranging as done in Equation (2.9), without using any assumptions from *Approximation A*. For that dependent *Z*-moment

$$Z_{ji}(E_i) = \int\limits_{E_i}^{\infty} \mathrm{d}E_j \, \frac{\Phi_j(E_j, X)}{\Phi_j(E_i, X)} \frac{\lambda_j(E_i)}{\lambda_j(E_j)} \frac{\mathrm{d}N_{j+\mathrm{air}\to i}}{\mathrm{d}E_j} = \int\limits_{0}^{1} \mathrm{d}x \, x^{\gamma(E_j)-1} \frac{\mathrm{d}N_{j+\mathrm{air}\to i}(x, E_j)}{\mathrm{d}x} \tag{2.11}$$

is introduced. The first step allows pulling out the factor of $\Phi_j(E_i)/\lambda_j(E_i)$ as in Equation (2.9) without any assumptions. The second step rewrites it in the scaling form (without assuming Feynman-scaling) and only relies on the assumption that the energy dependency factorizes. The energy dependent power law slope can be defined for any flux Φ (not only power laws) as

$$\gamma(E) = -\frac{E}{\Phi} \frac{\mathrm{d}\Phi}{\mathrm{d}E}.$$

By similarly introducing a spectrum weighted decay moment

$$Z_{ji}^d(E_i) = \int\limits_{E_i}^{\infty} \mathrm{d}E_j \, \frac{\Phi_j(E_j, X)}{\Phi_j(E_i, X)} \frac{d_j(E_i)}{d_j(E_j)} \frac{\mathrm{d}N_{j\to i}}{\mathrm{d}E_j} \tag{2.12}$$

which is proportional to the branching ratio $\mathscr{B}_{i\to j}$[8] the cascade equations are rewritten as

$$\frac{\mathrm{d}\Phi_i(E, X)}{\mathrm{d}X} = -\left(\frac{1}{\lambda_i} + \frac{1}{d_i}\right)\Phi_i(E, X) + \sum_j \left(\frac{Z_{ji}}{\lambda_j} + \frac{Z_{ji}^d}{d_j}\right)\Phi_j(E, X). \tag{2.13}$$

Here, the energy dependency of the *Z*-moments as well as the decay and interaction length are implicit. *Approximation A* is restored, if the energy dependency in the *Z*-moments is neglected. In *Approximation A* the difference of the interaction moments Z and decay moments Z^d is only that the power law over which is integrated has a spectral index, which is larger by one.

This treatment was pioneered by Reference [TIG96] and is the standard for theoretical analytical calculations of lepton fluxes. In calculations of the charmed component of lepton fluxes, this energy dependent *Z*-moment method is used [GMS15; Bha+15; Bai+22].

2.4 The Muon Flux

Before solving the cascade equations for lepton fluxes, the word "prompt" from the title of this thesis should be properly defined, since lepton fluxes in particle astrophysics are usually divided into a *prompt* and *conventional* component. While different definitions of "prompt" are explored in greater detail in Section 3.2.2, here the *conventional* part of lepton fluxes is defined as all leptons coming from pion or kaon decays, and all leptons with a different origin are *prompt*.

---

[8]This is worth mentioning, since this dependency is sometimes explicitly factored out in literature.

To obtain the muon flux with the *Z*-moment method, the cascade equations eq. (2.13) are solved by including the following terms: A primary nucleon flux (without decay) and the regeneration term, hadron fluxes with the decay, interaction and regeneration term as well as the source term from nucleon-air interaction and finally the lepton flux term with only the source term from hadron decay. The set of equations which need to be solved for that is

$$\frac{\mathrm{d}\Phi_N}{\mathrm{d}X} = -\frac{1}{\lambda_N}\Phi_N + \frac{Z_{NN}}{\lambda_N}\Phi_N,$$

$$\frac{\mathrm{d}\Phi_H}{\mathrm{d}X} = -\left(\frac{1}{\lambda_H} - \frac{Z_{HH}}{\lambda_H} + \frac{1}{d_H}\right)\Phi_H + \frac{Z_{NH}}{\lambda_N}\Phi_N,$$

$$\frac{\mathrm{d}\Phi_L}{\mathrm{d}X} = \sum_H \frac{Z_{HL}^d}{d_H}\Phi_H.$$

A proper derivation and discussion of the solution is presented in Appendix A.1, here only the solutions are given. The exact solution to the nucleon flux is

$$\Phi_N(E, X) = \Phi_N(E, X{=}0)e^{-X/\Lambda_N}.$$

Where the starting condition is the cosmic ray nucleon flux $\Phi_N(E) = \Phi_N(E, X{=}0)$ obtained by a primary flux model from Section 2.1. The hadron equation depends on d_H, which is by Equation (2.8) dependent on the density and thus the slant depth X. For this, the density of earth's atmosphere at a given slant depth $\rho(X)$ must be known. The relation is obtained from the definition of the slant depth

$$X = \int_l^\infty \mathrm{d}l'\,\rho\left(h(l')\right) = \int_h^\infty \mathrm{d}h'\,\rho\left(h'\right)\frac{\mathrm{d}l(h')}{\mathrm{d}h'}.$$

The first integral is performed in terms of the length along the shower-axis and the second integral is performed in terms of the height above earth's ground h, which is the natural variable for the density.

This integral is not analytically solvable even in the case of a simple isothermal atmosphere, with an exponential density dependency. In the flat-earth approximation $r \to \infty$ [9], the solution is

$$X = \frac{1}{\cos\theta}\int_h^\infty \mathrm{d}h'\,\rho\left(h'\right) = \frac{X_v}{\cos\theta}. \tag{2.14}$$

Restricting the solution to the simplest case of an isothermal atmosphere and making use of the ideal gas law, the vertical slant-depth X_v (zenith angle $\theta = 0$) then has the well-known exponential form of the barometric formula

$$\rho = \rho_0 e^{-h/h_0} \Rightarrow X_v = X_0 e^{-h/h_0}.$$

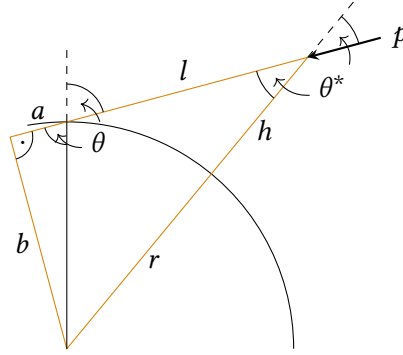[9]This is not to be confused with the flat-earth conspiracy fairy tale.

Figure 2.4: The geometry of the spherical atmosphere of Earth is outlined. Through the orange triangle the relation between θ and θ^* as well as the height h in dependence of the traveled length l, $h(l)$ is obtained.

With typical values of $h_0 = RT/Mg = 6.5\,\text{km}$ and $X_0 = 10\,300\,\text{kg/m}^2$[GER16, p. 121]. The wanted relation between the slant depth and the density is thus

$$\rho = -\frac{\mathrm{d}X_v}{\mathrm{d}h} = \frac{X_v}{h_0} = \overbrace{\frac{X_v}{X}}^{1/f(\theta,h)} \frac{X}{h_0}.$$

The *Chapman function* $f(\theta,h)$[10] is introduced, which encodes the zenith dependency and has no analytical expression, although many approximations exist [RD]. For low zenith angles and in the flat earth approximation by comparing it to Equation (2.14) it is just $f(\theta) = 1/\cos\theta$. Often, an ad-hoc approximation is obtained by ignoring the height dependency of θ^* in during integration, which results in $f(\theta,h) = 1/\cos\theta^*$.

Equation (2.8) can thus be expressed in terms of X by

$$d_H = \frac{EX\tau_H}{m_H c h_0 f(\theta,h)} = \frac{EX}{f(\theta,h)\epsilon_H}$$

where the decay constant $\epsilon_H = h_0 m_H c/\tau_H$[11] was introduced. Assuming a typical interaction depth of $X = \lambda_H$, the decay constant marks the energy at which the interaction term $1/\lambda_H$ starts dominating over the decay term $1/d_H$ for a vertical shower. The critical energy is listed for multiple hadrons in Table 2.1.

The exact solution to the hadron flux is

$$\Phi_H(E,X) = e^{-X/\Lambda_H}\frac{Z_{NH}}{\lambda_N}\Phi_N(E)\frac{X \cdot \gamma\left(\frac{\epsilon_H f}{E} + 1, \frac{X}{\Lambda_N} - \frac{X}{\Lambda_H}\right)}{\left(\frac{X}{\Lambda_N} - \frac{X}{\Lambda_H}\right)^{1+\epsilon_H f(\theta,h)/E}}. \tag{2.15}$$

---

[10]It is commonly called so in geo- and atmospheric physics.

[11]h_0 is also linear to the absolute temperature of the atmosphere. This gives rise to *seasonal variations*.

Table 2.1: The critical energies below which decay becomes dominant over interaction for different particles in an air shower are tabulated. The particles below $K^{\pm}$ are contributing to the prompt component and the last one is an example for an unflavored particle, which also contributes to the prompt component.

H	ϵ_H/GeV
$\mu^{\pm}$	1
$\pi^{\pm}$	115
$K^{\pm}$	850
$D^{\pm}$	3.7×10^7
D^0	9.9×10^7
D_s	8.4×10^7
Λ_c	2.4×10^8
$\omega(782)$	2.2×10^{17}

$\gamma(s,t)$ is the incomplete gamma function. The derivation is found in Appendix A.1. No reference to existing literature can be provided here, since the hadron flux solutions are only provided in approximation in all found literature. These high- and low energy approximations are of utmost importance to understand the *prompt* and *conventional* parts of the lepton spectra.

In the high energy limit $E \gg \epsilon_H f(\theta, h)$ [12], the solution behaves like

$$\Phi_H^{\text{high}}(E, X) = \Phi_{\text{N}}(E) \frac{Z_{\text{NH}}}{1 - Z_{\text{NN}}} \frac{\Lambda_H}{\Lambda_H - \Lambda_{\text{N}}} \left(e^{-X/\Lambda_H} - e^{-X/\Lambda_{\text{N}}} \right). \tag{2.16}$$

In the low energy limit $E \ll \epsilon_H f(\theta, h)$ the flux is given as

$$\Phi_H^{\text{low}}(E, X) = \Phi_{\text{N}}(E) e^{-X/\Lambda_N} \frac{Z_{\text{NH}}}{\lambda_{\text{N}}} \overbrace{\frac{EX}{\epsilon_H f(\theta, h)}}^{d_H}. \tag{2.17}$$

In the last step, the lepton fluxes generated by the decaying hadrons are calculated, which is analytically solvable only for the high and low energy approximations for the hadron flux. The low energy solution for the lepton flux is

$$\Phi_L^{\text{low}} = \Phi_{\text{N}}(E) \frac{Z_{NH} Z_{HL}^d}{1 - Z_{\text{NN}}} \left(1 - e^{-X/\Lambda_H} \right) \tag{2.18}$$

and the high energy limit is

$$\Phi_L^{\text{high}} = \Phi_{\text{N}}(E) \frac{Z_{NH} Z_{HL}^d}{1 - Z_{\text{NN}}} \frac{\epsilon_H f(\theta, h)}{E} \frac{\Lambda_H}{\Lambda_H - \Lambda_{\text{N}}} \left(E_1(X/\Lambda_N) - E_1(X/\Lambda_H) + \ln\left(\frac{\Lambda_H}{\Lambda_N}\right) \right). \tag{2.19}$$

---

[12]Since the zenith dependency is complicated and varies the slant depth by a factor of up to 40, usually $E \gg \epsilon_H$ is enough to specify.

Where E_1 is the exponential integral function, which is properly defined in Appendix A.1. It has to be noted, that the exact solution Equation (2.19) could not be found in any literature, so no reference or cross check for this formula is provided. In literature only the expressions for high X are usually given since $X_{\text{sealevel}} \gg \Lambda_i$ is a good approximation. The high X form of Equation (2.18) is

$$\Phi_L^{\text{low}} = \Phi_N(E) \frac{Z_{NH} Z_{HL}^d}{1 - Z_{\text{NN}}}. \tag{2.20}$$

The deviation from the exact solution at $E = 100\,\text{GeV}$ and for $H = \pi$ at typical vertical X at sea level from [GER16] is only $0.13\,\%$. The high X expression for Equation (2.19) is

$$\Phi_L^{\text{high}} = \Phi_N(E) \frac{Z_{NH} Z_{HL}^d}{1 - Z_{\text{NN}}} \frac{\epsilon_H f(\theta, h)}{E} \frac{\Lambda_H}{\Lambda_H - \Lambda_N} \ln \Lambda_H / \Lambda_N. \tag{2.21}$$

The deviation to the exact expression here is typically $0.06\,\%$.

Finally, an interpolation between the high and low energy solutions of the lepton fluxes is usually done for each hadron separately. With the observation that above (below) the characteristic energy ϵ_H the low (high) energy solution overestimates the flux, the geometric mean is a natural choice for interpolation:

$$\Phi_L(E, \theta) = \sum_H \frac{\Phi_L^{\text{high}} \Phi_L^{\text{low}}}{\Phi_L^{\text{high}} + \Phi_L^{\text{low}}} = \Phi_N(E) \sum_H \frac{\mathscr{A}_{HL}}{1 + \mathscr{B}_{HL} \frac{E}{\epsilon_H f(\theta, h)}} \tag{2.22}$$

with

$$\mathscr{A}_{HL} = \frac{Z_{NH} Z_{HL}^d}{1 - Z_{\text{NN}}}, \tag{2.23}$$

$$\mathscr{B}_{HL} = \frac{\Lambda_H - \Lambda_N}{\Lambda_H} \ln \Lambda_N / \Lambda_H. \tag{2.24}$$

The important observation, aside from numerical pre-factors, is the different behaviour of the low- and high energy solutions: The high energy limit eq. (2.21) is dependent on the Chapman function $f(\theta, h)$ and thus on the zenith angle and the atmosphere (including its temperature). The spectral index of it is the same as the CR spectral index lowered by one. The low energy solution eq. (2.20) on the other hand just follows the primary spectrum with a pre-factor. The transition for the high and low energy solution is marked by $\epsilon_H f(\theta, h)$ and differs for each hadron H. Table 2.1 shows that at typical energies for IceCube pions and kaons behave in their high-energy limit (*conventional component*) and all other particles are in their low-energy limit (*prompt component*). Because of the flatter spectral index, the prompt component becomes relevant at high energies.

All ingredients to understand the (semi-)analytical expressions for the lepton fluxes are given in current literature. It is important to understand the assumptions and limitations of the Z-moment method: It is assumed that the slant depth X and energy dependency E factorizes for all fluxes (Nucleon, Hadron, Lepton). Also, the X-dependency of d_i is taken to be approximately

linear in integration, and the true relation is later inserted by $f(\theta, h)$. And the biggest assumption which is made is the following: The unstable hadrons are only produced by themself or nucleons, but not by other hadron types. Processes like $\pi \rightarrow D \rightarrow l$ are ignored [13]. Finally, this process is only semi-analytical, since the energy-dependent Z factors must be approximated by MC simulations[14].

The full cascade equations in the form of Equation (2.13), can be written as a linear differential equation system of the first order,

$$\frac{\mathrm{d}}{\mathrm{d}X}\vec{\Phi} = \boldsymbol{M}\vec{\Phi}. \tag{2.25}$$

With the components of the flux vector belonging to the different particle types and the components of the matrix are given as

$$M_{ij} = -\left(\frac{1}{\lambda_i} + \frac{1}{d_i}\right)\delta_{ij} + \frac{Z_{ji}^d}{d_j} + \frac{Z_{ji}}{\lambda_j}.$$

MCEq takes this idea and carries it through to the end, by fully solving the cascade equations numerically. The complexity in solving the equations mainly lie in the energy dependency of the Z moments and over all in the X dependency of d_i.
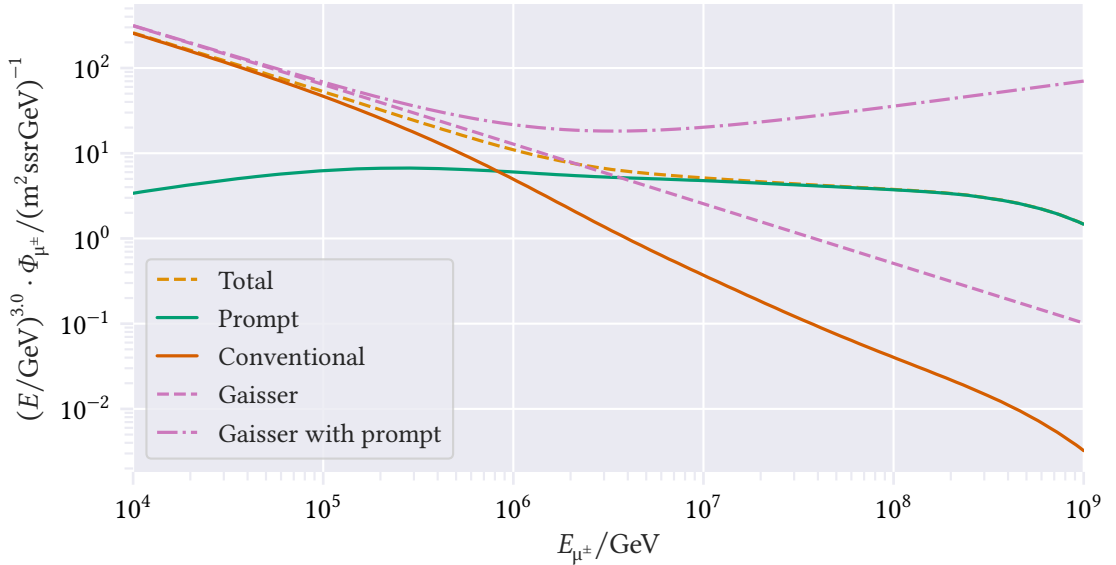
Figure 2.5: The energy dependency of the atmospheric muon flux at sea level, divided into the prompt and conventional component, as calculated with MCEq at $\theta = 0°$. Additionally, the flux parameterization by Gaisser from [GER16] is shown, which does not include prompt particles.

---

[13]This is why the sum over all hadrons independently is performed in Equation (2.22).

[14]The only difference to a EAS MC is, that here single hadron-interactions can be simulated, and there is no need to run a full coupled cascade.

The resulting spectra for muons from the cascade equations are shown in Figure 2.5, where the prompt and conventional and total spectra for muons are calculated with MCEq and results from the Z-moment method with values from [GER16] are shown. Reference [GER16] provides values for $H = \pi, K$ (conventional component), with the simple primary flux power law model eq. (2.1) with $\mathscr{A}_{\pi\mu} = 8.24 \times 10^{-6}$, $\mathscr{B}_{\pi\mu} = 1.11$ and $\mathscr{A}_{K\mu} = 4.45 \times 10^{-7} = \mathscr{B}_{K\mu}$. The reference also provides a parameterization for the prompt component by summing up all contributions from the different hadron of the prompt component into a component only consisting of the low energy contribution eq. (2.20), with $\mathscr{A}_{\text{prompt}\mu} \approx 10^{-3} \cdot \mathscr{A}_{\pi\mu}$, but $\mathscr{A}_{\text{prompt}\mu} = 10^{-4} \cdot \mathscr{A}_{\pi\mu}$ is used in Figure 2.5, which also overestimates the contribution. To gain good agreement with MCEq, the high energy contribution of charmed mesons starting at 10 PeV must be taken into account to describe the prompt spectrum. The crossover point for the prompt and conventional contribution is right below 1 PeV at a zenith value of $\theta = 0$.

The crossover point approximately rises with $f(\theta, h) \approx 1/\cos\theta^*$ with higher zenith angles. This is due to the zenith dependency of the conventional component, which is shown at 10 PeV in Figure 2.6. The precise results from MCEq are shown there, but additionally the approximate $1/\cos\theta$ and $1/\cos\theta^*$ behaviours from the Z-moment method are shown. Taking θ^* at $h = 50$ km they approximate the zenith distribution of the conventional flux well. The dip in both components towards 90° comes from additional energy losses of muons to the atmosphere. The slant depth at the horizon rises to approximately 400 000 kg/m², which is approximately 40 times its vertical value. The prompt component only shows slight variation in zenith, which is due to the charmed mesons coming to the end of their low energy limit at 10 PeV.
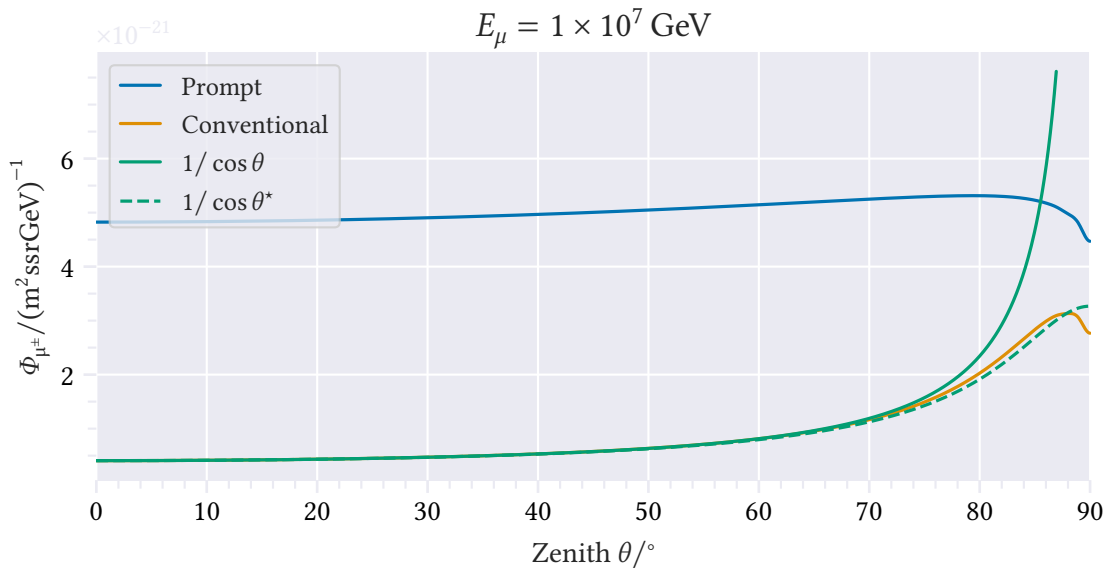
Figure 2.6: The zenith dependency of the atmospheric muon flux, divided into the prompt and conventional component component. The muon energy of 1×10^7 GeV is chosen, since it is right above the crossover energy for the prompt and conventional flux. The orange and blue lines show the MCEq-prediction. The green lines show two versions of the theoretical conventional prediction by Reference [GER16]. The solid version shows the original $1/\cos\theta$ dependency, while the dashed version shows a modified version where θ is replaced by $\theta^\star$ at 50 km.

3 The Prompt Muon Flux in Air Shower Simulations

Monte Carlo (MC) air shower simulation software, such as CORSIKA7, propagates particles through Earth's atmosphere by simulating interactions and particle decays. Although the MC program simulates every single particle in the shower, it is usually not necessary to save every single step of the simulation. The output of air shower simulation software is thus usually a list of particles and their corresponding attributes (energy, momentum, production height, etc.) only inside a defined plane (the observation level) or volume, as well as the properties of the primary particle which produced the air shower. This reduced set of information is usually sufficient to simulate the response of a detector. However, to differentiate the prompt component of an air shower, the production history of the observed particles must be known.

At this point it is important to mention that the definition of a prompt particle in astroparticle physics is somewhat different to other fields of physics. In high energy collider physics for example, a prompt particle is defined as a particle, which is produced directly in the proton-proton interaction and does not come from the decay of another particle [LHCb22]. In nuclear physics a "prompt neutron" refers to a neutron directly released by nuclear fission [US 93].

In astroparticle physics the term "prompt" refers to the lifetime of a decaying particle. As explored in Section 2.4, the following definition for the prompt and conventional part of the muon flux is used:

> The *conventional* part of the muon flux consists of all the muons originating from $\pi^{\pm}$, $K^{\pm}$, K_{L}^{0}, and K_{S}^{0} decays. All other muons are considered to be part of the *prompt* flux.

The pions and kaons are the mesons with the longest lifetime and they are the most common hadronic particles in an extensive air shower (EAS). Section 3.2.2 discusses other possible definitions of prompt muons. The nomenclature is a bit overloaded, but consistent nonetheless: The flux has a prompt part, and also individual muons in this flux are called prompt, although they are indistinguishable from conventional ones on a particle-to-particle basis. Sometimes, also the short-lived parent particles are called prompt.

"Prompt" in air showers refers to the *last* parent particle of the muon and not to the whole decay chain, like in collider physics. Thus, to split the flux into the prompt and conventional part with MC air shower simulations, the type of the parent particle for each observation level muon must be known. If this information is available, a label "prompt" or "not-prompt" to each observation level particle based on their parent particle can be assigned; this is referred to as *prompt tagging*.

This chapter describes how prompt tagging is implemented with CORSIKA7 output and shows that, to the knowledge of the author, for the first time consistent results with MCEq predictions for the prompt and conventional flux of muons have been produced. Previous work already used a similar tagging to estimate the contribution from the prompt component, but made no comparisons to MCEq or other theoretical fluxes [Meß22].

For tagging the prompt component, the extended history (EHISTORY) compilation option of CORSIKA7 is needed, which is described in detail in section 3.1. Along with this thesis the open-source python-package PANAMA [Nes23] was developed to facilitate the usage of CORSIKA7 and its EHISTORY option. The features include

- Correct parsing of the EHISTORY output

- Automatically running CORSIKA7 on multiple cores

- Weighting of CORSIKA7 output

- numpy- and pandas-friendly implementations of multiple state-of-the-art primary flux models

- Reading CORSIKA7 output files ("DAT" files) to pandas dataframes, using pycorsikaio [Lin23]

- Exporting DAT files to HDF5 files

The correct compatibility with EHISTORY has been implemented in the IceCube software IceTray as well [IC23b], to enable prompt tagging with IceCube MC data.

3.1 The Extended History Option of CORSIKA7

The default particle output format of CORSIKA7 is described in its userguide [KH93, p. 127]. It contains information about the whole CORSIKA7 run, for example the run number, and a block of data for each event. An event refers to one air-shower produced by a single primary particle. The event block also contains information about the run, for example the used version of CORSIKA. On the event level it stores the direction, type, energy and momentum of the primary particle for each event and a list with information about all the observation level particles. This list contains the particle ID (pid), the hadron generation counter (HGC), the number of the observation level (if multiple observation levels are defined), the momentum vector and the position/time since first interaction for each particle, that reached the observation level. With the EHISTORY compilation option of CORSIKA, this list of particles can be extended by two ancestors for muons and neutrinos [HE13]. The ancestors are marked with a negative pid encoding and the level of ancestors depends on the ordering in the file: Parent, Grandparent, Particle[1]. In theory the implementation of tagging prompt particles is straightforward: parsing the pid of the parent and assigning the prompt tag if the parent is neither a pion nor a kaon.

---

[1]CORSIKAs userguide calls them "mother" and "grandmother" particles.

However, the saved parent particles in CORSIKA are not guaranteed to be the direct parent particles, rather they are *some* ancestors. This does not diminish the prospect of tagging prompt particles with CORSIKA7, since there is a way to check how far apart the particles are in the decay chain: the HGC. The HGC is a number CORSIKA tracks for every particle. It is generally increased by one for every hadronic interaction and decay. There are multiple and important exceptions to this rule which have to be checked. The HGC

1. is not increased for short-lived resonances [HE13, p. 8]. As an artifact of this behavior, sometimes the counter is also not increased for some regular hadron decays. It is observed, for example, that in some cases, the HGC for the process $K^{*0} \rightarrow \mu^{\pm}$ is not increased, although the K^{*0} cannot directly decay into a muon and is far too short-lived, to interact with the atmosphere. A possible explanation of this is that CORSIKA7 passes the resonant particle to appropriate decay-routine (which may belong to a foreign hadron interaction model). The decay routine may then also generate the decays of the resulting child-mesons, since a K^{*0} (almost) always has a two-body decay into $K^{\pm}\pi^{\mp}$ anyways [PDG22].

2. is increased by 30 for a charmed decay, which is of special interest for the prompt component. Note that the documentation of EHISTORY says that it is increased by 31, not 30 [HE13, p. 7]. This seems to be either false or it has been changed in some update and is not addressed in the documentation. For CORSIKA version 7.7420 and onward, 30 is the correct value.

3. is increased by 51 for pion decay.

4. saturates at 99.

The HGC of the parent particle as well as the observation level particle is saved and thus their difference can be calculated. With this difference it can be asserted whether the given parent particle is really the parent, or rather, if there are still some intermediate decays. This begs the question: When does CORSIKA7 decide what parent particles to skip and what parent particles to write to output. The documentation does not give a definitive answer to that, but provides some examples [HE13, pp. 8, 9]. From the examples it appears that CORSIKA7 saves the "interesting" and rare decays, and only skips pions or kaons. With these assumptions, agreement with MCEq in the conventional and prompt muon flux is achieved (see section 3.2).

In summary: To tag a muon as prompt or conventional, the pid of the parent particle and the difference in the HGC must be known . Then:

1. If the difference is 0 or 1 and the parent is able to decay into the child[2], the parent pid is correct.

2. Else, if the difference is 30 and the parent particle is a charmed particle, the parent pid is correct.

3. Else, if the difference is 31 and the parent particle is a pion, the pid is correct.

---

[2]To respect the special case of non increasing generation counters from the previous listing.

4. Else the correct pid of the parent is unknown, but it's either a pion or a kaon and thus not prompt.

The prompt tag is assignable to the particle with this procedure. It is shown in the next section that the resulting spectra agree with MCEq predictions.

Nevertheless some inconsistencies with the HGC in produced CORSIKA7 output are observed. These include:

- Sometimes the difference in the HGC is negative (0.59 % of muons).

- Sometimes the difference in the HGC of a charmed parent is 29, although it should be at least 30 for a charm decay (0.74 % of muons).

- Sometimes a muon's parent particle is a muon (1.81 % of muons) [3].

These cases happen rarely enough to have no big influence on the overall flux, but indicate the need for careful cross-checks to verify that the tagging procedure is actually working — see section 3.2. The given percentages in parenthesis are calculated from the whole MC calculation described in the next chapter. An energy dependent version of these numbers are shown in appendix B.2.

With a modern and customizable EAS simulation, the tagging could be implemented with greater control over the details and without inconsistencies directly into the air shower simulation by adding a module to the software. Currently, no such finalized MC software exists, but CORSIKA8 is under active development [RU19]. An initial beta release is planned later in 2023 [HR23]. CORSIKA8 is a complete re-implementation of CORSIKA7 in the modern C++17 standard and aims at providing greatly increased usability, modularity, maintainability and customizability compared to its FORTRAN77 predecessor [Eng+19]. One of its explicit goals is to increase the capability of investigating a particle's history [RUP21; Rei23]. The eventual release of CORSIKA8 will with no doubt be an important milestone for the cosmic ray community and enable a whole range of interesting possibilities — for the time being, utilizing CORSIKA7's EHISTORY is the only option.

3.2 Prompt and Conventional Muon Spectra from a full Monte Carlo Simulation

To verify that the prompt tagging procedure is working as expected, a tagged and weighted MC sample is compared to the lepton fluxes produced by MCEq. MCEq uses the same hadronic event generators as CORSIKA7 internally to produce a tabulated version of the matrix M from the matrix-form of the cascade equations eq. (2.25) [Fed+15][4]. The method of numerically solving the cascade equations is a completely different methodology as running a whole MC simulation, which should be considered in evaluating the comparisons between MC and MCEq.

---

[3]This may come from multiple-scattering or pair-production, but makes no physical sense as a decay.

[4]MCEq further divides M into a decay part D and interaction part C.

The differences between obtaining flux predictions from MCEq and a full MC EAS simulation is summarized here. MCEq uses the pre-calculated matrix $\boldsymbol{M}$ (see eq. (2.25)), which tabulates the particle yield of decays and interactions at discrete energy values, to solve the cascade equations with the initial condition provided by a chosen primary flux model. The result directly provides the lepton fluxes at different energies, but contains no information about shower-to-shower differences, since there is no stochastic method involved and the same MCEq settings result in the same solution. CORSIKA7, on the other hand employs MC methods and samples particles from a given primary flux model and simulates all particle interactions and decays in the atmosphere stochasticly until some defined energy cutoff is reached. To generate physical fluxes from MC simulations, the simulation must be performed repeatedly, such that the statistics are high enough to be able to bin the resulting observation level particles in the energy space. Each particle is binned with a certain weight w, which contains the information about the frequency of the primary particle, which initiated the air shower.

The flux, from which the primary particle's energy is sampled, is not a physical one, but rather some arbitrary power law

$$\Phi_s(E) = \frac{1}{N} \cdot E^{-\gamma_s}. \tag{3.1}$$

Usually, $\gamma_s = 1$ or $\gamma_s = 2$ is chosen, depending on how much statistics in the high energy region are needed, where smaller spectral indices γ_s favor higher energy. If the sampled energy region is $E_p \in [E_{\min}, E_{\max}]$, then N in eq. (3.1) is chosen such that Φ_s is normalized. The weight w for an event with primary energy E_p is

$$w = \frac{\Phi_p(E_p)}{n\Phi_s(E_p)} = \Phi_p(E_p) \cdot \frac{N}{nE^{-\gamma_s}}, \tag{3.2}$$

where n is the total number of events generated in the energy region. The normalization factor is given by

$$N = \begin{cases} \ln\left(\frac{E_{\max}}{E_{\min}}\right) & \text{if } \gamma_s = 1 \\ -(\gamma_s - 1)^{-1}\left(E_{\max}^{-(\gamma_s-1)} - E_{\min}^{-(\gamma_s-1)}\right) & \text{else} \end{cases}.$$

Cosmic Rays (CRs) vary in energy more than 10 orders of magnitude. Due to the power law nature of their spectrum, their flux spans an even wider range across these energies. To investigate high energy CR phenomena, like prompt muons, high statistics in the very high energy region are needed. The MC runtime for a single air shower (event) is approximately equal to the number of particles in the air shower. Based on the Heitler-Matthews model explained in Section 2.2, the number of particles is approximately proportional to the primary's energy[5]. Simulating a 1 PeV air shower thus takes approximately 1000 times longer than a 1 TeV shower. Because even with unphysical sampling spectra of $\gamma_s = 1$, the number of simulations required to gain enough statistics in the high energy region above e.g. 1 EeV is unfeasible, another trick

---

[5]Because a shower from a nucleus with mass-number A behaves very approximately as A independent nucleons, the runtime also is proportional to A.

is applied for simulations across many orders of magnitude in energy: The whole energy region is split up into different sub-regions, which all contain a given number of events. If the energy intervals are disjoint, which is usually chosen to be the case, the weighting from eq. (3.2) can be performed straightforward separately on all sub-sets. If the energy intervals are not disjoint, the weighting has to be performed separately in every region of overlap, which makes the procedure more complicated. The weighting used in this section is implemented in PANAMA [Nes23], IceCube's weighting is implemented in the `SimWeights` python package [IC23c].

With energy bin edges $E_0, E_1, \ldots, E_m$ the muon flux differential in energy in the ith energy bin ($E \in \left(E_i, E_{i+1}\right]$) can be calculated with

$$\Phi_i = \frac{1}{E_{i+1} - E_i} \sum_{\substack{j \\ E_\mu^j \in \left(E_i, E_{i+1}\right]}} w_j$$

where j enumerates all observation level muons, w_j their weights according to eq. (3.2) and the sum is performed over all muons, with energy in the energy bin. As with all weighted histograms, the error on the bin entry is given by[6]

$$\Delta\Phi_i = \frac{1}{E_{i+1} - E_i} \sqrt{\sum_{\substack{j \\ E_\mu^j \in \left(E_i, E_{i+1}\right]}} w_j^2}.$$

The primary CR spectrum consists of many nuclei, ranging from hydrogen to iron and beyond [GER16]. In simulation, usually not all nuclei are injected with a composition which is physical. Instead, the different primaries are divided into a number of groups and for each group the dominant nucleus is chosen to represent all showers in that group. Normally, groups are chosen to be roughly of constant length in $\log(A)$, since $X_{\max}$ varies in $\log(A)$ [KU12], which can be understood with the Heitler-Matthews model (section 2.2[7]). This chapter uses the same five components as the standard IceCube software: hydrogen, helium, carbon, silicon and iron.

The properties of the used CORSIKA7 dataset in this chapter are listed in Table 3.1 and the full steering card can be found in Listing 1 in Appendix B.1. CORSIKA7 version 7.7420 is used and compiled with the CHARM, CURVED, DYNSTACK and EHISTORY options. The configured high energy hadron model is SIBYLL2.3d and the low energy one is URQMD. The prompt component of the muon flux, becomes dominant at around 1 PeV, hence the settings are chosen, such that all the muons above 1×10^5 GeV are generated. The primary energy range starts at 1×10^5 GeV, and the hadron and muon cutoff is set to 1×10^5 GeV as well. This allows for the large statistics of more than 30 million showers (see table 3.1), since the many low energy muons and hadrons must not be computed. The electromagentic (EM) components (electrons

---

[6]This can be derived with the multiplicative and additive properties of the variance, see e.g. `www.boost.org/doc/libs/1_82_0/libs/histogram/doc/html/histogram/rationale.html`.

[7]If the primary composition is measured using the number of muons, it varies with $A^{1-\beta}$, roughly with $\beta \in (0.88, 0.92)$

and photons) are completely cut away, so that only the hadronic part of the shower is simulated. This has little effect on the generated muons, since EM-processes which produce hadrons or muons are heavily supressed[8]. With these settings the runtime on 40 cores was approximately 5 days.

Table 3.1: The Monte Carlo dataset used for the figures in this section is listed. `CORSIKA7` used the `SIBYLL2.3d` hadronic interaction model and a curved atmosphere. Each primary was simulated with a spectral index of $\gamma_S = 1$ once for a zenith angle of $0°$ and once for $60°$. The electromagnetic component was not simulated and the hadronic and muonic cut below which simulation is stopped was set to 1×10^5 GeV.

E_{min}/ GeV	E_{max}/GeV	Primary	Number	Spectral Index	Zenith
		H1	10×10^6		
		He4	10×10^6		
1×10^5	1×10^9	C12	10×10^6	1	$0°, 60°$
		Si28	1×10^6		
		Fe54	1×10^6		
		H1	100×10^3		
		He4	100×10^3		
1×10^9	5×10^{10}	C12	100×10^3	1	$0°, 60°$
		Si28	10×10^3		
		Fe54	10×10^3		

Utilizing the `EHISTORY` option for prompt tagging without accounting for the HGC, the results are not consistent with expectations, as can be seen in Figure 3.1. This is expected and shows that the correction of the HGC described in this thesis is needed. Figure 3.1 compares the uncorrected readout to MCEq, but the fluxes are also not consistentt: the flux is weighted with $E^{-3.7}$, so an approximately flat spectrum for the conventional component is expected, with the prompt component rising. The flattening of the "prompt"-labeled component below the crossover region of about 1 PeV indicates substantial contamination from the conventional component. While the region beyond $10^{6.5}$ GeV behaves more correctly, the deviations in the lower energies make an uncorrected `EHISTORY` readout unusable for analysis of the prompt component.

When accounting for the HGC as described earlier, the resulting spectra agree with MCEq predictions, which can be seen in Figure 3.2. This indicates that the tagging procedure is working correctly and can be used to identify prompt muons in the MC simulation.

---

[8]Consider for example muon-pair-production, which is suppressed by a factor of $m_e^2/m_\mu^2 \approx 2 \times 10^{-5}$ compared to electron-pair-production
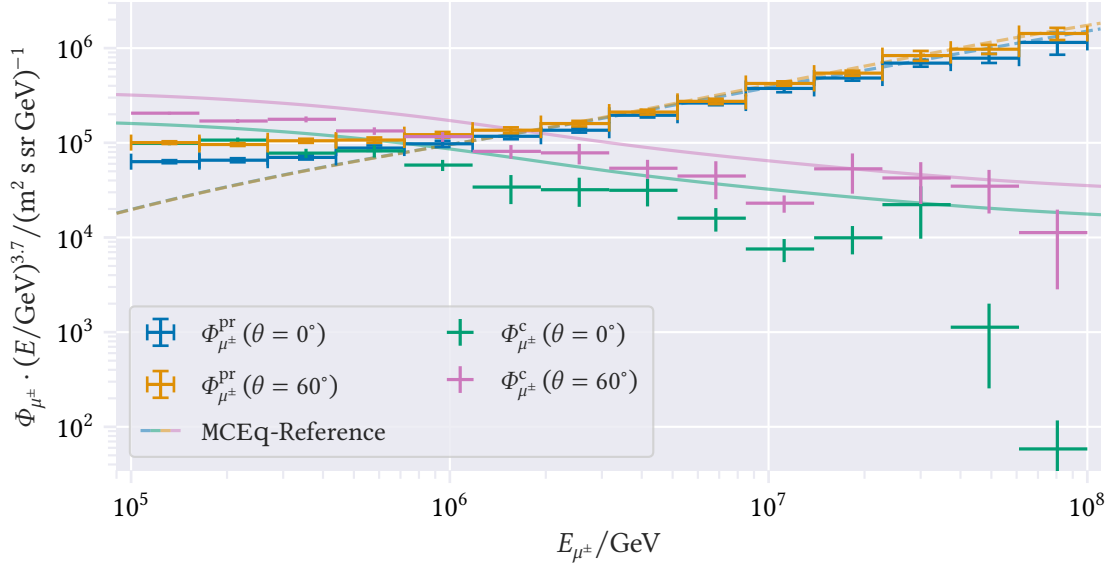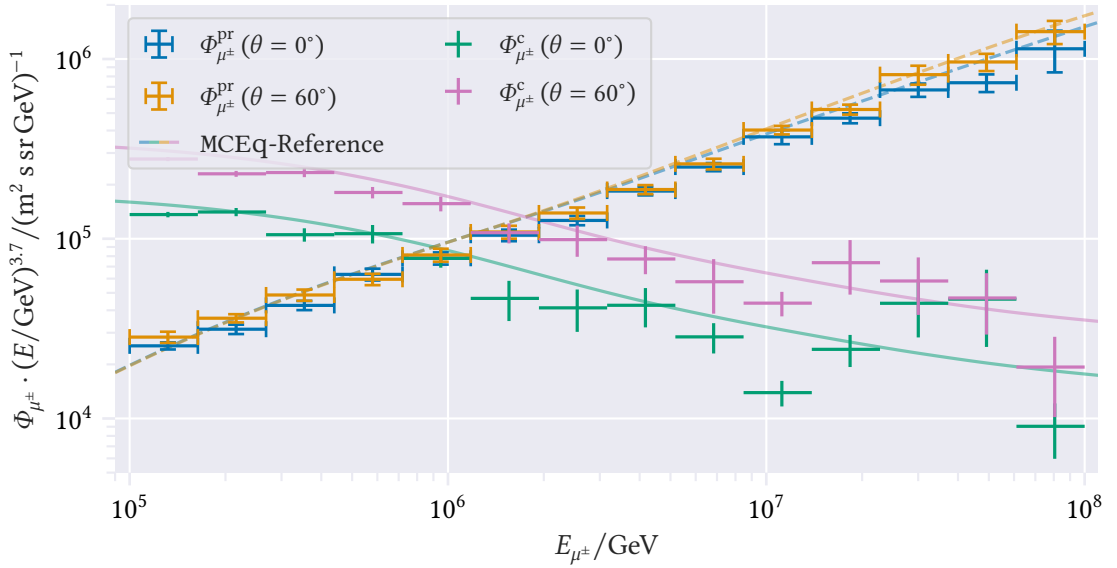
Figure 3.1: The high energy muon spectrum produced by CORSIKA7 (crosses) devided into the prompt (orange and blue) and conventional (green and pink) component is shown at two different zenith angles $\theta = 0°$ and $\theta = 60°$. Here, the readout with the EHISTORY option is *not* corrected as described in this section. Especially right below the cross-over region the spectrum does not match the MCEq-prediction shown in solid lines. Global Spline Fit (GSF) is the primary model in both cases.

Figure 3.2: The high energy muon spectrum produced by CORSIKA7 (crosses) devided into the prompt (orange and blue) and conventional (green and pink) component is shown at two different zenith angles $\theta = 0°$ and $\theta = 60°$. The MCEq-prediction shown in solid lines matches the weighted CORSIKA7 histograms. GSF is the primary model in both cases.

3.2.1 Muonic Origin

Most muons in EAS come from pion or kaon decay and are referred to as conventional, as already established. The other muons, the prompt ones, come from heavier meson decays. For a long time, it was believed that most of the prompt atmospheric muon flux originates from charm hadron decays (mainly $D^\pm$, D^0, $\overline{D}^0$ and Λ_c) [Bug+89; TIG96; Bug+98]. Only in the last decade it was realized that unflavored meson decays (mainly $\eta, \eta', \rho^0, \omega$ and ϕ) probably contribute to the flux on the same level as charm decays [Ill+11; GER16]. Charmed and conventional decays produce a neutrino as well, as seen in its tree-level Feynman-Diagram fig. 3.3a, while unflavored decays do not produce neutrinos, as seen in Figure 3.3b. Differentiating the origin of the muon at ground level is not possible with CR-observatories, since all muons leave the same tracks in a detector, no matter their origin. Probing muon production processes is only possible in collider experiments, like the ones at CERN's Large Hadron Collider (LHC). LHC can measure the decay rates of hadrons and they are subsequently used for example in MC event generators like SIBYLL. With EAS simulation software, the origin of muons in EAS can be studied, as they in turn use the event generators, which are tuned using collider data.

(a) $\pi^-/K^-/D^- \to \mu^- \bar{\nu}_\mu$ **(b)** $q\bar{q} \to \mu^- \mu^+$
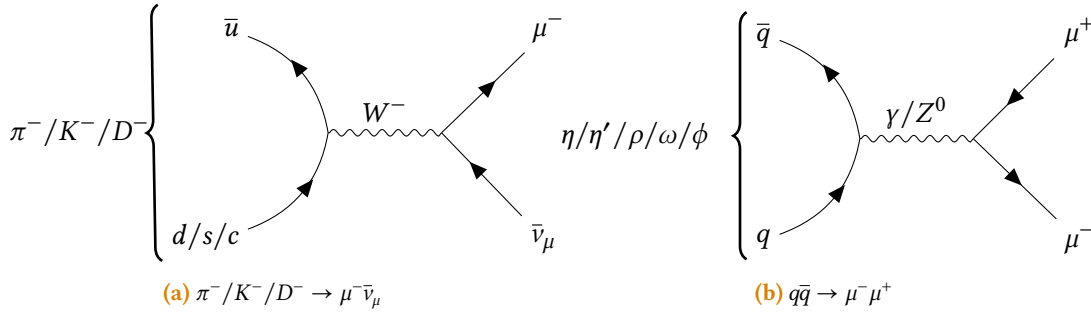
Figure 3.3: Leading order Feynman diagrams for the $\pi^- \to \mu^- \bar{\nu}_\mu$ decay (fig. 3.3a) and unflavored decays of the type $q\bar{q} \to \mu^- \mu^+$ (fig. 3.3b) are displayed. The K^- (D^-) decay has the same leading order diagram as in Figure 3.3a, but the down (up) quark is swapped with a strange (charm) quark.

The previous Section 3.2 showed that reconstructing the muon origin with CORSIKA7 agrees with MCEq predictions on the level of differentiating between the prompt and the conventional component. Splitting up the conventional component of the muon flux into muons originating from $\pi^\pm$ or $K^\pm$ decay with CORSIKA7 is not possible: EHISTORY only provides enough information to say that a parent particle is conventional, some of them are undetermined to be either a pion or a kaon. But further dividing the prompt component of the flux into origins from multiple other particles is possible, and this can also be compared to MCEq results. This is done in Figure 3.4. The solid lines there show the MCEq solutions from [Fed+19]. It is noticeable that the two methods don't agree with each other for every particle, although they do if summed up, as shown in Figure 3.2. The two particle types with the most contradicting results are D_s and D^0. The differences probably can't be explained with the hadronic models, since both in the CORSIKA7 simulation and in MCEq the same one, namely SIBYLL2.3, is used. The only difference is the concrete version, as for MCEq SIBYLL2.3c is used and for CORSIKA7
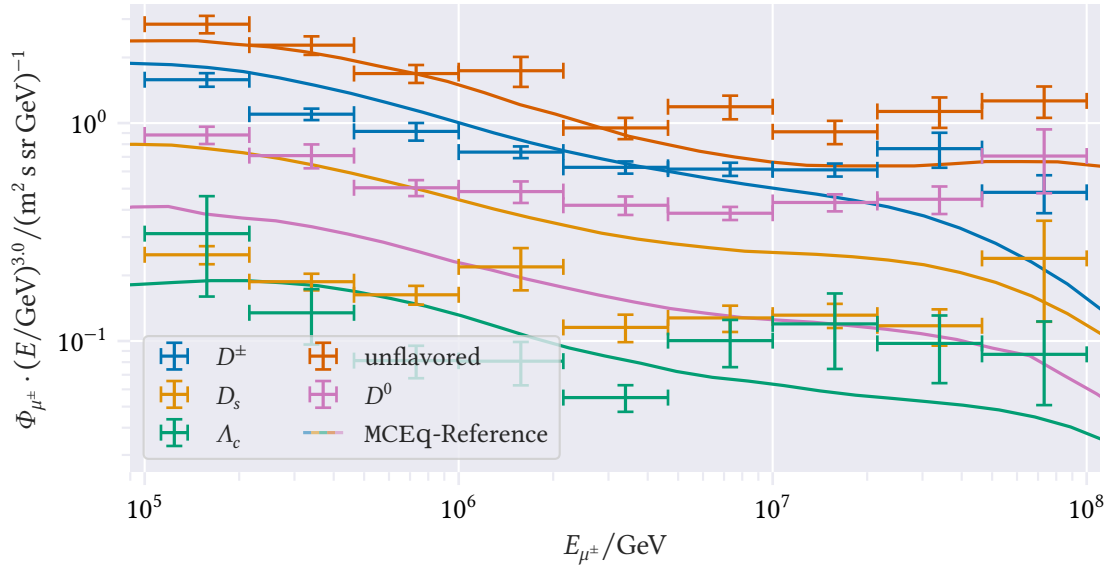
Figure 3.4: The prompt component of the high-energy muon flux divided into different parent-particles is shown. The crosses come from the described CORSIKA7 EHISTORY readout, while the solid lines come from numerical solutions to the cascade equations from MCEq. The MCEq data are taken from [Fed+19].

SIBYLL2.3d is used. According to correspondence with the developers of the model and the corresponding papers [Fed+19; Rie+20], the differences between the c and d version of the software are minimal and probably can't explain a difference to this degree. Efforts have been made to reproduce the fluxes from fig. 5 of [Fed+19], but the current version of MCEq does not support SIBYLL2.3d and also does not provide the feature to differentiate all particles, only some of them (like the D_s).

While the differences in the per-particle readout are unsatisfactory, they do not play a role in the tagging procedure. The discrepancies will probably only be solved with the new version CORSIKA8, which provides a much finer grained control over the history of particles. Possible reasons for the discrepancies are

- Different hadronic interaction models (SIBYLL2.3c/SIBYLL2.3d) → unlikely, as they only differ slightly.

- Different methods (Cascade equations/MC) → Different methods should agree.

- An implementation error in the code of the EHISTORY readout.

- An implementation error in EHISTORY.

- An implementation error in MCEq.

- Labeling errors in fig. 5 of [Fed+19].

A third method for comparison could give some insight into where exactly the problem lies. CORSIKA8 is under early development and working with the unstable CORSIKA8 exceeds the scope of this thesis. Another option is to compare to the production cross section measured by collider experiments, although direct comparison must be performed with great care, since the results from air shower simulation are a convoluted version of the production cross section (through the cascade equations). Focusing on the difference in the D_s and D^0 production, since it is the most significant. The LHCb collaboration reports that the production cross section for D^0 is $(2072 \pm 2 \pm 124)\,\mu b$ in pp collisions at a center of mass (COM) energy of $\sqrt{s} = 13\,\text{TeV}$, which corresponds to a fixed target energy of $E_{FT} \approx 90\,\text{PeV}$ [LHCb16]. While the production cross section for D_s^+ is $(353 \pm 9 \pm 76)\,\mu b$. The data is given in a pseudo rapidity range of $2 < y < 4.5$, so as always in CR physics, it's hard to compare to the extreme forward boosted region of EAS, although the fixed target energy is in the relevant region for prompt muons. The D^0 decays into muons $(6.8 \pm 0.6)\,\%$ of the time and the $D_s^\pm$ decays into muons $(6.33 \pm 0.15)\,\%$ (assuming lepton flavor universality) of the time [PDG22]. This provides a hint into the direction, that there indeed should be more muon production from D^0 than from D_s.

3.2.2 Definitions of Prompt

The prompt component of EAS can be defined in different ways. This chapter compares different possible definitions and their influence on the obtained muon fluxes. From the particle theorist point of view, each type of meson in an air shower behaves differently. They can for example calculate the spectrum weighted Z-moments for pion, for multiple charmed mesons with a variety of different Quantum Chromo Dynamics (QCD)-meson models, increasing in precision and detail over time and for a variety of different primary flux models. From these Z-moments, a theoretical prediction of the muon flux is obtained, for different models of mesons and different primary flux models.

From the experimentalist's point of view, the interesting thing is the different behavior of the prompt component in variables, which can actually be measured, since decays inside the EAS can be probed only indirectly. The three measurable differences of the prompt component are the different spectral index, the flatness in zenith and the non-existence of seasonal variations.

These differences can be explained phenomenologically, without the need for full QCD calculations. The different spectral index arises from the fact that the mesons with the short lifetime most likely decay before they interact with the atmosphere and thus do not lose energy to the atmosphere, which makes their spectrum flatter. This effect depends on the energy region, since the decay length is Lorentz-boosted, and thus for higher energies, interaction with the atmosphere starts to dominate again. The non-existing zenith dependence can be explained by the fact that the short-lived mesons decay before they travel any significant amount through the atmosphere and thus there is no competition between interaction and decay, which is the reason why the $1/\cos\theta^*$ dependency of conventional muons arises. The non-seasonality of the muon flux arises for the same reason: prompt mesons almost always decay before they interact with the atmosphere, so it does not matter how dense the atmosphere is due to temperature variations in the seasons.

Based on these different perspectives on the prompt flux, multiple ideas on how to identify the prompt flux in a MC simulation may be proposed. As already established in the last section, to arrive at consistent results with theorist's predictions and therefore MCEq, the tag of the prompt component must be based on the last decay in the decay chain, as can be seen in Figure 3.2. In this section four slightly different definitions of "prompt" are investigated. The figures in this chapter show the MCEq predictions as a baseline to provide a reference for the deviation of the suggested definition shown in Figure 3.2, which is consistent with MCEq. This means, that for most figures in this chapter consistency with MCEq is not expected.

The first definition, here called the "energy" definition, separates the two components based on theoretical considerations on the crossover energy between the interaction dominated and the decay dominated part of the spectrum. As explained in section 2.4, below the parent-particle type H specific critical energy ϵ_H, the decay dominates over interaction. This is labeled as prompt by the energy definition, while parent particles with energy above ϵ_H are labeled as conventional. By this definition, any particle with enough energy (more than the critical energy) becomes conventional at some point. Just that the critical energy is different for different particles. This is also true the other way around: every particle can be prompt, if the energy is small enough (below the critical energy). The critical energies for some particles are listed in Table 2.1. Under the assumption that the interaction length in air is approximately the same for any meson,[9] the critical energy can be calculated for any meson with the formula

$$\epsilon_h = h_0 \frac{m_h c}{\tau_h} \approx \frac{m_h c^2}{\tau_h} \cdot 21\,348.10 \text{ ns}.$$

Here a typical scaling height of $h_0 = 6.4$ km (like in [GER16, p. 122]) is used. This critical energy is used for the prompt definition seen in Figure 3.5. It shows that this definition produces agreeing results with MCEq until roughly the crossover point at 1 PeV. Above 1 PeV, the conventional labeled particles start having a similar spectral index to the prompt component. This is because a lot of D-mesons which decay right above the critical energy somewhere above 10 PeV start contributing to the conventional component. Once the crossover region is in energies is passed by a few orders of magnitudes, the conventional component is expected to start having the spectral index from other definitions again.

This definition can be improved: a zenith dependence in the critical energy can for example be introduced, to account for the varying slant depth with the zenith angle. More accurate interaction lengths for different mesons can also be used or the true slant depth at the meson's interaction height can be calculated. Since this definition is not used anywhere else, for demonstration purposes only this simple energy threshold is presented.

Prompt particles dominate at higher energies, since they do not lose as much energy in the atmosphere as conventional ones. Considering this, the idea to select all the particles in the MC simulation, which did not lose a significant amount of energy to the atmosphere seems

---

[9]This is not exact, but only a rough approximation. Since mesons mostly interact with the air nuclei via the strong force, the independence of the hadron type can be motivated by QCD's flavor-blindness. For a comparison of the interaction lengths of pions and kaons at different energies, see for example table 5.4 of Reference [GER16].
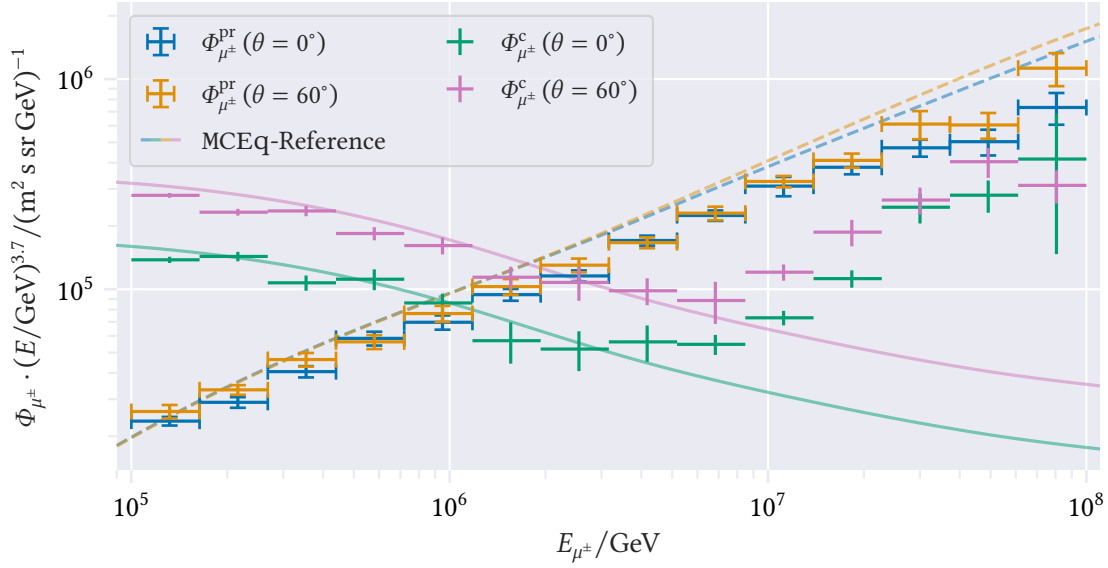
Figure 3.5: Shown here is the energy definition of prompt for the CORSIKA7 fluxes (crosses) described in the text. The MCEq prediction (lines) is shown as a reference, but is not expected to agree with this definition, since MCEq uses a different one. The energy definition separates the prompt and conventional flux with a particle-type dependent energy threshold for the parent particle. In the high-energy region the methods do not agree, because the energy-threshold for charmed mesons at about 3×10^7 GeV is reached. The GSF model is used for weighting.

reasonable. For example these may be the muons directly created in the first interaction, or these could be the muons created from only short-lived mesons in the whole decay chain, since these do not interact much with the atmosphere. This means that for example a decay chain of the type $p + \text{air} \rightarrow \pi + \text{air} \rightarrow D^+ \rightarrow \mu^+ \nu_\mu$ would not be counted as being prompt, because of the intermediate pion. With the standard definition of prompt, the muon would be a prompt one, since it comes from a D meson decay. Since the full decay chain is not available in CORSIKA7, this definition can't fully be implemented, but an approximation can be: the information about the grandparent particle to the observation level muon is available[10]. Thus, in the "grandmother" definition of prompt, additionally the particles are labeled as prompt, which have a pion or a kaon as a grandparent, even if their parent is prompt.

The resulting fluxes from the "grandmother" definition of prompt can be seen in Figure 3.6. While the lower energies look quite similar to for example Figure 3.2, in the higher energies the conventional component is overestimated, since more prompt particles are excluded from being prompt, but no additional ones are introduced.

The two definitions, which finally produce agreeing results with MCEq and therefore theory predictions, are called the "pion-kaon" definition and the "lifetime" definition. The "pion-kaon"

---

[10]CORSIKA7 calls this the "grandmother"
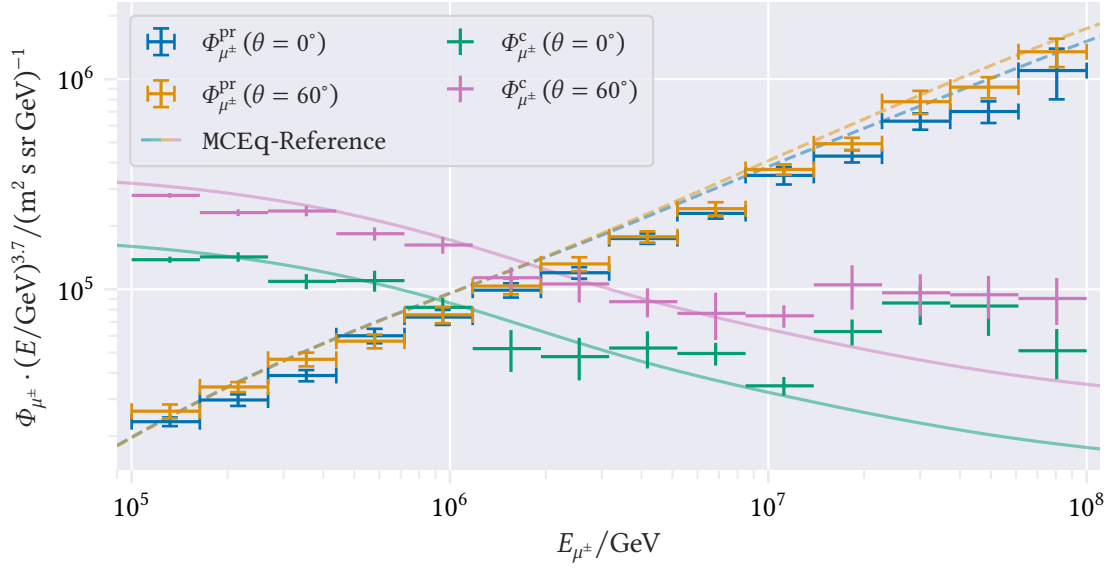
Figure 3.6: The grandmother definition of prompt is visualized. The MCEq predictions (lines) are shown as a baseline, but are not expected to agree with the CORSIKA7 fluxes (crosses). For the crosses, the type of the grandparent particle in addition to the parent particle is considered to tag the prompt component in the CORSIKA7 simulation. The methods are deviating somewhat in the high energy region. A good agreement is not expected, as MCEq does not consider the whole decay chain of a muon, only the last step, to differentiate prompt and conventional. The tag used here considers the last two steps of the decay chain. The used primary parametrization is MCEq.

definition is explained in more detail in the last chapter and can be seen in Figure 3.2. It includes every muon with a parent particle of $\pi^{\pm}, K^{\pm}, K_{\mathrm{L}}, K_{\mathrm{S}}$ or of unknown particle type as conventional, while the rest is prompt. The "lifetime" definition is similar, as it includes every particle with a lifetime which is greater than ten times the lifetime of the D^0 as conventional and the rest as prompt. This is the definition of prompt used inside MCEq, and the lifetime limit corresponds to a decay length of approximately 1.2 cm. Considering all particles in CORSIKA7[11], these are the $\gamma, e^{\pm}, \mu^{\pm}, \nu$ from the fundamental particles. Of these none can decay into a muon, although, as already mentioned in the previous chapter, a muon can be listed as the parent of a muon. These would then be considered to belong to the conventional component. The hadrons below the lifetime limit are $\pi^{\pm}, K^{\pm}, K_{\mathrm{L}}, K_{\mathrm{S}}$, which are exactly the pion and kaons from the pion-kaon definition. The Baryons below the lifetime limit are $p, n, \Lambda, \Sigma^{\pm}, \Xi^0, \Xi^{\pm}$, of these only the proton and the neutron can not decay into a muon. These baryons and the muon is the only difference compared to the pion-kaon definition of prompt. These particles do not seem to contribute much to the flux, as both of the definitions produce nearly identical results, as shown in Figure 3.8. This lifetime definition has therefore also approximate agreement with MCEq, see Figure 3.7.

A comparison of the prompt fluxes for the four different definitions of prompt can be seen in

---

[11]Automated for example with the `particle` python package [RS]
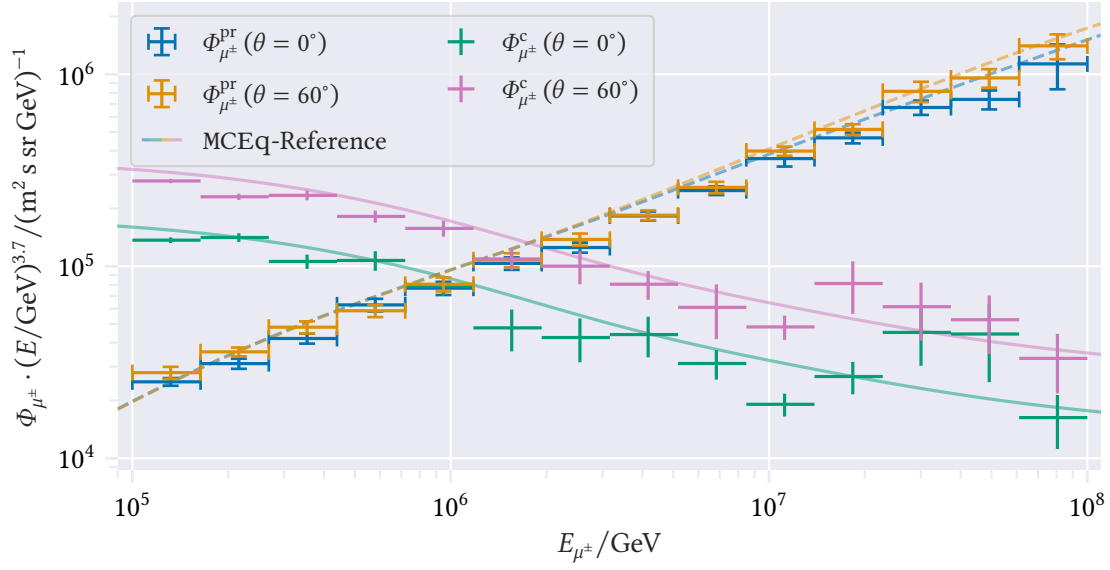
Figure 3.7: The lifetime definition of prompt is shown. A prompt definition based on a lifetime limit of the parent particle is considered in the CORSIKA7 simulation (crosses). The lifetime limit is chosen at 4.1×10^{-3} ns, which is 10 times the lifetime of the D^0 meson. The lines show the MCEq fluxes, which use the same definition for the prompt flux. The CORSIKA7 simulation is weighted with the GSF model.

Figure 3.8. The figure also shows that the different definitions do not vary largely, and that especially the pion-kaon definition and the lifetime definition are almost the same. All the definitions from this chapter can be generated with the `prompt` module of PANAMA [Nes23].
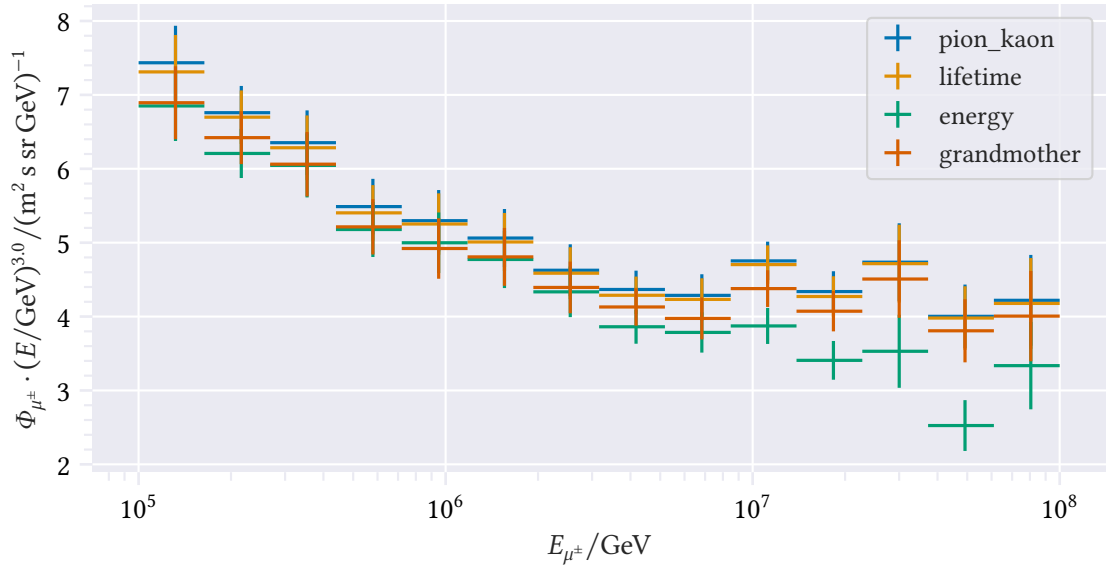
Figure 3.8: The prompt muon flux for four different possible definitions of the prompt component for tagging is shown. The simulation is weighted with the GSF. Here, a weighting with E^3 is chosen to keep the prompt component approximately flat.

3.2.3 Influence of the Primary Model

The used parametrization of the primary CR flux has a great influence especially on the prompt component. The reason behind this is, that the different primary models have the biggest differences in the high energy region. This is the least explored part of the CR flux, due to the fact that high energy CR events are very rare. The composition and flux of these are still subject to active research [Hil06]. Since the muon energy is a lower bound of the CR primary energy, the CR producing the prompt component in the region where the prompt component becomes dominant, are in the region of high uncertainty.

The results for the prompt flux from CORSIKA7 and MCEq for four different state-of-the-art primary models are displayed in Figure 3.9. The GSF and the Global Fit GST (GST) [Dem+17; GST13] models produce the highest prompt flux. The Gaisser H3a and H4a models [Gai12] produce lower prompt fluxes. In particular, the H3a model produces prompt fluxes which are up to a factor of 5 lower than for example in the GST model at high energies.
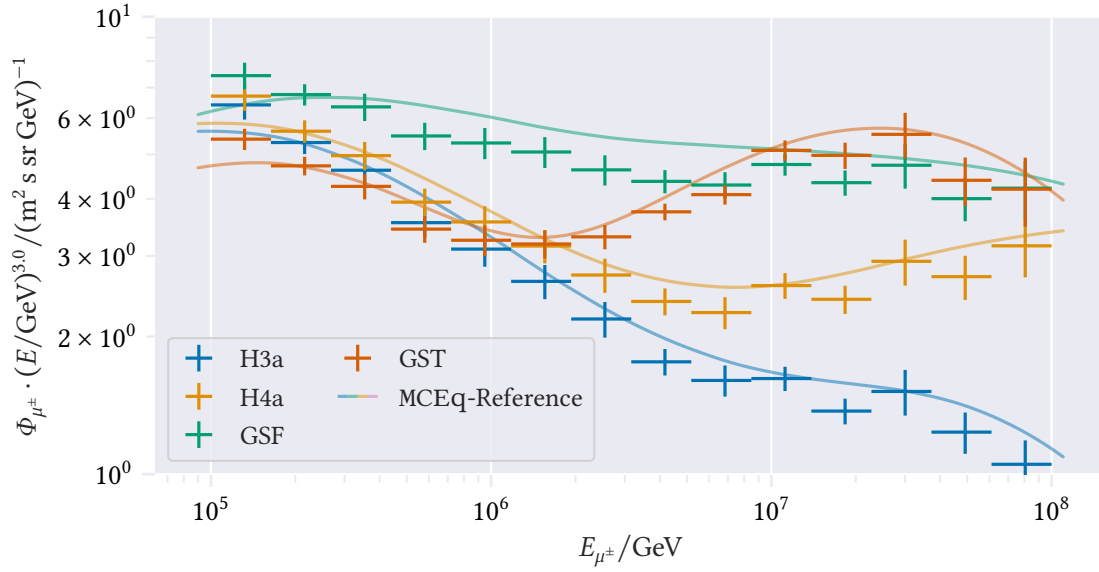
Figure 3.9: The prompt muon flux for different primary models, calculated with MCEq (crosses) and EHISTORY (lines) is compared.

3.3 Manipulating the Prompt Component

3.3.1 Scaling

As shown in the previous sections, the prompt component of the atmospheric muon flux can be identified reliably in CORSIKA7 simulations with the tagging developed in this thesis[12]. While this opens the door to investigate the properties of the prompt component of the muon flux in MC simulations[13], it can also be used as the basis of an analysis of the prompt component in data.

Another method to analyze the prompt component can be considered: In the first step a number of different MC sets with the same parameters is produced, which only differ by the strength of the prompt component in the MC simulation. The strength of the prompt component can be adapted by replacing a prompt particle, e.g. the D meson, with a certain probability p by an equivalent pion or kaon. Equivalency here means, that the particle needs to have the same charge and the momentum needs to be changed to conserve energy. Then datasets for different p can be produced, for example $p = 0, 0.5, 1, 1.5, 2$. Where $p > 1$ means that instead of a prompt particle being replaced by a conventional one with probability p, a conventional particle is replaced with probability $p - 1$ by a prompt one. Then an interpolation between the datasets can

---

[12]It has to be mentioned again, that previous work already did a lot of work to understand how to use the EHISTORY option to identify the prompt component, see [Meß22].

[13]This is done in the next section

be performed, to accurately describe the data. From the interpolation, the most likely strength of the prompt component could be estimated.
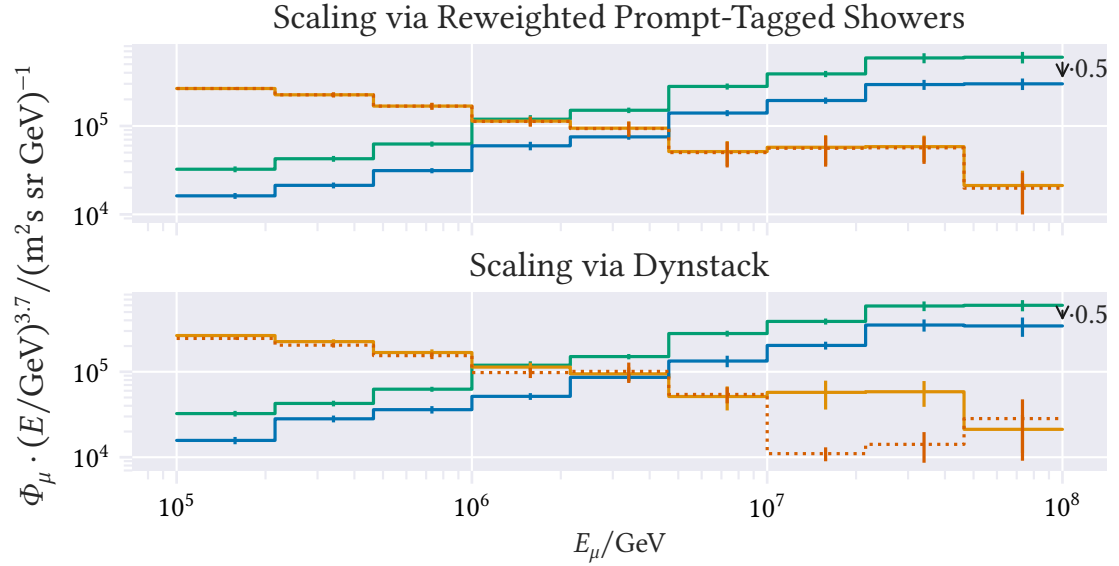
Figure 3.10: Two methods for scaling the prompt component of the muon flux at $\theta = 60°$ are compared. The green histogram shows the baseline prompt component, as standard CORSIKA7 simulations produces it, while the blue histogram shows a downscaled version of the prompt component by a factor of 0.5. The orange histogram shows the conventional component, while the orange dotted histogram shows how the scaling of the prompt component changes the conventional one. The upper panel shows scaling by applying an additional weight of 0.5 to the events (showers) which are tagged as prompt, and the lower panel shows the scaling method implemented via DYNSTACK, where a new simulation dataset is created where prompt particles are explicitly replaced by conventional ones in the simulation. The GSF model is applied for weighting.

For this analysis-idea, nicknamed the "DYNSTACK-method", the CORSIKA7 simulation needs to be modified, which is done most easily in a modern way, via CORSIKA7's DYNSTACK module [Baa16]. The results from down scaling the prompt component in CORSIKA7 by a factor of 0.5 can be seen on the bottom panel of Figure 3.10. It is observable, that when downscaling the prompt component, also the conventional component of the muon flux is reduced in the two energy bins above 10 PeV. This can be explained by the method of how the replacement in DYNSTACK works. Each time a prompt particle enters the stack, it is replaced by some probability, no matter where in the decay chain the particle exists. This means, also a conventional muon coming from a decay-chain of the form $D + air \rightarrow \pi^+ \rightarrow \mu^+$ is removed with the probability p. This effect should be notable in the energy region where the interaction of charmed mesons with the atmosphere becomes relevant, which is, according to table 2.1, somewhere above 10 PeV.

The downside of this method is the heavy computation costs: generally the EAS simulation is one of the most costly steps in the whole MC simulation chain of CR observatories. If this simulation

step has to be repeated multiple times for different strengths of the prompt component, some of which might turn out to be not relevant or realistic, a lot of computation power is wasted. Another problem with just changing out particles in the simulation is not breaking up the physics of the simulation. The ideal replacement is equal to changing the strength of the prompt component in the MC generators, that means for example changing the production cross section of charmed and unflavored particles. Just replacing particles needs to regard a lot of laws to be physically flawless: energy conservation, the energy-dependent pion/kaon ratio, momentum conservation, cross-section measurements from collider experiments and phase space distributions. For these reasons, the idea of applying a weight to the prompt component arose.

As explained in section 3.2, the generated MC events are weighted to the a primary model anyway, so after that another weight of n_{pr} can be applied to only the prompt events. With that the strength of the prompt component can be varied with nearly no computation cost, after the whole MC simulation has already been produced. This is the second method, referred to as the "reweighting-method".

What exactly classifies as an event here, can vary depending on the use case. For comparison to theoretical single-muon flux predictions from theorists, each muon in the simulation can be weighted differently. That means that in a single shower, each muon can have either a weight of w (see eq. (3.2)), or a weight of $w \cdot n_{conv}$. Another possibility is to apply a weight to the whole shower, so each muon in the shower has the same weight, as in usual MC weighting. Then the question arises, which muon in the shower decides if the whole shower gets a weight for prompt. It might appear superficial to force all muons in a shower to have the same weight, but regarding experimental data, for example IceCube measures one air shower at a time and generally can not resolve the different single muons in an EAS[14]. It seems natural that the decision if the whole shower is weighted as prompt or conventional is based on only the muons with the highest energies in an air shower. If the extreme is assumed and only the highest energy muon in the air shower (called "the leading muon") is considered in the decision if the whole shower receives a weight, how big is the error to the total flux? At least a small error is introduced: our goal is to scale down the strength of the prompt component, but as there are almost certainly also conventional muons in the shower. The conventional component is affected as well.

A physical argument hints at the case, that only a minor error to the total flux is introduced. Considering the energy distribution of the primary particles, which on average produced a muon of energy E_μ, some of its properties can be deduced[15]. The distribution is surely 0 below the muons energy, to conserve energy. It is expected to rise in some sense slowly directly above the muon energy, since it is unlikely that most of the primary energy is converted to the muons energy. It must have a maximum at some point, and fall of to 0 for primaries many orders of magnitude above the muon energy. This is due to the fact, that the muon number is expected to only rise sub-linearly with the primary energy, according to the Heitler-Matthews model

---

[14]As seen in the next chapter, a proxy-variables to get a grip on the single-muon spectrum can be generated.
[15]This is called the response function for a single muon energy in literature [GER16].

(see Equation (2.6)), but the occurrence of these showers are suppressed with the well-known power law of at least $E^{-2.6}$. In simpler words this means: a primary with the energy $E_p = 10^4 E_\mu$ might approximately produce 10^2 times more muons at the right energy, compared to a shower with $E_p = 10^2 E_\mu$, but it also happens $\left(10^2\right)^{2.6} \approx 10^5$ times more rarely. This means that most muons are expected to come from primaries with energies which are not too far above the muon's energy. MC simulations show that this is indeed only 0-2 orders of magnitude above the muons energy, this is later in Figure 3.12. If this is the case, then muons which do not carry a significant amount of the primary flux, do not contribute much to the overall flux.

To assert the "worst-case-scenario" in the sense of affecting the conventional component of the muon flux, in this example a weight to each shower is applied, which contains *any* prompt muons, no matter how much energy they are carrying [16]. This type of weighting can be seen in the top panel of Figure 3.10. The reweighting of the whole shower only affects the conventional component very slightly and indeed less than the scaling via DYNSTACK. This can be understood with Figure 3.11, where the fraction of conventional muons (above 1×10^5 GeV) in a shower with any prompt muons is shown. At these muon energies most showers do not contain more than a handful of muons: the conventional muons are at a sub-promille level in prompt showers.
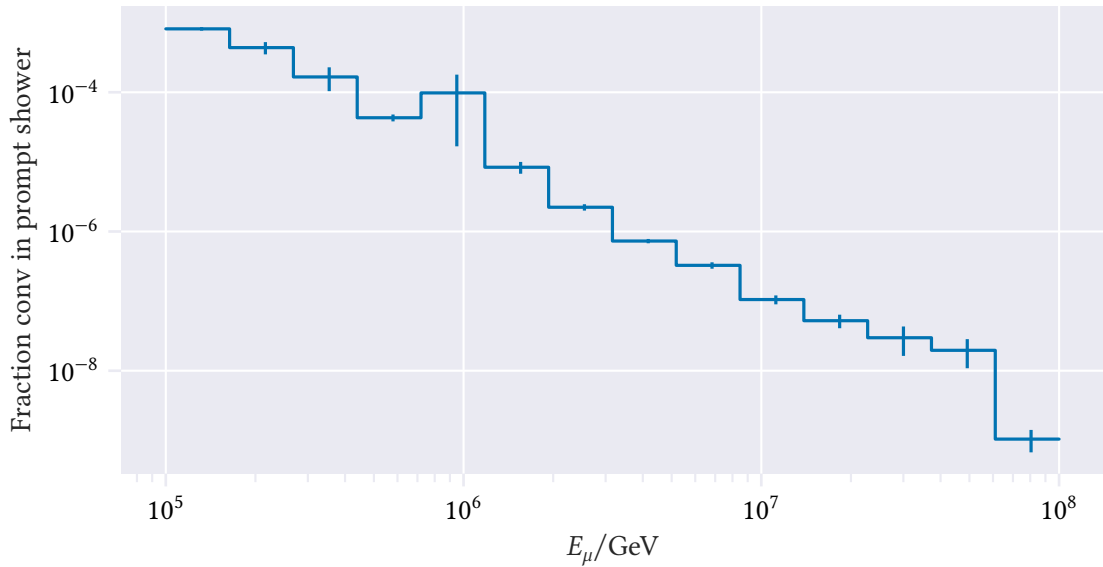
Figure 3.11: The fraction of conventional muons above the muon energy cut of 1×10^5 GeV in a prompt-tagged shower is binned. Here, a whole shower is tagged as prompt, if it contains any prompt muon (above 1×10^5 GeV).

This means, the conventional fluxes are not expected to be distorted at any meaningful level, if the leading muon is used to assign a whole shower as prompt. It must be noted, however, that

---

[16]Regard however, that no muons below 1×10^5 GeV exist, since they are cut away by the muon cut setting in CORSIKA7 for this MC set.

this picture might change, looking at the muon spectrum at very low energies on the order of GeV. There, muons might accumulate since they cannot have much less energy, otherwise they would decay, and the degree of distortion of conventional muons might be larger there.

The unchanging conventional flux might also be described as a downside of the reweighting method. The shower development is changed by the presence of prompt particles and this effect of a changing shower evolution is not modeled by applying a weight to the shower. The shower development is not expected to change drastically and indeed, that is why the two scaling methods in Figure 3.10 look so similar. The differences of the two methods are further summarized in table 3.2.

The reweighting changes the strength of the overall prompt flux, but does not modify its shape. It is possible to also modify the shape of the prompt component by introducing an energy dependent weight $n_{\mathrm{pr}}(E_\mu)$. With a proportionality of e.g. $E^{-\Delta\gamma}$, the spectral index could be changed by $\Delta\gamma$. In theory, this shape-changing reweighting has no limits and the whole flux could completely be reweighted to any given flux-model $\Phi'_{\mathrm{pr}}(E, \theta; \vec{p})$, [17] with arbitrarily many parameters $\vec{p}$, which all can be fitted to data. It is assumable though, that the flux prediction from the full MC simulation is one of the most accurate ones available in current theoretical calculations. MCEq might compete with a full MC calculation, but for example the *Z*-moment method assumes heavy simplifications of the cascade equations and internally also rely on event generators from hadronic interaction models. Thus, complicating the reweighting results most likely not in more accurate fluxes. It additionally complicates the easy interpretation of applying a constant weight.

Table 3.2: The difference between the two methods to change the strength of the prompt component is compared. "DYNSTACK" refers to the method of replacing prompt particles during the simulation with conventional ones, while "reweighting" refers to the method of applying a weight to the MC simulation.

	Pro	Con
DYSNTACK	• Changes shower development • Control the whole decay chain	• Computationally expensive • Correct physics is hard • Custom code
Reweighting	• Near 0 computation overhead • Taggable prompt component • Tried and tested software • Simple and easy interpretation	• No changes to shower development • EHISTORY complications

---

[17]The formula for the weight is similar to eq. (3.2), only that Φ_{p} is replaced with Φ_{pr}.

3.3.2 Fitting

Applying a weight only to the prompt component of the simulation allows fitting this weight to data from an air shower experiment. If the best fit value differs significantly from 0, this means that the prompt component is needed in the MC simulation to explain the data. The procedure is briefly outline here, and fully applied to IceCube data in the next chapter. The raw data of the experiment is used to reconstruct one or more variables per event, which behave differently in the prompt and conventional component, for example the zenith angle θ_{rec}, the leading muon's energy $E_{\mathrm{Leading}\mu,\mathrm{rec}}$ or seasonality d (day of year). While these variables are responsible for the different behaviour of the prompt component in the first place, also other variables which correlate to the probability of being prompt can be used, and these ones might be easier to reconstruct. An obvious candidate for this might be the energy of the whole muon bundle $E_{\mathrm{Bundle,rec}}$. Assuming that one target variable is used, this variable is then split up into N bins with edges $E_0, E_1, \ldots, E_N$ and the counts $C_1, \ldots, C_N$ in the bins are calculated for the data. The same thing is done for the MC simulation, only in there, the prompt and conventional component can be differentiated. Then each bin count contains the sum from both contributions

$$C_1^{\mathrm{MC}} = n_{\mathrm{pr}}C_1^{\mathrm{MC,pr}} + n_{\mathrm{conv}}C_1^{\mathrm{MC,conv}}, \ldots, C_M^{\mathrm{MC}} = n_{\mathrm{pr}}C_M^{\mathrm{MC,pr}} + n_{\mathrm{conv}}C_M^{\mathrm{MC,conv}}.$$

Here n_{pr} is the weight (or *normalization*) for the prompt contribution, and n_{conv} is the weight for the conventional contribution. The expected "bin count" $C_M^{\mathrm{MC,pr}}/C_M^{\mathrm{MC,conv}}$ in each bin is calculated by summing the weights from the MC simulation in that bin. The conventional weight is introduced, so also the conventional component can be fitted, if needed. This might be necessary to prevent the prompt component of filling up mismatched data/MC normalizations for the conventional component. For the sake of argument, the conventional normalization is left at $n_{\mathrm{conv}} = 1$. The total counts can be thought of as a function of the prompt normalization $C_i^{\mathrm{MC}} = C_i^{\mathrm{MC}}\left(n_{\mathrm{pr}}\right)$. Since this is a counting experiment, a Poisson-distribution is assumed in each bin, with an expectation value determined by the MC counts

$$p\left(C_i\right) = p_{\mathrm{poisson}}\left(C_i; \lambda\left(n_{\mathrm{pr}}\right) = C_i^{\mathrm{MC}}\left(n_{\mathrm{pr}}\right)\right) = \frac{\lambda\left(n_{\mathrm{pr}}\right)^{C_i} e^{-\lambda\left(n_{\mathrm{pr}}\right)}}{C_i!}.$$

The likelihood of observing the data then is given by

$$\mathscr{L}\left(n_{\mathrm{pr}}\right) = \prod_{i=1}^{M} p\left(C_i; n_{\mathrm{pr}}\right). \tag{3.3}$$

This likelihood is then maximized by varying n_{pr} to obtain the best fit value, or equivalently the negative logarithmic likelihood is minimized, which is computationally easier

$$-\ln \mathscr{L} = -\sum_{i=1}^{M} C_i \ln \lambda\left(n_{\mathrm{pr}}\right) - \lambda\left(n_{\mathrm{pr}}\right) - \ln C_i!. \tag{3.4}$$

Here, only terms including λ need to calculated for minimization. Then, with the best-fit value $\hat{n}_{\mathrm{pr}}$ a likelihood-ratio test can be performed. Assuming Wilks' theorem [Wil38], the test statistic

$$\Lambda = -2\ln\frac{\mathscr{L}\left(n_{\mathrm{pr}} = \hat{n}_{\mathrm{pr}}\right)}{\mathscr{L}\left(n_{\mathrm{pr}=0}\right)} = -2\sum_{i=1}^{M} C_i\left(\ln\lambda\left(\hat{n}_{\mathrm{pr}}\right) - \ln\lambda\left(0\right)\right) - \left(\lambda\left(n_{\mathrm{pr}}\right) - \lambda\left(0\right)\right) \qquad (3.5)$$

is χ^2 distributed with one degree of freedom. The null-hypothesis of $n_{\mathrm{pr}} = 0$ is rejected with a given confidence level of α based on Λ, if $\Lambda > s(\alpha)$ with $\chi^2(s) = \alpha$.

This weight-fitting is done in the forward-folded space of variables describing the detector response. There is another possibility of fitting the prompt component using unfolding: the detector data can be unfolded to obtain a physical flux Φ for high energetic muons (at the surface). The big advantage of unfolding is the universality of the result: The flux values obtained by unfolding describe the total muon flux and — amazingly — it does so in a mostly model independent way. The fit of the prompt component in the unfolded space is performed very similarly. In either case, in the end the prompt normalization is fitted and can be proven to significantly differ from 0 this way. For this procedure the prompt tagging is not even necessary, since only a theoretical model for the prompt flux is needed, which can be tested then. The tagging provides a theory prediction from a complete MC simulation, and can be tested as one of the models. An unfolding provides a full high energy muon flux in the end, which contains the contribution of the prompt part of the flux in a model-independent way.

3.4 Properties of the Prompt Component

While introduced to reweight the prompt component, the tagging of prompt particles can also be used to investigate the behavior of the prompt component in MC simulation. While the previous sections already asserted the energy and zenith dependent behaviors expected from the prompt component (see fig. 3.2), this section goes into further detail.

The spectral index of conventional muons is greater by one compared to prompt muons, thus prompt muons have on average more energy. While this may seem to imply that prompt muons also carry a greater fraction of energy from the primary particle than their conventional counterparts, the opposite is the case. This is shown in Figure 3.12, where the distribution of the fraction of primary energy for conventional muons is shown in the upper panel and for prompt muons in the panel below that. The 2D-histogram is normalized along the muon energy bins, so a column in a panel adds up to one. The blue crosses mark the mean μ in each column, while the height of the crosses show the standard deviation of the distribution in the column. The lowest panel shows the ratio of the means in each muon energy bin. The error bars for the ratio show the uncertainty on the ratio value, not the uncertainty of the distribution of the ratios, hence they are smaller compared to the uncertainties in the upper panel. Prompt muons carry on average somewhere between 35 % to 70 % of the energy of their conventional counterparts. This contra-intuitive behaviour is understood through simple reasoning: prompt mother particles

are produced much more rarely than conventional particles, even at high energies, they only decay earlier. This means that it is more likely that prompt mother particles are created deeper in the shower, where many more muons have been created already.
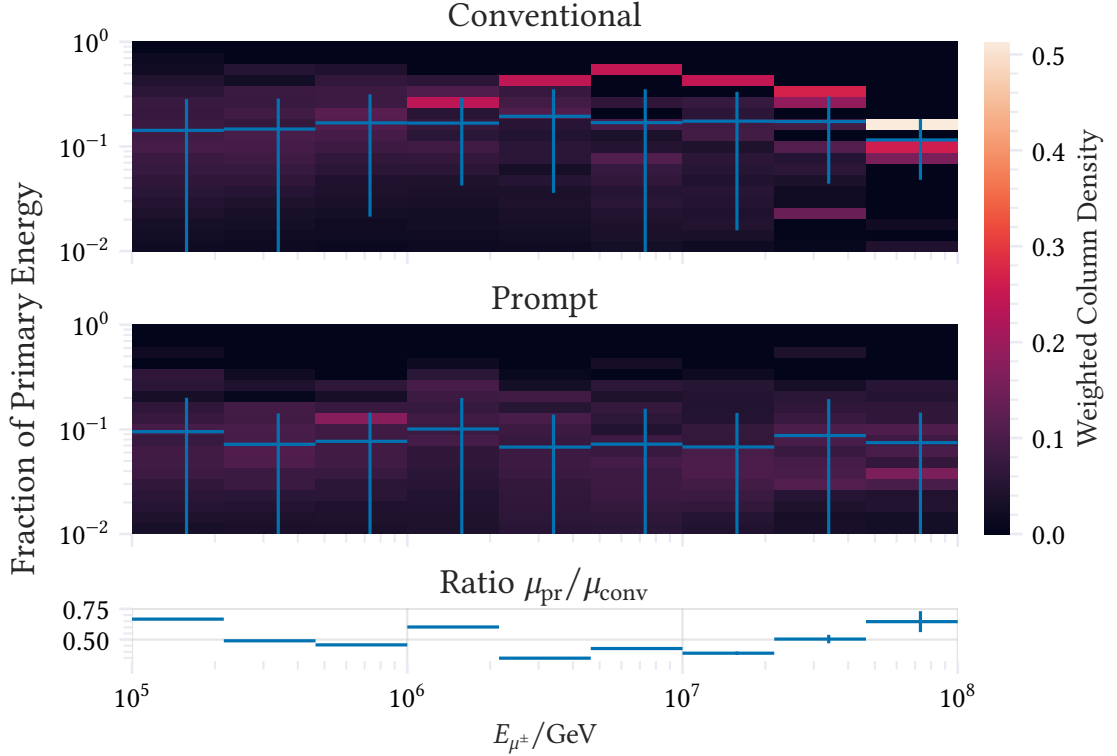

Figure 3.12: The fraction of the primary energy a muon carries is visualized in a 2D Histogram. It is normalized column-wise, so a column adds up to 1. The events in each column are weighted with the GSF primary model. The blue crosses show the mean and standard deviation of the distribution in each column. The top panel contains all prompt muons, the center panel the conventional muons and the lowest panel shows the ratio of the prompt mean value to the conventional mean value, where the error bar refers to the standard deviation of the mean value, not the distribution.

As seen from Equation (2.22) theoretical calculation of lepton fluxes at sea level using the Z-moment method give results for lepton fluxes from each parent particle type H in the form of

$$\Phi_\mu\big(E_\mu, \theta\big) = \Phi_{\mathrm{p}}\big(E_\mu\big) \frac{\mathscr{A}}{1 + \mathscr{B}\frac{E_\mu}{\epsilon_h}\cos\theta}. \tag{3.6}$$

Were Φ_{p} is the primary flux at the muon energy and ϵ_h is the critical energy for a given parent hadron. For prompt particles $E_\mu \ll \epsilon_h$ and this results in the known relation $\Phi_\mu \propto \Phi_{\mathrm{p}}$. For conventional particles $E_\mu \gg \epsilon_h$ and this results in the relation $\Phi_\mu \propto \Phi_{\mathrm{p}}/E_\mu/\cos\theta$. The factors A and B contain the spectrum weighted Z-moments and are also energy dependent, although this energy-dependency is not very large compared to $1/E_\mu$. This behaviour is approximately

asserted in Figure 3.13, where indeed the $1/E$ slope of the conventional component can be seen. The prompt component varies only comparatively little up to 1×10^8 GeV, where the critical energy of the charmed mesons is expected to be exceeded and thus also the charmed mesons follow Φ_{p}/E_μ.
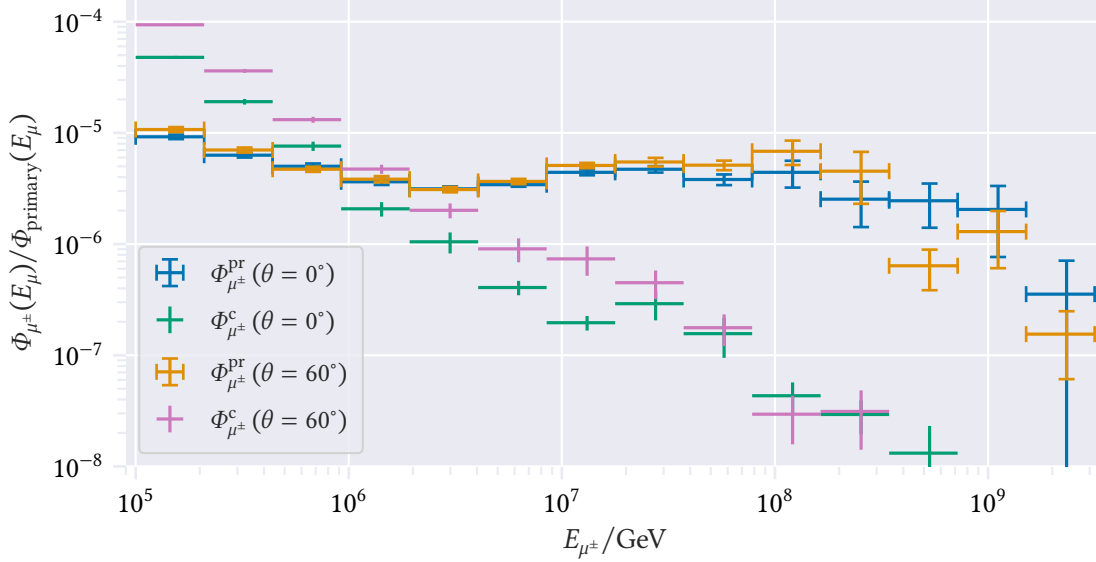
Figure 3.13: The muon flux (weighted using GSF), divided by the flux of the primary particle *at the muon's energy* is binned. The spectrum is divided into the prompt (pr) and conventional (c) component for 0° and 60°. The approximately flat shape of the prompt component up to 1×10^8 GeV can be seen, as well as the approximate proportionality to E^{-1} for the conventional component.

To assert that the values shown in Figure 3.13 are consistent with theoretical predictions, the values given in [GMS15] are translated to the values shown in figure. Comparing Equation (3.6) in the region below the critical energy with Equation (2.20) and Equation (2.23), it reads

$$\frac{\Phi_\mu}{\Phi_{\mathrm{P}}} \approx \mathscr{A} = Z_{H\mu} \frac{Z_{NH}^d}{1 - Z_{NN}}.$$

Estimating from Figure 9 of [GMS15], the Z_{NH} ranges between approximately 1.3×10^{-4} to 3.5×10^{-4} for the sum of charmed hadrons $D^0, D^+, D_s^+, \Lambda_c^+$. They use the (energy dependent) Z_{NN} values of [Bha+15], which give a value of $Z_{NN} = 0.271$ at $E = 1 \times 10^3$ GeV and $Z_{NN} = 0.231$ at $E = 1 \times 10^8$ GeV. As neither [GMS15] nor [Bha+15] provide their calculated values for $Z_{H\mu}$ directly, $Z_{D\mu} \approx 0.03$ is estimated based on Appendix A of [Bug+98], which both papers provide as a reference. This means an estimate at the lower energy range of

$$\mathscr{A} = 5.7 \times 10^{-6}$$

and at the higher end of the energy range of

$$\mathscr{A} = 1.4 \times 10^{-5}.$$

45

These are approximately consistent with the flux fraction of the prompt component seen in Figure 3.13, which is on the order of 10^{-5}.
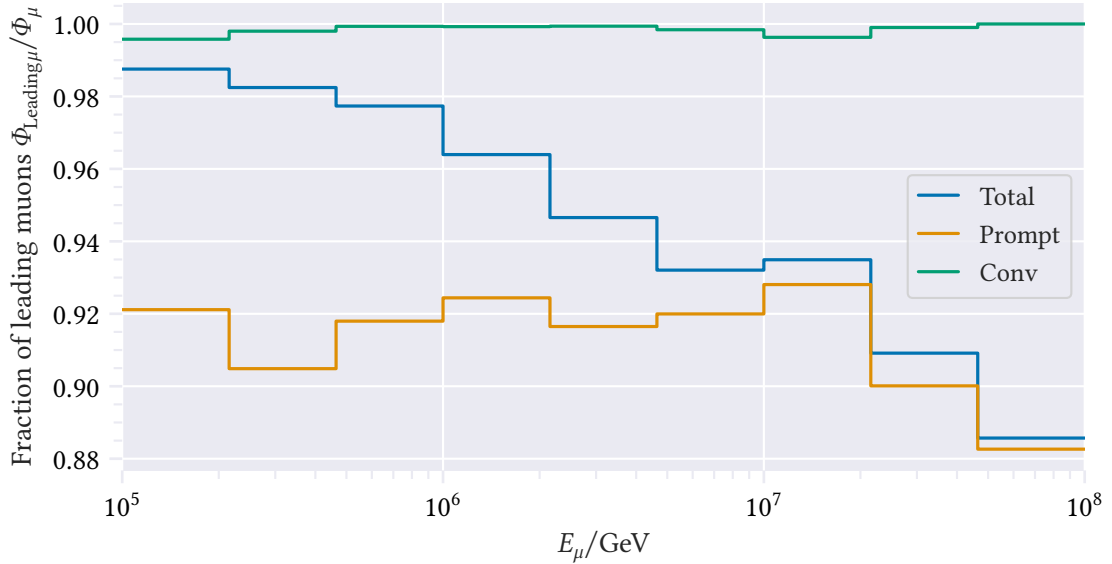
Figure 3.14: The GSF-weighted fraction of leading muons per energy bin, divided into prompt and conventional is shown. For example, a value of 0.9 in one bin means, that 90 % of the total muon flux in this energy bin is coming from leading muons. A leading muon is the most energetic muon inside a shower.

As described earlier, the single muon flux usually cannot be resolved by an air shower detector. What is resolved is for example the muon bundle or the leading muon flux. Most of the single muon flux in our energy range is coming from leading muons, as shown in Figure 3.14. There the leading muon flux divided by the total muon flux in each energy bin is shown by the blue line. Additionally, the leading conventional (prompt) muon flux divided by the total conventional (prompt) flux is shown in green (orange). The transition of the total flux line from the conventional to the prompt line indicates the transition from conventional muons dominating the spectrum to prompt muons dominating.

The reason why prompt muons seem to have a lower probability of being the leading muon is the same reason why they carry on average less energy of the primary particle: they are on average produced later in the shower, since prompt parent particles are created more rarely.

46

4 Finding the Prompt Component with IceCube

In this chapter the lessons learned from the previous chapter are applied in the context of IceCube. The goal is to significantly discover the prompt component of the atmospheric muon flux. In this chapter the prospect of this goal with the 10 years of available IceCube data is studied using the methods described in the earlier chapter. The whole analysis is still under development at the time of writing this thesis, so no complete analysis with actual IceCube data is performed, but everything is based on Monte Carlo (MC) studies.

The MC simulation in IceCube are explained in Section 4.1. The reconstructed variables from the detector response are introduced in Section 4.2. The prompt tagging and reweighting procedure described in the previous chapter is applied in Section 4.3.

Additionally the chosen filters are explained in Appendix C.1 and the MC simulation's validity is checked against a small "burn-sample" of real data in Appendix C.2.

4.1 Monte Carlo Simulations for IceCube

The MC sample used in the previous chapter chapter 3 is produced by CORSIKA7 and contained muons at the ground-level. To describe IceCube's data from extensive air showers (EASs), this is only the first step in a chain of simulation softwares. The chain can be outlined as

EAS simulation (CORSIKA7) → Muon propagation (PROPOSAL) →
Photon propagation (SNOWSTORM+CLSIM) →
Detector Response (SNOWSTORM) → "Level1" and "Level2" Filters.

The details of the first step have already been explained in the previous chapter. The propagation of muons from the surface to the detector and calculation of their energy losses is handled by PROPOSAL [Koe+13]. CLSIM produces and propagates the Cherenkov photons to the Digital Optical Module (DOM)s, where the detector response is then simulated. SNOWSTORM handles systematic uncertainties in IceCube and samples systematic parameters for the ice model as well as the detector response [IC19]. The "Level1" filters are filters applied to data directly at the South Pole. The "Level2" filters are filters applied to the data in the North. With the simulation chain a detector response from the primary particle inducing an EAS is obtained, so its detector signature can be investigated. The injected CORSIKA7 simulation is listed in Table 4.1.

To verify that the prompt tagging procedure is also working using the IceCube software, a comparison plot for tagging and MCEq is shown in Figure 4.1 (similar to Figure 3.2). The difference there is that the IceCube MC simulation samples the whole zenith range from 0° to

Table 4.1: The dataset used in the IceCube simulation pipeline. The energy interval is divided into four different disjoint regions so that enough statistic is produced in the high-energy region, which is especially interesting for this analysis. In each energy region 5 different primary particles are simulated: H1, He4, N14, Al27, Fe56, with a fraction of 10:5:3:2:1 and a spectral index of $\gamma = 2$.

$E_{\min}/\text{GeV}$	$E_{\max}/\text{GeV}$	N
6.0×10^2	1.0×10^6	1.0×10^6
1.0×10^6	1.0×10^8	2.0×10^5
1.0×10^8	1.0×10^9	1.0×10^5
1.0×10^9	5.0×10^{10}	1.2×10^3

90°, while in the last chapter only two discrete zenith angles were shown. Thus, the values of the IceCube MC dataset for the conventional flux lie somewhere between the 0° and above 60° degree MCEq fluxes.
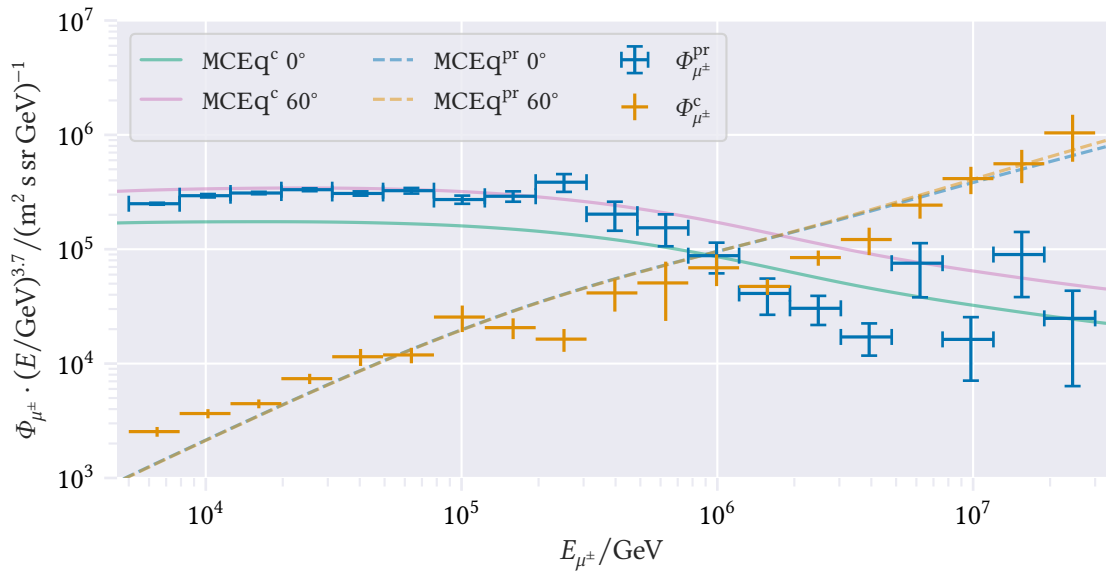
Figure 4.1: The tagging procedure applied in the IceCube simulation pipeline *before* detector simulation (crosses) compared to MCEq results (lines) is shown. The flux is given at ground-level and is weighted with the Global Spline Fit (GSF) primary model.

With the prompt tagging, it is testable how events with a prompt leading muon behave and look in the detector compared to conventional events. A comparison of an event topology is shown in Figure 4.2. Both the event with a prompt leading muon (left, from hereon called "prompt events") and a conventional leading muon (right, "conventional event") have a large muon bundle inside the detector, with over 1800 muons, but most of the energy is carried by the leading muon. Both are high energy events with primaries of a few hundred PeV, which
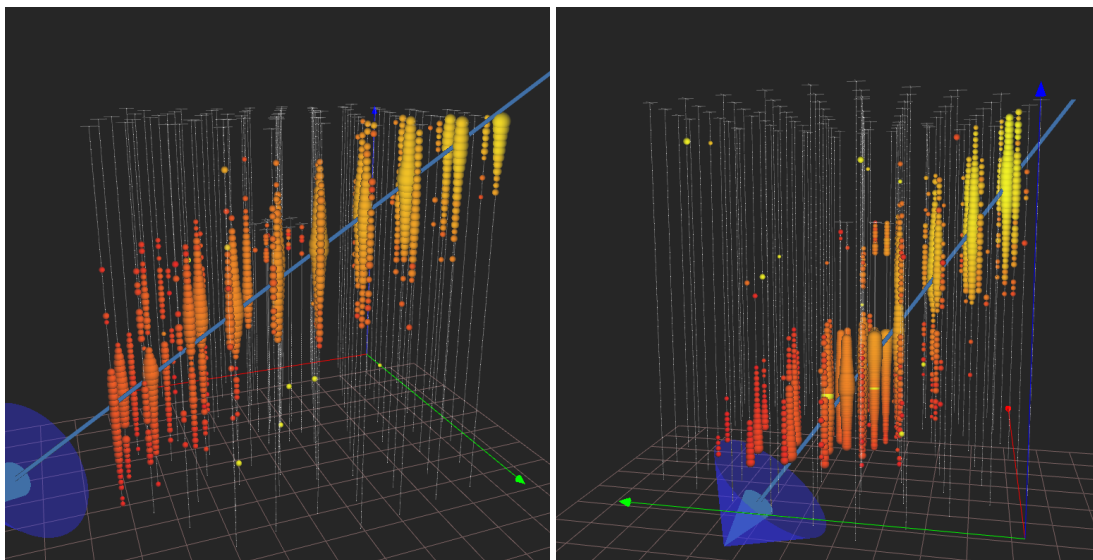
Figure 4.2: Two event displays of two atmospheric-muon events from the MC simulation, of which one has a prompt leading muon (fig. 4.2a) and the other has a conventional leading muon (fig. 4.2b). The events are chosen so that they are relatively similar. The prompt event has a leading muon energy of 1.2 PeV and a bundle energy of 1.6 PeV with a muon multiplicity of 1812, coming from a primary with an energy of 875 PeV. The conventional event has a muon energy of 1.05 PeV, a bundle energy of 1.8 PeV with a muon multiplicity of 1880, which was produced from a primary with energy 379 PeV. The size of a bubble corresponds to the total charge deposited in the DOM, while the color corresponds to the time the charge was deposited from early (yellow) to late (orange).

are expected to happen a few times per square kilometer per year. No visible distinction exists between the event, and this is expected: prompt and conventional muons behave the same inside the detector. The prompt component can only be discovered by distributions of the variables in which they differ (energy, zenith, seasonality).

4.2 Reconstruction

In real data the true information about the properties of the EAS are not accessible, they must be reconstructed. There are a number of different methods in IceCube to reconstruct variables from events. These include different likelihood-based reconstruction algorithms for energy and direction. For most of the history of IceCube these likelihood-based algorithms produced the best results, but recently there has been fast progress in machine learning-based methods in IceCube. Deep Neural Networks (DNNs) made the 4.5σ discovery of neutrinos from the galactic plane via cascade events possible [IC23a] and a new Graph Neural Network (GNN) framework for neutrino telescopes [Søg+23] already reports promising results. The reconstruction methods

used in this chapter are based on the same DNN software framework used in the galactic plane analysis [Hue23; IC21]. The exact layouts and training procedure are described in Ref. [Bra23; Flo23]. The reconstruction DNNs still need further investigation and verification before applying them in the final analysis. While the reconstructions are improvable for the analysis in the end, these preliminary reconstructions already show promising results for the analysis. It is expected that the analysis will not show a big decrease in sensitivity, if conventional reconstruction methods are used, although further investigation is needed to verify this.

The complete IceCube detector (IC-86) began operations in 2011 [IC17], so at the time of writing this thesis, 12 years of IceCube data is available. For this reason the event count for 10 years of data is shown in the following plots, so the order of magnitude of the available data is comparable to the figures.

When a muon bundle deposits energy in the detector, the natural physical variable to estimate is the energy of the whole bundle, since it is not easy to disentangle the contribution of a single muon to the energy losses. A usable distinction between the prompt and conventional showers in dependence of the bundle energy in Figure 4.3a is seen, although the transition from conventional to prompt is less pronounced than expected from Figure 2.5. The reason for this is that the bundle energy correlates with the leading muon energy, but it is smeared out. When displaying the transition in terms of the leading muon's energy in Figure 4.3b, the transition is below 1 PeV, as expected.

(a) Muon bundle energy

(b) Leading muon energy
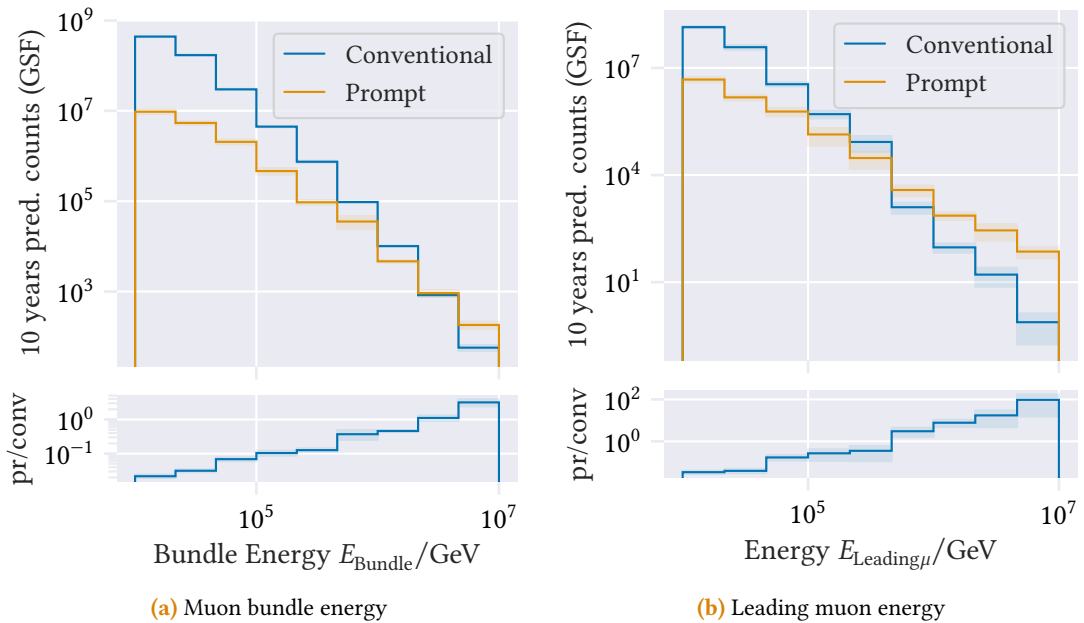
Figure 4.3: The expected event counts for prompt and conventional events with 10 years of IceCube data assuming the GSF primary model. The *x*-axis shows the MC truth values. The bottom panel shows the ratio of conventional to prompt muons in each bin. Overflow bins are omitted, so the two distributions do not sum up to the same number of total events, although the sample is the same.

To find a reasonable estimator for the leading muon energy is challenging. There are three available options:

1. Only use single-muon events.

2. Reconstruct the leading muon energy.

3. A combination of 1.& 2.

Since the prompt component becomes relevant at high energies and the muon number in a shower is proportional to the energy, there is no expectation of single muon events at the energies interesting in this analysis. Low energy muons stop somewhere in the ice before reaching the detector. The energy threshold for reaching the detector depends on the amount of ice over the detector and therefore on the zenith angle. This means that in higher zenith angles, single muon events are detected up to a higher energy, but the statistics are also decreased, because of the restricted zenith band. Consider the following events: 100 1 TeV compared to 50 1 TeV muons with one 50 TeV muon. Both have the same energy, but the deposited losses are expected to be more continuous in the first case, than in the second. Thus, there might be a mechanism to estimate the leading muon's energy. The third option is the option best suited for the final analysis: Produce a selection containing events, with an easily reconstructable leading muon energy. Such as events where the leading muon carries a significant amount of the bundle's energy. A compact comparison of how pronounced the transition of prompt and conventional muons is, is depicted in Figure 4.4. While a DNN reconstructing the leading muon energy (second option) is used in this chapter, the reconstruction can not be believed to be good: Reference [Flo23] shows that the DNN mainly predicts the bundle energy and the predicted leading energy is just a fraction of this bundle energy. Nonetheless, this highly approximate reconstruction is enough for the proof-of-concept toy analysis presented in Section 4.3.

The zenith distribution is also expected to differ for prompt and conventional muons, see Figure 2.6. Figure 4.5 shows the zenith distribution of the events in the MC dataset. The prompt component is indeed flat, as expected, but the conventional component does not seem to have the approximate $1/\cos\theta$ dependency, but also appears flat. The difference to the theoretical zenith dependency at the surface is the propagation through the ice, this can explain the difference since in the flat earth approximation muons loose energy with $\cos\theta$. But Figure 4.5 only shows events above 1 PeV, so this effect should not be noticeable except for very high zenith angles. The energy cut in this plot is at 1 PeV to bring the conventional and the prompt flux down to the same level.

A bigger insight into these important two analysis variables can be gained when displayed simultaneously. This is done in a two-dimensional histogram for all muon events in Figure 4.6, where also the marginalized distributions are shown. Most events in this energy range still come from conventional muons, so the marginalized zenith distribution for all energies rises with zenith, as expected. The bins in a column become more uniform for higher energies, as expected, since the prompt component starts to dominate. The same figure is shown divided into prompt, conventional and the reconstructed variables in Figure 4.7. The prompt component (right-hand side) is approximately constant in the zenith distribution over the whole energy
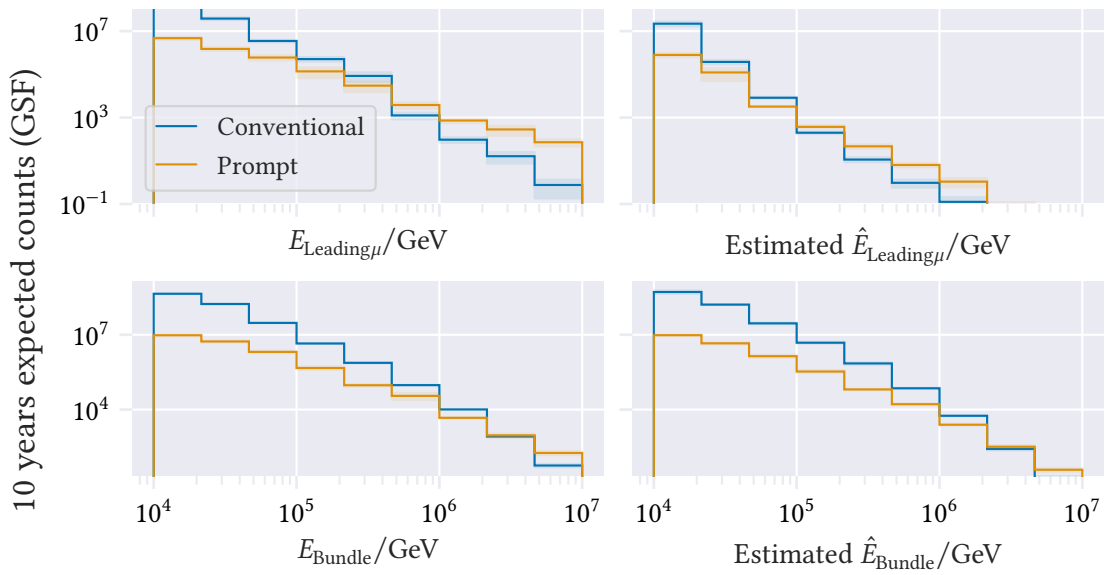
Figure 4.4: The number of conventional and prompt events expected for 10 years of IceCube-data. The left panels show the MC truth and the right ones show the reconstruction on the MC set. In the upper panels the leading muon energy is displayed, while the lower ones show the bundle energy. For weighting, the GSF model is used. Overflow bins are omitted, thus the sum of the bins are not equal for each plot, although the same dataset is used.

range, while the zenith distribution for the conventional component (left-hand side) favors high zenith values. This effect decreases for high energies. The lower panels with the reconstructed variables show a mismatching behavior especially at the low energy border.

In order to improve the reconstruction of the leading muon's energy, events where the leading muon contains a significant amount of the whole bundle energy are favorable to select. Most high energy events have a muon which carries most of the energy and the distribution, as depicted in Figure 4.8. The distributions do not differ much for prompt and conventional muons, so no bias is created, if a leadingness based selection is performed.
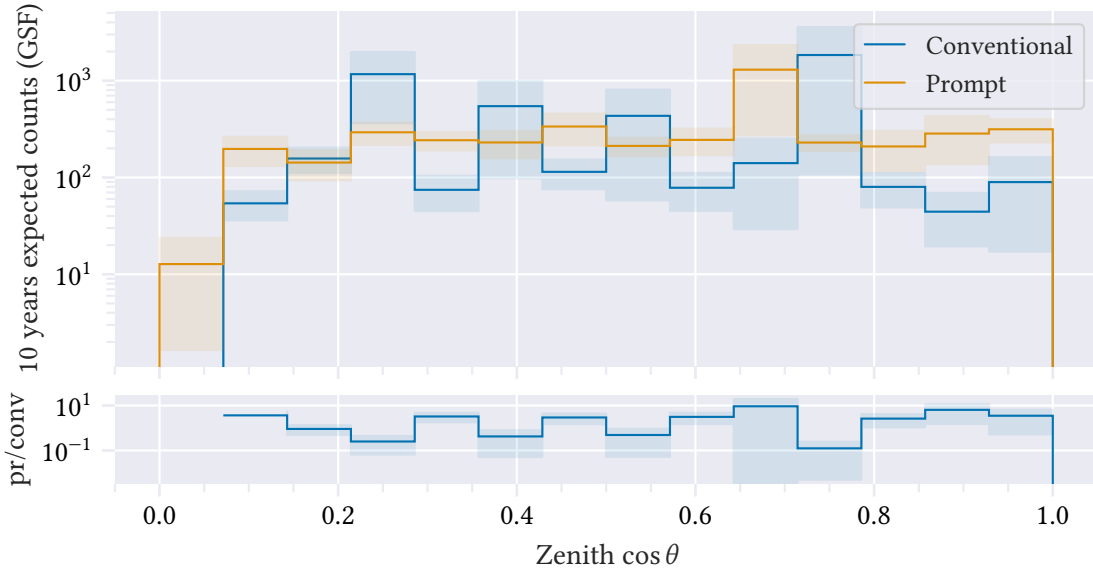
Figure 4.5: The expected prompt and conventional zenith distribution of events with a leading muon energy above 1 PeV. The bottom panel shows the ratio of prompt to conventional events.
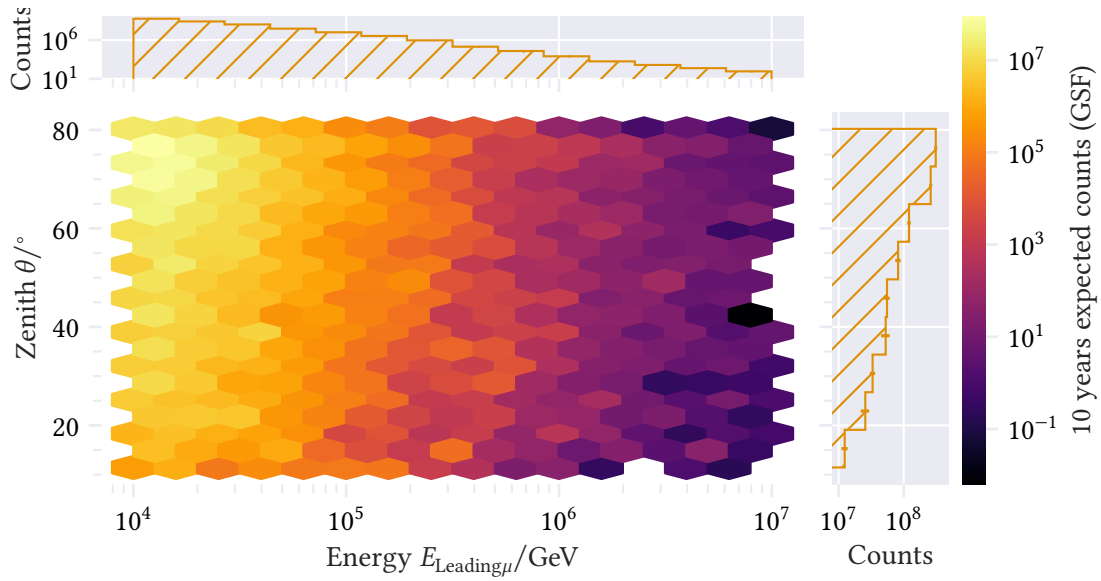
Figure 4.6: Expected even rates for the two-dimensional histogram using the GSF primary model. The *x*-axis shows the leading muon energy and the *y*-axis the zenith angle. The marginalized distribution over each axis is shown in the histograms.
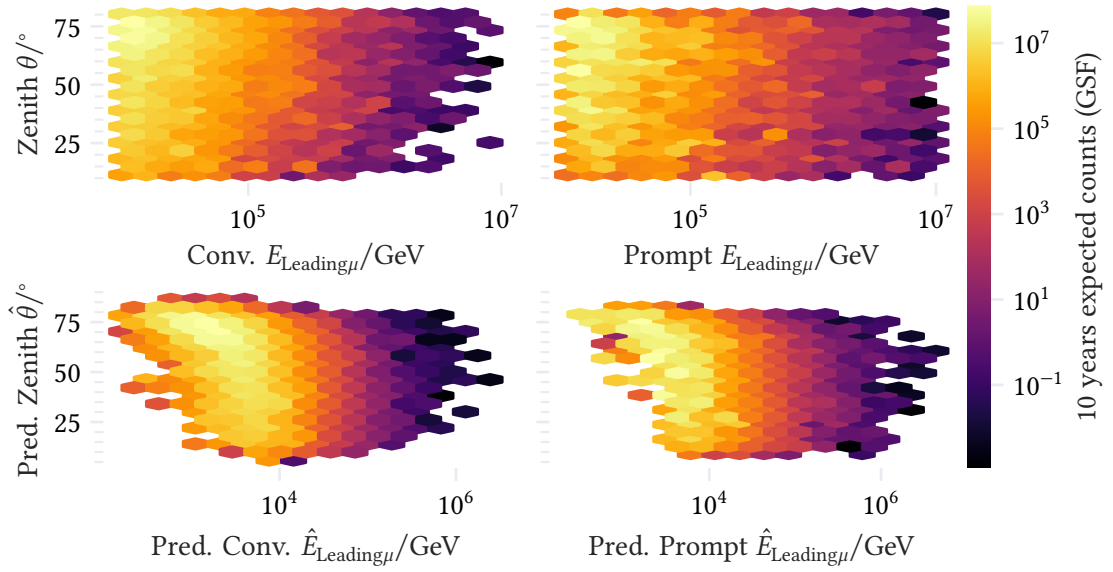
Figure 4.7: The expected event rates for 10 years of data are depicted. Each *x*-axis shows the leading muon energy and each *y*-axis the zenith angle. The histograms are divided into conventional (left) and prompt (right) events as well as true MC values (top) and reconstructed ones (bottom).
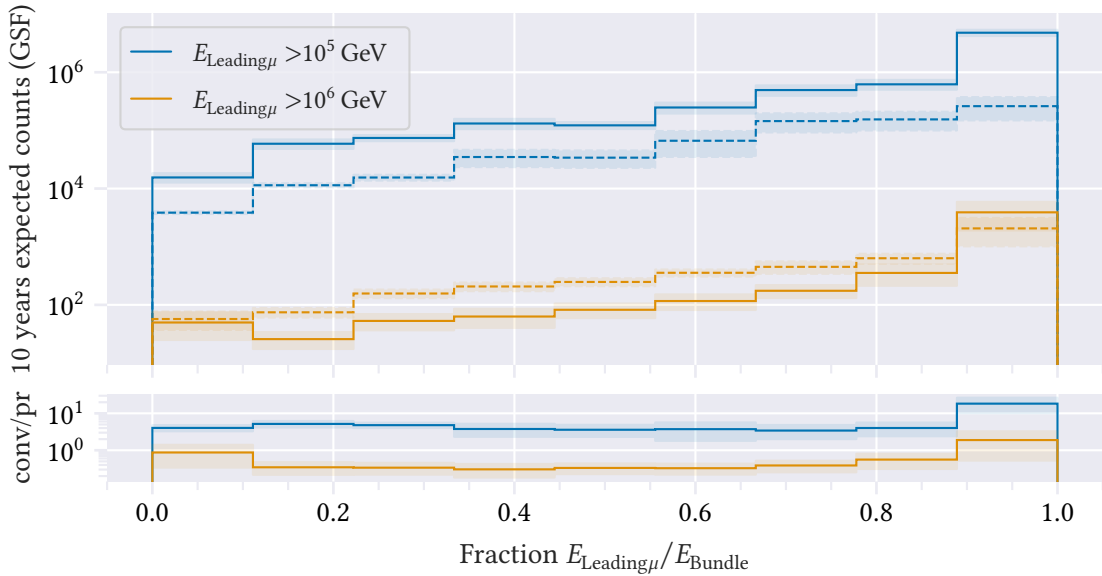
Figure 4.8: The distribution of the leading muon energy fraction is depicted. The dashed lines show the distribution for prompt leading, while the solid lines show the distribution for conventional leading muons. The energy cut of 1×10^5 GeV (blue) corresponds to a value below the crossover point, and the energy cut of 1×10^6 GeV (orange) is above the crossover point for conventional and prompt events.

4.3 Analysis

The potential of the proposed method of fitting the prompt normalization n_{pr} is verified in this chapter. This is done for a toy MC dataset, which is generated for a detector livetime of $T = 10\,\mathrm{yr}$. The toy dataset consists of N events from the MC set, which are randomly drawn from the whole MC so that the probability of event i being drawn is $w_i / \sum_i w_i$. The weight also contains the prompt normalization n_{pr}, if the event is tagged as prompt. N is drawn from a Poisson distribution with mean $\lambda = T \sum_i w_i$. This results in a set of events, which then do not have associated weights anymore, and may be drawn multiple times. Since the MC set is focused towards high energies, low energy events are heavily oversampled here. Beyond this proof-of-concept toy analysis this is something which needs to be improved. This procedure of drawing pseudo datasets for 10 years is visualized in Figure C.14, for different injected strengths of the prompt normalization. The expected rate from weighted MC simulation is shown in addition to the unweighted pseudo data. The goal is, to adjust the prompt weight n_{pr} of the weighted MC simulation so that the prompt strength of the (pseudo) dataset is matched (which is in the toy MC study just the injected strength). Additionally, a weight n_{conv} is also applied to the conventional component, which is always injected with $n_{\mathrm{conv}} = 1$. This prevents the prompt weight to fit any mismatch in the overall normalization of the conventional component in the end. This fitting procedure has already been described in greater detail in Section 3.3.2.

For this toy analysis only the reconstructed leading muon energy has been chosen as an analysis variable. A 2D fit also to the reconstructed zenith has been tested as well, but did not show any significant improvement, so for the sake of simplicity only the energy is fitted. The selection is very currently very simple and consists alongside the muon filter only of a cut to the reconstructed bundle energy requiring $\hat{E}_{\mathrm{bundle}} > 100\,\mathrm{TeV}$. With these selections around 5.9 million events for 10 years of data with the GSF primary model are expected. The analysis bins are chosen to be seven logarithmically uniform energy bins from 5 TeV to 2000 TeV. They are shown in Figure 4.9, where also the MC expectation for prompt and conventional is shown in each bin. The blue line shows how the data rate in each bin is affected by the cut on the bundle energy.

To evaluate the potential significance of the fit, it is performed repeatedly to collect statistics about the result. In each repetition a new pseudo dataset is sampled and the result of the fits ($n_{\mathrm{pr,fit}}$, $n_{\mathrm{conv,fit}}$ and the test statistic Λ from Equation (3.5)) are saved. This is referred to as one *trial*. The null hypothesis H_0 in this test is that there is no prompt component of atmospheric muons, so $H_0 : n_{\mathrm{pr}} = 0$. Assuming, that the dataset is large enough to assume Wilks' theorem, the test statistic Λ is χ^2-distributed with as many degrees of freedom (DOF) as the fit contains. For a fit where only the prompt normalization is fitted, the DOF would be one. Since the conventional normalization is also fitted, the DOF are higher, but not equal to two, since the two parameters are correlated through the overall normalization. To assert the applicability of Wilks' theorem, 2000 background trials are performed and a χ^2 distribution is fitted to the distribution of Λ. This can be seen in Figure 4.10. The DOF are indeed fitted to ca. 1.5. There
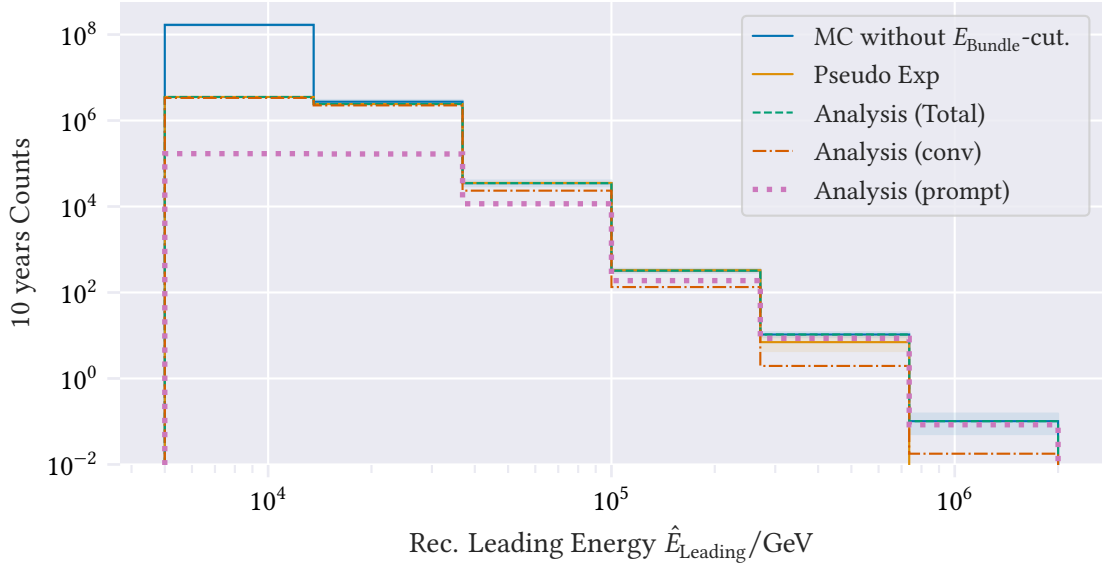
Figure 4.9: The expected distribution of the reconstructed leading energy with 10 years of data and the cut on the leading muon energy. The binning corresponds to the binning used in the toy analysis for fitting. It is also divided into the prompt and conventional component alongside with a sampled pseudo data sample from the MC set.

also the η value is given, which is close to 0.5. It is defined as

$$\eta = \frac{N(\Lambda \leq 0)}{N}.$$

Here $N(\Lambda \leq 0)$ is the number of trials where the test-statistic is smaller than zero and N is the total number of trials. A trial where the test-statistic is smaller than zero may seem impossible, since that means that the fitted value $\hat{n}_{\mathrm{pr}}$ is less likely than the null hypothesis. $\eta = 0.5$ stems from the fact that $\hat{n}_{\mathrm{pr}}$ is restricted to be non-zero in the fit, since a negative value is not physical. But n_{pr} is injected as 0 in the background trials, so the best fit value is expected to fluctuate symmetrically around 0, so half of the fits should have $\hat{n}_{\mathrm{pr}} < 0$. This is not allowed, so a positive value must be fitted which is then less likely than $n_{\mathrm{pr}} = 0$.

Figure 4.11 shows the distribution of the test statistic for different injected prompt normalizations. It shows that the distributions deviate more from a χ^2 for higher injected normalizations, as expected. Already at $n_{\mathrm{pr,inj}} = 0.03$ most of the trials generate a test statistic that deviates more than 5σ from the mean of the fitted χ^2 distribution.

It has to be guaranteed, that for any injected prompt normalization, the fit reproduces the correct value for the normalization. This is tested in Figure 4.12, where the fitted prompt normalization in dependence of the injected one is shown for both the fit that only fits the prompt normalization (left) and the one that also fits the conventional normalization (right). There seems to be a small bias towards higher fitted prompt normalizations if the injected norm is smaller than 1 %. The conventional normalization is always correctly fitted no matter what
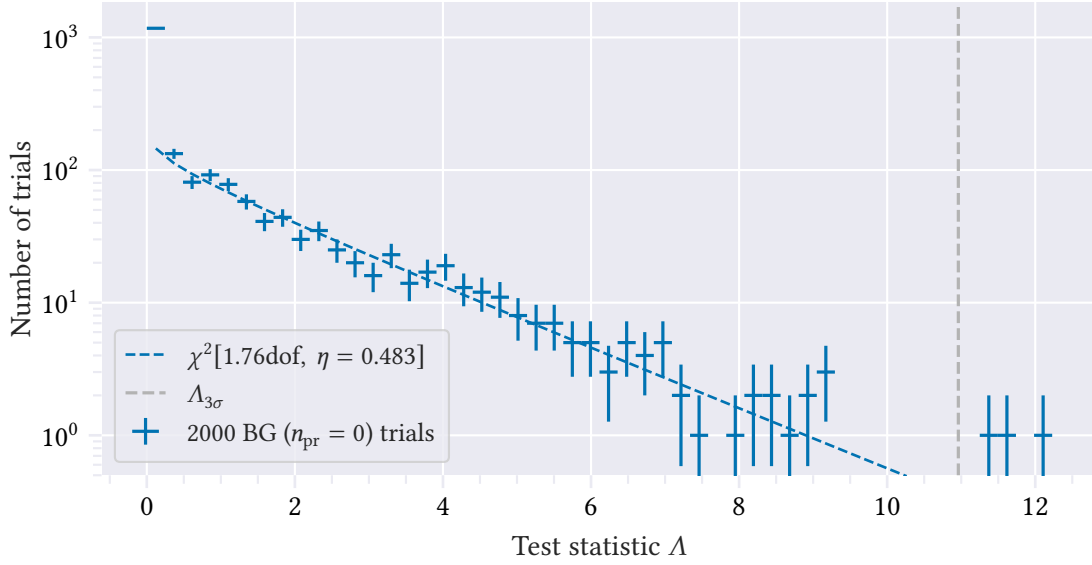
Figure 4.10: The distribution of the test statistics for 2000 background (no prompt component) trials. The test statistics Λ is the logarithmic likelihood ratio of the fit compared to the null-hypothesis. In the fit the prompt as well as the conventional normalization is fitted, so the fit has two free parameters, which are, however, not completely uncorrelated. To that distribution a χ^2 distribution is fitted.

the injected prompt normalization is: The minimum fitted value for all trials across all injected prompt normalizations is 0.998 and the maximum is 1.001 .

The 5σ discovery potential is defined as the prompt normalization at which 50 % of all trials result in a test statistic with a significance of 5σ or more. With the expected statistic for 10 years of IceCube data with the GSF primary flux model, the 5σ discovery potential is

$$n_{\mathrm{pr}}^{5\sigma} = (3.24 \pm 0.13)\,\%. \tag{4.1}$$

The sensitivity is defined as the prompt normalization which results in a distribution of test statistics, where 90 % of all trials result in a test statistic larger than the median of the distribution of the test statistic under the null hypothesis. With the expected event number for 10 years of IceCube data with the GSF primary flux model, the sensitivity is

$$s_{\mathrm{pr}} = (0.79 \pm 0.03)\,\%. \tag{4.2}$$

The same toy analysis is performed without fitting the conventional normalization and has very similar results. For a one-year analysis the 5σ disovery potential is $(10.17 \pm 0.48)\,\%$ and the sensitivity is $(2.43 \pm 0.09)\,\%$, as approximately expected from a quadratic decrease in statistics.
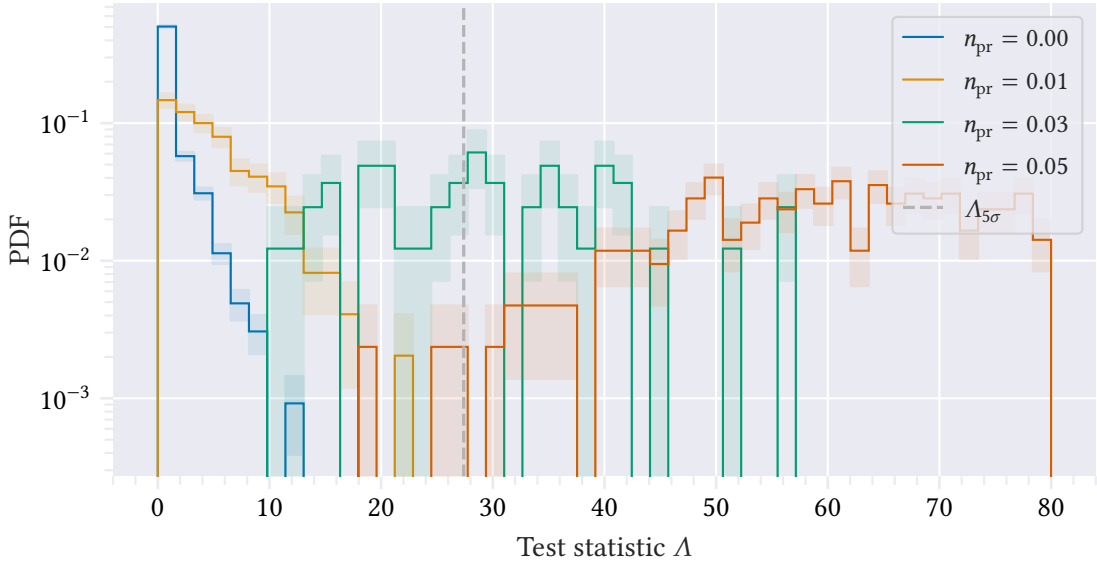
Figure 4.11: The distribution of the test statistics for different injected prompt normalizations. The prompt and conventional normalization is fitted. The required test statistic for a 5σ discovery is marked in the plot.
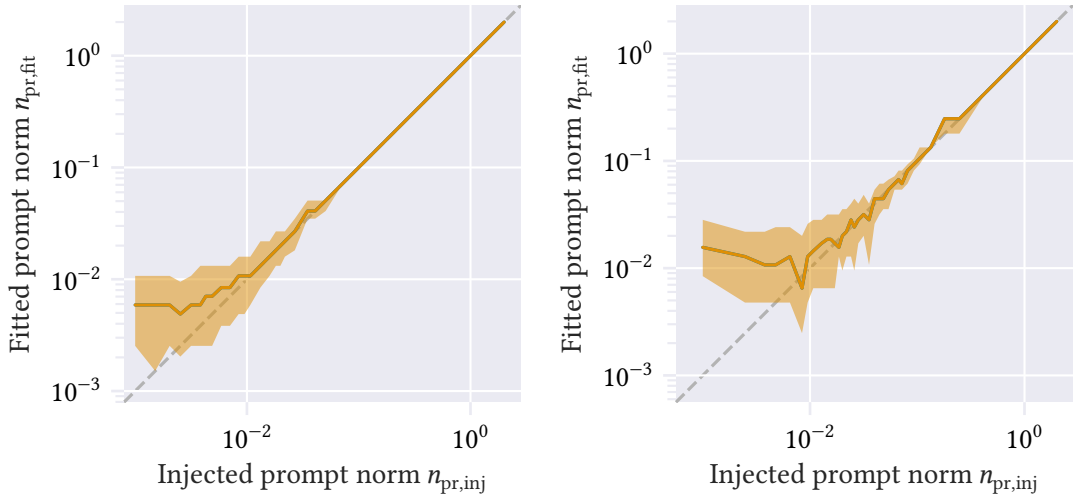
(a) Without conventional normalization fitted.

(b) With conventional normalization fitted.

Figure 4.12: The fitted vs. injected prompt normalization, the range of one standard deviation of all trials is shown around each value. Left the bias for the fit without the conventional normalization is shown and on the right the conventional normalization is also fitted.

5 Conclusion and Outlook

This thesis developed a method to distinguish (or *tag*) *conventional* and *prompt* muons in the extensive air shower (EAS) simulation software CORSIKA7 using its extended history (EHISTORY) option. An inclusive prompt muon flux calculated from a full Monte Carlo (MC) EAS simulation is reported. The prompt and conventional fluxes are consistent with numerical solutions to the cascade equations via MCEq. The influence of different state-of-the-art Cosmic Ray (CR) flux models on the prompt component is tested. Different definitions of which particles contribute to the prompt component are compared. This work suggests to use the simplest definition of the prompt flux: A muon from a pion or kaon decay is conventional, all others are prompt. The behavior of the prompt component in MC simulations is analyzed. The investigations show that prompt muons on average carry a smaller fraction of the primary energy than their conventional counterpart. Furthermore, on average, prompt muons carry a smaller fraction of the muon bundle energy — they are less "leading". Alongside this thesis the open source python package PANAMA was developed [Nes23], which provides user friendly utilities to work with CORSIKA7. Features of PANAMA include tagging of the prompt component, loading of the EHISTORY output, weighting and running CORSIKA7 in parallel.

Using the muons tagged as prompt, their weight in the MC simulation can be fitted to data from a high energy muon detector in the forward folded space. The tagged fit is proposed as a method to significantly discover the prompt component. To analyze the prospect of the suggested prompt analysis, a toy MC study is set up for the *IceCube* detector. The tagging is implemented into the IceCube software. The variables in which the prompt component is expected to differ are most importantly the energy and zenith. Since the zenith distribution has a less clear separation between the prompt and conventional fluxes, the toy analysis only uses the energy. While the leading energy shows the clearest transition from conventional to prompt, the bundle energy also transitions between conventional and prompt. In this toy MC study, a 5σ discovery potential of $(3.24 \pm 0.13)\,\%$ of the prompt flux predicted by the hadronic interaction model SIBYLL2.3d and a sensitivity of $(0.79 \pm 0.03)\,\%$ with 10 years of IceCube data is expected. While the analysis is at a very early stage, the discovery potential hints towards a promising analysis.

To finalize the analysis, the used zenith and energy reconstructions need to be verified and improved. The used simulation dataset is not large enough for an analysis on the final scale. A large scale simulation matching the statistics of about 10 years of IceCube data needs to be produced. Finally, systematic uncertainties need to be considered. After the event selection is finalized, a proper *unfolding* on the obtained dataset of the high energy muon spectrum can be

performed. With this model-independent physical spectrum, different theoretical calculations of the prompt component of the muon flux can be tested.

Measuring the prompt component of the muon flux is also an interesting result for neutrino astronomy. Every charmed decay into a muon also produces a prompt muon neutrino, which are a source of background for astrophysical neutrino analyses. Although the proposed analysis method is worked out for muons and not for neutrinos, the *prompt tagging* is also possible for neutrinos. As a matter of fact, the produced MC sample for IceCube already contains tagged neutrinos. Early work suggests that these prompt neutrino spectra are consistent with MCEq as well. This analysis will be the kick-off point for a future analysis detecting the prompt component of the neutrino flux.

A Derivations

A.1 Derivation of the Lepton Flux Solutions

Consider the equation for the nucleons, which reads

$$\frac{\mathrm{d}\Phi_N(E, X)}{\mathrm{d}X} = \overbrace{\left(-\frac{1}{\lambda_N} + \frac{Z_{NN}}{\lambda_N} \right)}^{-1/\Lambda_N} \Phi_N(E, X).$$

It is trivially solved by

$$\Phi_N(E, X) = \Phi_N(E, X{=}0) e^{-X/\Lambda_N}.$$

Where the cosmic ray nucleon flux $\Phi_N(E) = \Phi_N(E, X{=}0)$ is obtained by a primary flux model from Section 2.1. The equations for the hadrons are given by

$$\frac{\mathrm{d}\Phi_H(E, X)}{\mathrm{d}X} = -\left(\overbrace{\frac{1}{\lambda_H} - \frac{Z_{HH}}{\lambda_H}}^{1/\Lambda_H} + \frac{1}{d_H} \right) \Phi_H(E, X) + \frac{Z_{NH}}{\lambda_N} \Phi_N(E, X). \tag{A.1}$$

The density dependency of d_H from Equation (2.8) has to be regarded, which introduces an implicit dependency on X.

For this, the density of earth's atmosphere at a given slant depth $\rho(X)$ must be known. The relation is obtained from the definition of the slant depth

$$X = \int_l^\infty \mathrm{d}l' \, \rho\left(h(l')\right) = \int_h^\infty \mathrm{d}h' \, \rho\left(h'\right) \frac{\mathrm{d}l(h')}{\mathrm{d}h'}.$$

The first integral is performed in terms of the length along the shower-axis and the second integral is performed in terms of the height above earth's ground h, which is the natural variable for the density. The relation $l(h)$ between the height h and the path length l is obtained via simple geometrical consideration, using the triangle shown in Figure 2.4:

$$l(h) = \sqrt{(r + h)^2 - b^2} - a = \sqrt{(r + h)^2 - r^2 \sin^2 \theta} - r \cos \theta = (r + h) \cos \theta^* - r \cos \theta.$$

The height-dependent θ^* is introduced

$$r \sin \theta = (r + h) \sin \theta^* \Leftrightarrow \theta^*(h) = \arcsin\left(\frac{r}{r + h} \sin \theta \right).$$

θ^* and θ are equal in the flat earth approximation and agree well below 60°. This results in

$$X = \int_h^\infty dh' \rho\left(h'\right) \frac{r+h'}{\sqrt{(r+h')^2 - r^2 \sin^2 \theta}} = \int_h^\infty dh' \rho\left(h'\right) \frac{1}{\cos \theta^*(h')}. \tag{A.2}$$

This integral is not analytically solvable even in the case of a simple isothermal atmosphere, with an exponential density dependency. In the flat-earth approximation $r \to \infty$, the solution is

$$X = \frac{1}{\cos \theta} \int_h^\infty dh' \rho\left(h'\right) = \frac{X_v}{\cos \theta}. \tag{A.3}$$

Restricting the solution to the simplest case of an isothermal atmosphere and making use of the ideal gas law, the vertical slant-depth X_v (zenith angle $\theta = 0$) then has the well-known exponential form of the barometric formula

$$\rho = \rho_0 e^{-h/h_0} \Rightarrow X_v = X_0 e^{-h/h_0}.$$

With typical values of $h_0 = RT/Mg = 6.5\,\text{km}$ and $X_0 = 10\,300\,\text{kg/m}^2$ [GER16, p. 121]. The wanted relation between the slant depth and the density is thus

$$\rho = -\frac{dX_v}{dh} = \frac{X_v}{h_0} = \overbrace{\frac{X_v}{X}}^{1/f(\theta,h)} \frac{X}{h_0}.$$

The *Chapman function* $f(\theta, h)$[1] is introduced, which encodes the zenith dependency and has no analytical expression, although many approximations exist [RD]. For low zenith angles and in the flat earth approximation by comparing it to Equation (A.3) it is just $f(\theta) = 1/\cos \theta$. Often, an ad-hoc approximation is obtained by ignoring the height dependency of θ^* in Equation (A.2) during integration, which results in $f(\theta, h) = 1/\cos \theta^*$.

Equation (2.8) in terms of X is now expressible by

$$d_H = \frac{EX\tau_H}{m_H c h_0 f(\theta, h)} = \frac{EX}{f(\theta, h)\epsilon_H}.$$

Where the decay constant $\epsilon_H = h_0 m_H c / \tau_H^2$ is introduced. Assuming a typical interaction depth of $X = \lambda_H$, it marks the energy at which the interaction term $1/\lambda_H$ starts dominating over the decay term $1/d_H$ for a vertical shower. The critical energy is listed for multiple hadrons in Table 2.1.

Equation (A.1) can be written simply as an inhomogenious linear differential equation of order one

$$\frac{d\Phi_H(E, X)}{dX} = -\left(\frac{1}{\Lambda_H} + \frac{\epsilon_H f(\theta, h)}{EX}\right)\Phi_H(E, X) + \frac{Z_{NH}}{\lambda_N}\Phi_N(E)e^{-X/\Lambda_N}, \tag{A.4}$$

---

[1]It is commonly called so in geo- and atmospheric physics.
[2]Expanding h_0, it is also linear to the absolute temperature of the atmosphere, which gives rise to *seasonal variations*.

which is solvable by general standard formula with [GER16, p. 124]

$$\Phi_H(E, X) = e^{-X/\Lambda_H} \frac{Z_{NH}}{\lambda_N} \Phi_N(E) \int_0^X dX' \exp\left(X'\left(\frac{1}{\Lambda_H} - \frac{1}{\Lambda_N}\right)\right) \left(\frac{X'}{X}\right)^{\epsilon_H f(\theta,h)/E}. \tag{A.5}$$

Note, that although the cascade equations were formulated using the Z-moments, that by defining them energy dependent, no assumptions other than that the X and Z dependency of Φ_i factorizes were made, which means that the Z-moments do not depend on X. It is common in literature to directly provide approximate solutions to the integral in Equation (A.5) [GER16; GMS15; Bha+15; Bug+89; TIG96; Bug+98], but it is possible to provide an exact solution by introducing the *incomplete gamma functions*

$$\Gamma(s, x) = \int_x^\infty dt \ t^{s-1} e^{-t} \quad \text{and} \quad \gamma(s, x) = \int_0^x dt \ t^{s-1} e^{-t}.$$

They are equal to the gamma function $\Gamma(s)$ at their boundaries $x = 0$ (for $\Gamma(s, x)$) and $x = \infty$ (for $\gamma(s, x)$).

With them, the exact solution to Equation (A.5) is written as

$$\Phi_H(E, X) = e^{-X/\Lambda_H} \frac{Z_{NH}}{\lambda_N} \Phi_N(E) \frac{X \cdot \overbrace{\left[\Gamma\left(\frac{\epsilon_H f}{E} + 1\right) - \Gamma\left(\frac{\epsilon_H f}{E} + 1, \frac{X}{\Lambda_N} - \frac{X}{\Lambda_H}\right)\right]}^{\gamma\left(\frac{\epsilon_H f}{E} + 1, \frac{X}{\Lambda_N} - \frac{X}{\Lambda_H}\right)}}{\left(\frac{X}{\Lambda_N} - \frac{X}{\Lambda_H}\right)^{1 + \epsilon_H f(\theta,h)/E}}. \tag{A.6}$$

In reality, though, this is nothing but a reformulation, since no analytical form of the gamma functions exist. The form can be useful nonetheless, since the gamma functions are implemented in many numerical libraries and are well studied objects. If nothing else, it shows where the exactness of the solution breaks down exactly: Equation (2.15) can not be written as a factorization of energy and slant-depth functions, which in turn means that the Z moments are X dependent in the solution and this was ignored when solving the linear differential equation eq. (A.4). The dependency is only expected to be slight, so the provided solutions are expected to be almost exact. Forms of the high- and low energy limit are now derived, which are important to understand the *prompt* and *conventional* parts of the lepton spectra.

In the high energy limit $E \gg \epsilon_H f(\theta, h)$ [3], the argument of the gamma function is $s = 1$ and they boil down to a simple exponential integration with the solution

$$\Phi_H^{\text{high}}(E, X) = \Phi_N(E) \frac{Z_{NH}}{1 - Z_{NN}} \frac{\Lambda_H}{\Lambda_H - \Lambda_N} \left(e^{-X/\Lambda_H} - e^{-X/\Lambda_N}\right). \tag{A.7}$$

---

[3]Since the zenith dependency is complicated and only varies a bit more than a factor of 10, usually $E \gg \epsilon_H$ is enough to specify.

In the low energy limit $E \ll \epsilon_H f(\theta, h)$ the first argument of the gamma function is very large, hence the power law part in the integral appendix A.1 favors higher values of t. Therefore, the exponential part in $\gamma(s, x)$ is taken as constant towards the upper end x, which reduces γ to a power law integration. This provides the solution

$$\Phi_H^{\text{low}}(E, X) = \Phi_N(E) e^{-X/\Lambda_N} \frac{Z_{NH}}{\lambda_N} \frac{X}{1 + \frac{\epsilon_{Hf}}{E}} \approx \Phi_N(E) e^{-X/\Lambda_N} \frac{Z_{NH}}{\lambda_N} \overbrace{\frac{EX}{\epsilon_H f(\theta, h)}}^{d_H}. \tag{A.8}$$

In the last step, lepton fluxes generated by the decaying hadrons are calculated, and only the source term is included, so the cascade equations eq. (2.13) read

$$\frac{d\Phi_L}{dX} = \sum_H \frac{Z_{HL}^d}{d_H} \Phi_H(E, X).$$

Since there is no Φ_L dependency on the right hand side, the equations can just be integrated. The integral of the gamma functions does not have any analytical expression, so the low energy expression eq. (A.8) and the high energy expression eq. (A.7) for each hadron are integrated separately and the low energy limit is obtained as

$$\Phi_L^{\text{low}} = \Phi_N(E) \frac{Z_{NH} Z_{HL}^d}{1 - Z_{NN}} \left(1 - e^{-X/\Lambda_H}\right) \tag{A.9}$$

and the high energy limit as

$$\Phi_L^{\text{high}} = \Phi_N(E) \frac{Z_{NH} Z_{HL}^d}{1 - Z_{NN}} \frac{\epsilon_H f(\theta, h)}{E} \frac{\Lambda_H}{\Lambda_H - \Lambda_N} \int_0^X dX' \frac{1}{X'} \left(e^{-X'/\Lambda_H} - e^{-X'/\Lambda_N}\right). \tag{A.10}$$

In literature the expressions for high X are usually given since $X \gg \Lambda_i$ is a good approximation. For the case of Equation (A.9) the result is trivially

$$\Phi_L^{\text{low}} = \Phi_N(E) \frac{Z_{NH} Z_{HL}^d}{1 - Z_{NN}}. \tag{A.11}$$

The deviation from the exact solution for $E = 100 \, \text{GeV}$ and $H = \pi$ and at typical vertical X at sealevel from [GER16] is only $0.13 \, \%$. But for Equation (A.10) the limit is not that trivial and a proper derivation is usually skipped in literature but can be found in Appendix A.2, where also an expression for the exact solution is provided[4]. The resulting high X expression is

$$\Phi_L^{\text{high}} = \Phi_N(E) \frac{Z_{NH} Z_{HL}^d}{1 - Z_{NN}} \frac{\epsilon_H f(\theta, h)}{E} \frac{\Lambda_H}{\Lambda_H - \Lambda_N} \ln \Lambda_H / \Lambda_N. \tag{A.12}$$

The deviation to the exact expression here is typically $0.06 \, \%$.

---

[4]The author could not find the exact solution in literature for comparison.

A.2 Derivation of the High Density Integral

To derive a high-X expression for the integral

$$I = \int_0^X dX' \frac{1}{X'} \left(e^{-X'/\Lambda_H} - e^{-X'/\Lambda_N} \right),$$

care has to be taken, since the integrant is not defined at $X' = 0$, which makes the evaluation of the integral non-trivial. The expression needs to be understood as a limit and can then be rewritten as

$$I = \lim_{\varepsilon \to 0} \int_\varepsilon^X dX' \frac{1}{X'} \left(e^{-X'/\Lambda_H} - e^{-X'/\Lambda_N} \right) = \lim_{\varepsilon \to 0} \left(\int_\varepsilon^X dX' \frac{1}{X'} e^{-X'/\Lambda_H} - \int_\varepsilon^X dX' \frac{1}{X'} e^{-X'/\Lambda_N} \right).$$

The splitting of the integral is only possible when leaving the limit outside, since limits (from the definition of the integral) would be swapped otherwise. To solve that, the new variable $y = X'/\Lambda_i$ is introduced

$$I = \lim_{\varepsilon \to 0} \left(\int_{\varepsilon/\Lambda_H}^{X/\Lambda_H} dy \frac{1}{y} e^{-y} - \int_{\varepsilon/\Lambda_N}^{X/\Lambda_N} dy \frac{1}{y} e^{-y} \right).$$

At this point it is worth mentioning that each integral does not converge on its own, and the combined expression one step earlier has no analytical form and on top of that: convergence is highly unobvious. The non-elementary *exponential integral* function E_1 is introduced [ASR88, p. 229], which is defined as

$$E_1(x) := \int_x^\infty dt \frac{e^{-t}}{t} \quad \text{for } x > 0$$

$$= -\gamma - \ln x - \sum_{n=1}^\infty \frac{(-x)^n}{n n!} = \Gamma(0, x).$$

Where γ is the Euler–Mascheroni constant and $\Gamma(s, x)$ is the incomplete gamma function, which was introduced earlier in Section 2.3. The series expansion can be easily derived by writing the exponential as its Taylor-Series. With an exact solution to I can be given

$$I = E_1(X/\Lambda_N) - E_1(X/\Lambda_H) + \lim_{\varepsilon \to 0} \left(E_1(\varepsilon/\Lambda_H) - E_1(\varepsilon/\Lambda_N) \right) = E_1(X/\Lambda_N) - E_1(X/\Lambda_H) + \ln\left(\frac{\Lambda_H}{\Lambda_N} \right).$$

Where the form with the logarithm is obtained by using the series expansion without any terms from the sum. This solution is exact and the high energy solution for the lepton flux is therefore

$$\Phi_L^{\text{high}} = \Phi_N(E) \frac{Z_{NH} Z_{HL}^d}{1 - Z_{NN}} \frac{\epsilon_H f(\theta, h)}{E} \frac{\Lambda_h}{\Lambda_h - \Lambda_N} \left(E_1(X/\Lambda_N) - E_1(X/\Lambda_H) + \ln\left(\frac{\Lambda_H}{\Lambda_N} \right) \right). \tag{A.13}$$

By the definition of the E_1 function it is obvious that it converges to 0 for high x values, since the integration interval goes to 0. The known expression for high X is obtained

$$\Phi_L^{\text{high}} = \Phi_N(E) \frac{Z_{NH} Z_{HL}^d}{1 - Z_{NN}} \frac{\epsilon_H f(\theta, h)}{E} \frac{\Lambda_h}{\Lambda_h - \Lambda_N} \ln\left(\frac{\Lambda_H}{\Lambda_N}\right). \tag{A.14}$$

B Tagging

B.1 CORSIKA7 Steering Card

```
RUNNR     {run_idx}                   run number
EVTNR     {first_event_idx}           number of first shower event
NSHOW     {n_show}                    number of showers to generate
PRMPAR    {primary}                   particle type of prim. particle
ESLOPE    -1                          slope of primary energy spectrum
ERANGE    {emin}  {emax}              energy range of primary particle
THETAP    0.   0.                     range of zenith angle (degree)
PHIP      -180.  180.                 range of azimuth angle (degree)
SEED      {seed_1}   0   0            seed for 1. random sequence
SEED      {seed_2}   0   0            seed for 2. random sequence
OBSLEV    110.E2                      observation level (in cm)
FIXCHI    0.                          starting altitude (g/cm**2)
MAGNET    16.811   -51.890            magnetic field at south pole
HADFLG    0  0  0  0  0  2            flags hadr.interact.&fragment.
ECUTS     1.E5  1.E5  1.E20  1.E20    energy cuts for particles
MUADDI    T                           additional info for muons
MUMULT    T                           muon multiple scattering angle
ELMFLG    T    T                      em. interaction flags (NKG,EGS)
STEPFC    1.0                         mult. scattering step length fact.
RADNKG    200.E2                      outer radius NKG lat.dens.distr.
LONGI     F  10.   F   F              longit.distr. & step & fit & out
MAXPRT    1                           max. number of printed events
DIRECT    {dir}                       output directory
DYNSTACK  10000                       size DYNSTACK
DYNSTACK_P 1 1                        Parameter DYNSTACK (prompt norm)
USER      you                         user
DEBUG     F   6   F   1000000         debug flag and log.unit for out
EXIT                                  terminates input
```

Listing 1: CORSIKA7 card for the test dataset used in chapter 3. The templates marked with {...} are replaced accordingly.

B.2 EHISTORY **Output**

Some output of CORSIKA7 with the extended history (EHISTORY) option is not fully understood. The fraction of muons with unreasonable values in specific variables is shown from Figure B.1 to Figure B.6. Everything is provided as a weighted flux-fraction and a unweighted muon-number fraction.
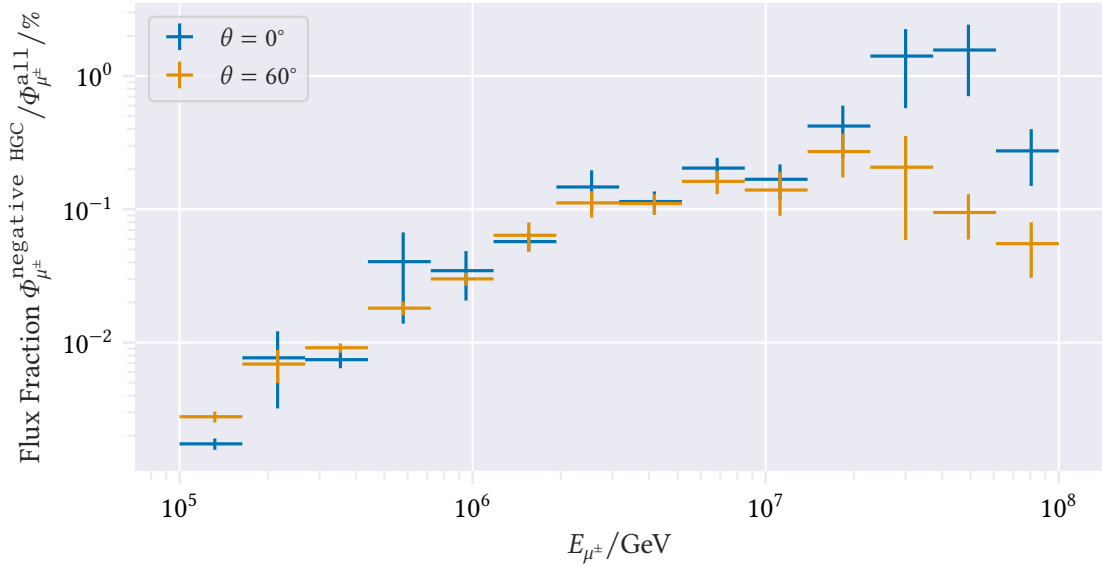
Figure B.1: This shows the Flux fraction of negative hadron generation counter (HGC) weighted with Global Spline Fit (GSF).
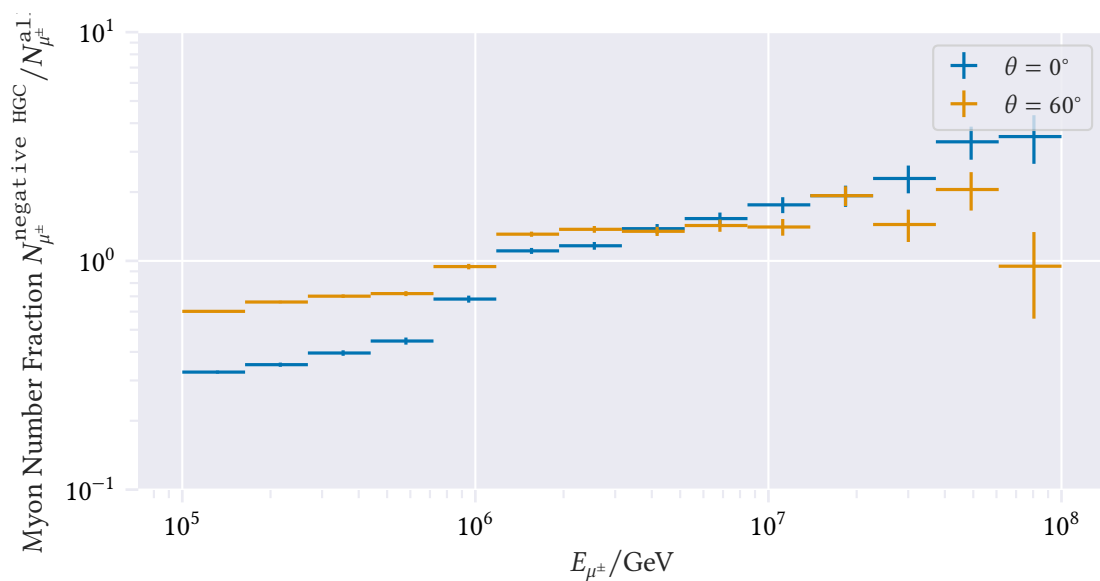
Figure B.2: Number of muon fraction of negative HGC.
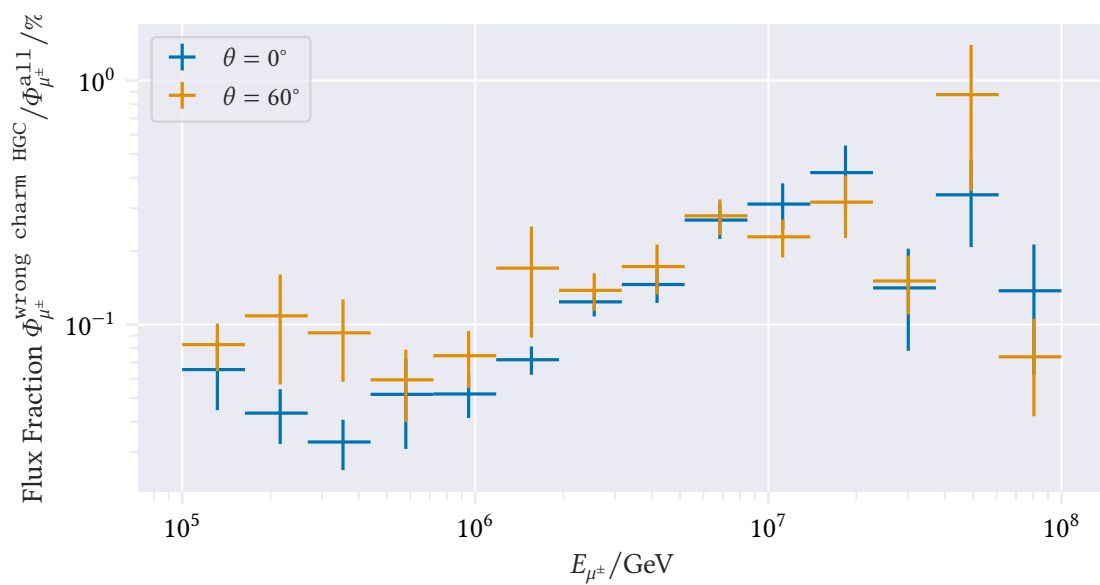
Figure B.3: Energy-dependent flux-fraction of muons with a HGC of less than 30, but with charmed parent particles weighted with GSF.
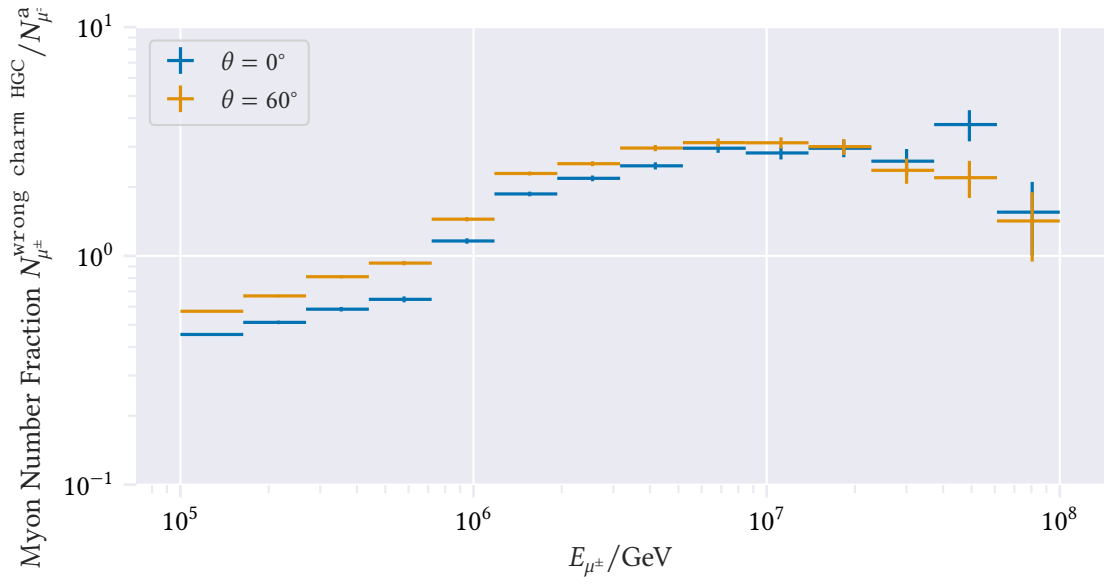
Figure B.4: Energy-dependent number of muons fraction with a HGC of less than 30, but with charmed parent particles.
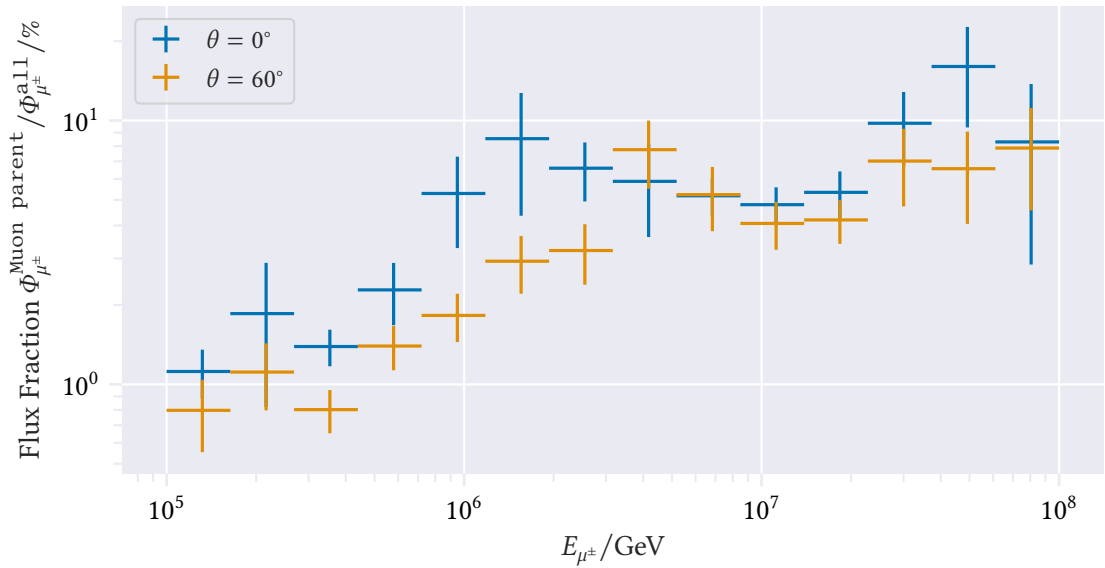
Figure B.5: Energy-dependent flux fraction of muons with muons as parent particles weighted with GSF.
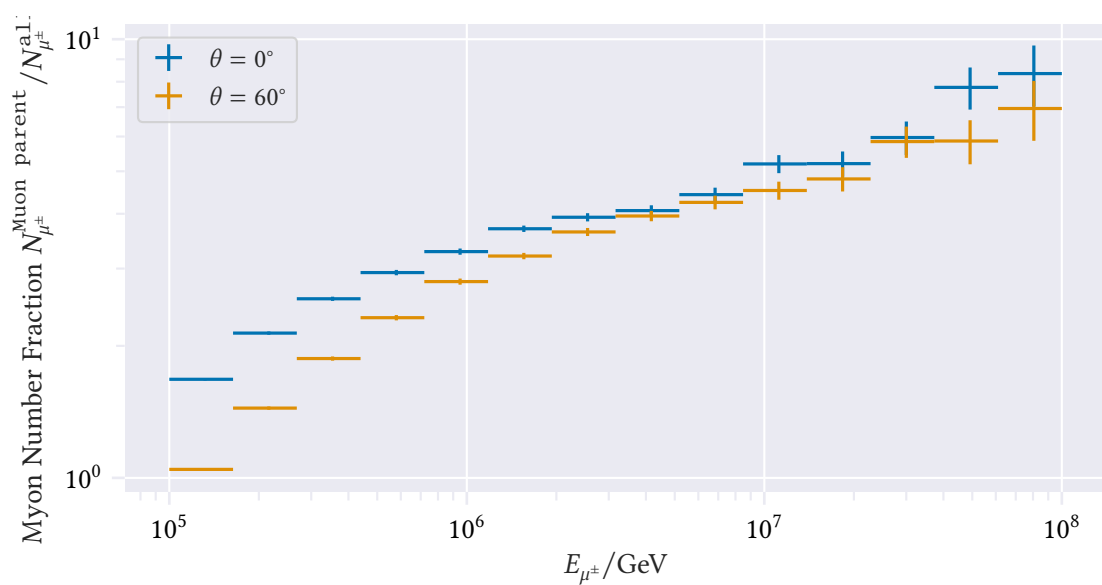
Figure B.6: Energy-dependent fraction of muons with muons as parent particles.

C IceCube Analysis

C.1 Expected Event Rates and Filters

To calculate expected event rates, the weighting described in Chapter 3 has to be modified. The weighting of the IceCube simulation starts with the weights from Equation (3.2), but *event rates* $R = dN/dt$ are now of interest instead of fluxes. The weights $w_\Phi(E)$ from Equation (3.2) which result in fluxes $\Phi = dN/dA\,d\Omega\,dE\,dt$ need to be multiplied [1] by the area and the solid angle of the detector, which are zenith-dependent[2] $A(\theta)$, which results in event rates weights

$$w_R = w_\Phi \int d\Omega\, A(\theta) = w_\Phi 2\pi \int_{\theta_{\min}}^{\theta_{\max}} d\theta\, A(\theta)\sin\theta = w_\Phi 2\pi \int_{\cos\theta_{\max}}^{\cos\theta_{\min}} d\cos\theta\, A(\cos\theta),$$

where the last representation is chosen since the detector area in dependence of the zenith angle is parameterized as $A = \sum_i A_i \cos(\theta - \theta_i)$ for many detector geometries, like union of many planar surfaces or a cylinder. The integral is called the "area sum". These weights must be applied so that n in Equation (3.2) refers to the number of *generated* events. Not all generated events N_{gen} trigger the detector or pass the filters, this number is generally smaller $N_{\text{passed}} < N_{\text{gen}}$. To easily estimate the rate of expected events for a certain differential energy flux, the effective area

$$A_{\text{eff}}(E, \theta) = \overbrace{\frac{dN_{\text{passed}}}{dt\,dE\,d\Omega}}^{R} \Bigg/ \overbrace{\frac{dN_{\text{generated}}}{dt\,dE\,dA\,d\Omega}}^{\Phi}$$

is introduced. By this definition, it is the area a theoretical flux needs to be multiplied with, to get the expected event rate [GER16]. With Monte Carlo (MC) simulations the effective area can easily be calculated (possibly restricted to certain energy and zenith bins) by summing the rate weights for the passed events and dividing by the sum of flux-weights of generated events

$$A_{\text{eff}}(E, \theta) = \frac{\sum_{\text{passed}} w_R}{\sum_{\text{generated}} w_\Phi} \propto \frac{N_{\text{passed}}(E)}{N_{\text{generated}}(E)} \int A(\theta)\, d\Omega.$$

---

[1]This can be motivated as follows: With dividing the primary flux by the (extended) PDF of the generation probability in Equation (3.2), the distribution in energy is accounted for. To also include the distribution in area and solid angle, which are approximately uniformly distributed, since Cosmic Ray (CR) are isotropic, dividing the PDF there is the same as multiplying by the normalization constant, which is the integral given in the formula.

[2]For an approximately spherical symmetric detector like IceCube , otherwise also an azimuth dependency exists.
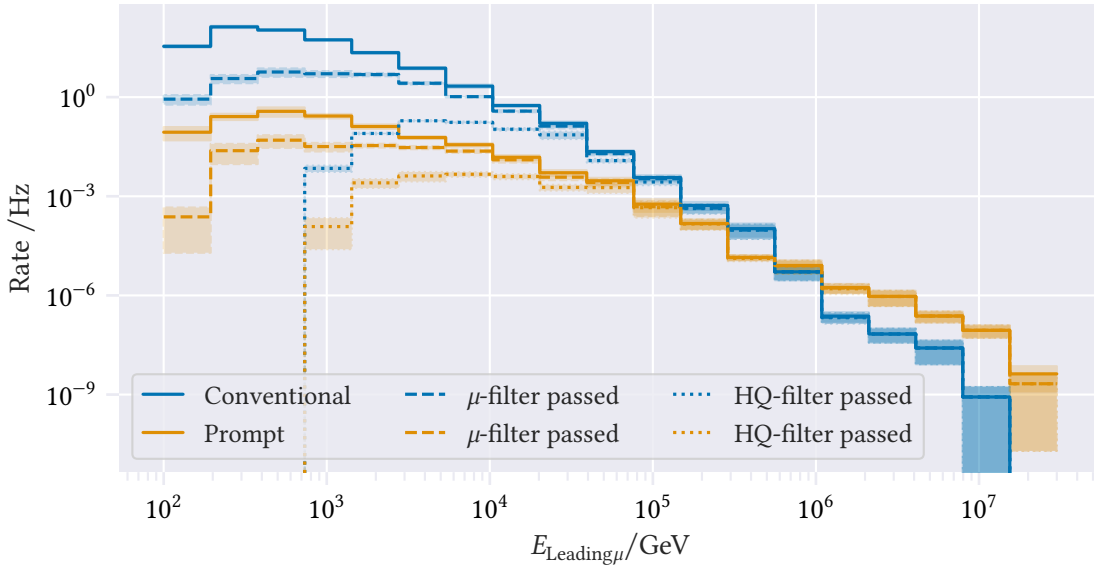
Figure C.1: The event rates for prompt and conventional events for the passed muon and HQ-filter in dependence of the leading muon energy. The events are weighted with the GSF primary model.

The expected event rates in dependence of the leading muon energy are shown in Figure C.1, where they are split up into prompt (orange) and conventional (blue) events. Additionally, the event rates with the applied "muon-filter" and "HQ-filter" are shown. The two filters are standard filters in the IceCube software for selection of muon or high charge events. The muon filter selects events based on the charge and the zenith reconstruction. It divides the events into three reconstructed $\cos\theta$ intervals $[-1, 0.2)$, $[0.2, 0.5)$ and $[0.5, 1]$. In the first interval (below the horizon to slightly above), the likelihood of the fit is required to be below a certain threshold. The integrated charge in the other two zenith regions is required to be above a certain threshold, which increases linearly in each of the regions with a continuous transition. With simpler words: the more upgoing an event is, the more charge it has to have, and events below the horizon only require to have a fit with a likelihood below a certain threshold. The HQ filter is simpler and only requires the total deposited charge to exceed 1000 pe. For a first proof-of-concept data selection, the muon filter seems to have the right trade-off between reducing the data rate and keeping almost all prompt events in the interesting transition region above 10 TeV. From here on, every event shown passed the muon filter.

The unweighted composition of the primaries in the MC dataset is shown in Figure C.2. The expected event rate of conventional muon events without the muon filter is 365.21 Hz and the event rate of prompt muons is 4.23 Hz . With the applied muon filter, the event rate is 24.40 Hz for conventional muons and 0.21 Hz for prompt ones.

A quantity to estimate the size of the generated MC dataset in terms of "how long would it take the detector to take data with a similar statistics?" is the *effective livetime*. The effective
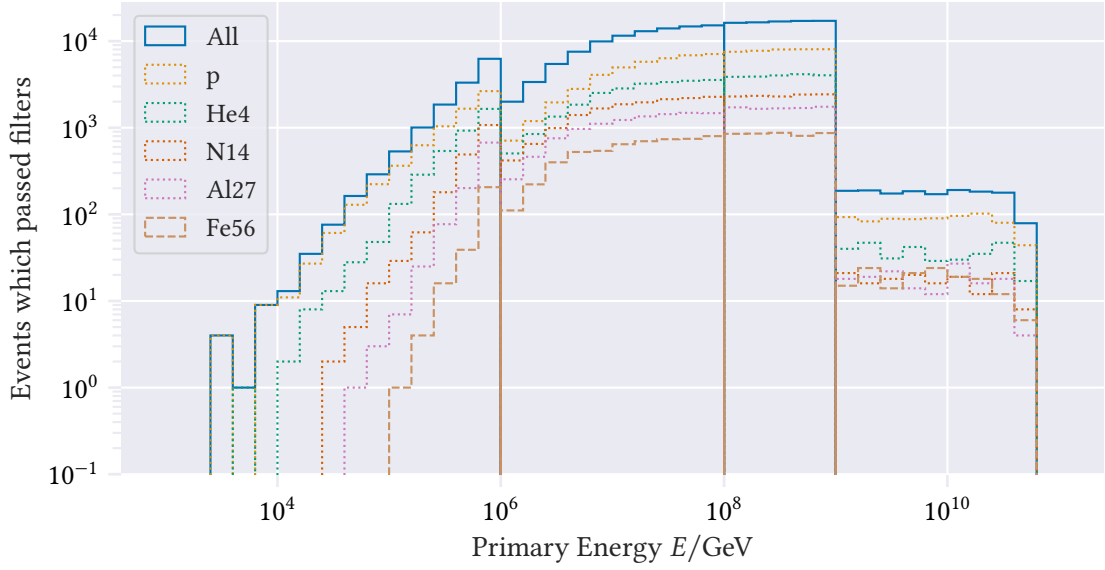
Figure C.2: The contribution from different primary particles to the MC dataset in the IceCube simulation which triggered the detector and passed the muon filter.

livetime[3] T_{eff} of a MC sample refers to the time the detector needs to take data to collect a dataset with the same average relative uncertainty. For an unweighted sample with N events, which are assumed to be Poisson distributed, the uncertainty is $\sqrt{N}$. For a weighted sample the uncertainty in the event rate R is, as described in Section 3.2, $\Delta R = \sqrt{\sum_i w_i^2}$. With that, the effective livetime is derived:

$$\frac{\sqrt{N}}{N} = \frac{\sqrt{RT}}{RT} \overset{!}{=} \frac{\Delta R}{R} \Leftrightarrow T_{eff} = \frac{R}{\Delta R^2} = \frac{\sum_i w_i}{\sum_i w_i^2}.$$

The effective lifetime is shown in Figure C.3 for the used dataset after passed muon filters, in dependence of an energy cut to the leading muon energy. The produced dataset heavily favors, as wanted and expected, high energy events. Above 10 PeV the statistics is equivalent to more than 10 years of data. While in the transition region of prompt above 100 TeV, the MC data is only equivalent to a few hours of data-taking. The effect of different primary models is depicted, although they only differ for very high energies.

The difference of the four state-of-the-art primary models is shown in Figure C.4. To highlight the distinctness of the four models, Gaisser's H3a model is chosen as a baseline model and the ratio of the expected event rate compared to H3a is shown energy-dependently for prompt and conventional events. GSF produces the highest amount of prompt muons (except for the last energy bin). And the models are in agreement in the low energy region.

---

[3]Note that "livetime" refers to the time in which the detector is "live", not the time of the detector's "life".
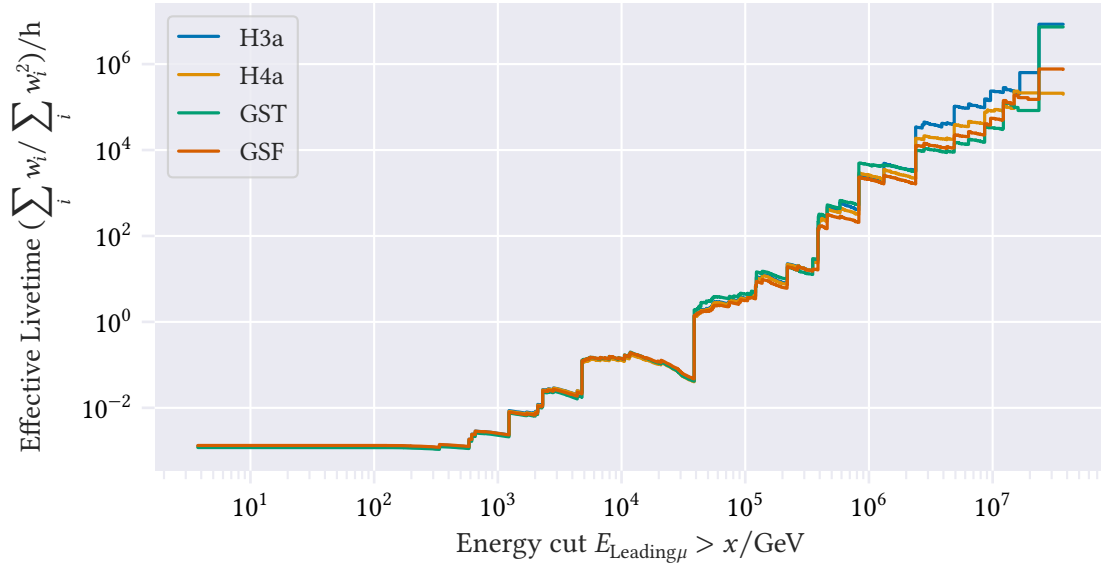
Figure C.3: The effective livetime of the MC dataset, after passed muon filters in dependence of the chosen energy cut on the true leading muon energy. It can be seen that the simulation focuses towards higher energies.
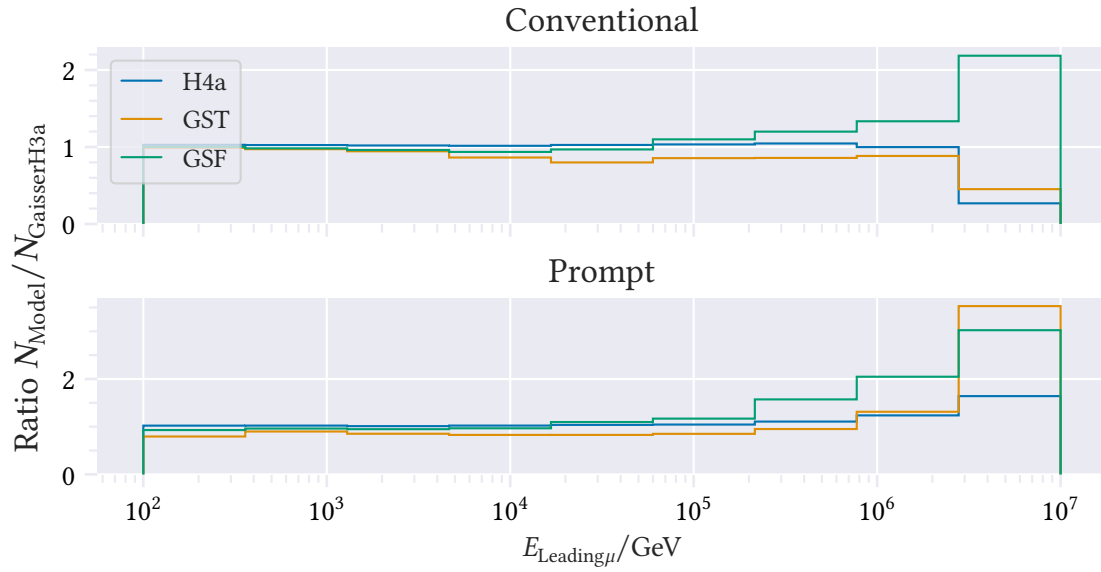
Figure C.4: The difference between the event rates for four different primary models is depicted. With conventional events shown in the top panel and prompt events shown in the bottom panel. The *y*-axis shows the ratio of the model to the Gaisser H3a model.
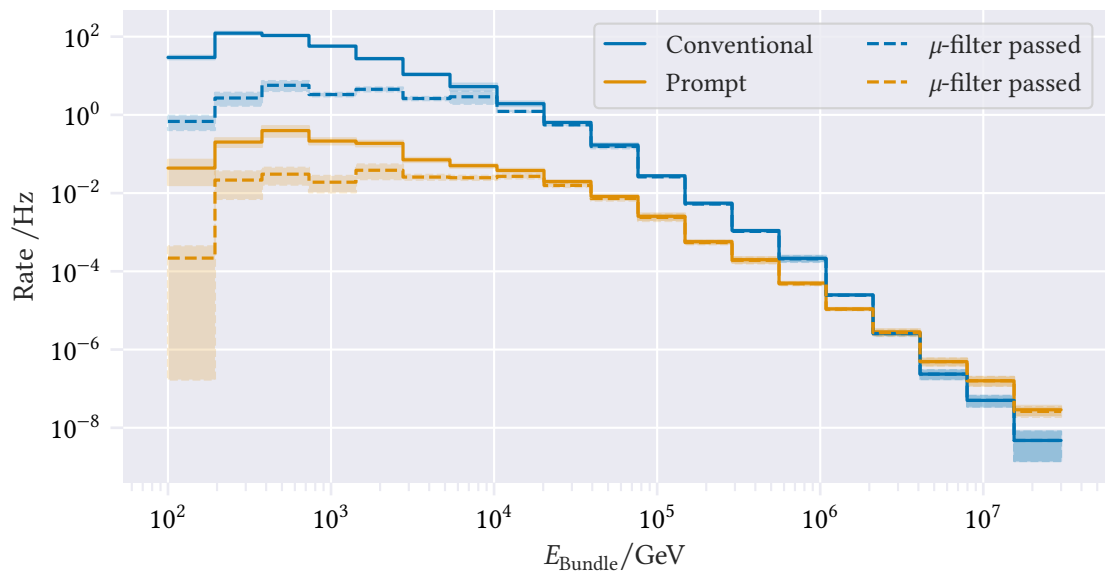
Figure C.5: The bundle-energy dependent event rate for conventional and prompt events, and how many passed the muon filter. The MC sample is weighted using the GSF model.

C.2 Data-MC Agreement

A precursor IceCube analysis [IC16], was able to reject the hypothesis of no prompt muons with a significance of 3.46σ [IC16]. The authors observed a zenith-dependent data/MC mismatch, stemming from an unknown systematic error, shown in Figure C.6a. Since their result depends on a fit in two zenith bins, authors report a significance of more than 9σ if the angular correction were not needed. Since the MC simulation in Reference [IC16] used the SIBYLL2.1 hadronic interaction model [Ahn+09], there is the hope that newer MC simulations describe the muon distribution better and may lower some of the disagreements observed between data and MC. The angular distribution of muons for example differs greatly between SIBYLL2.1 and SIBYLL2.3c, as shown for the energy of 10 PeV in Figure C.6b. This effect is energy-dependent and it is currently unclear if that is the full solution to the zenith dependent mismatch.
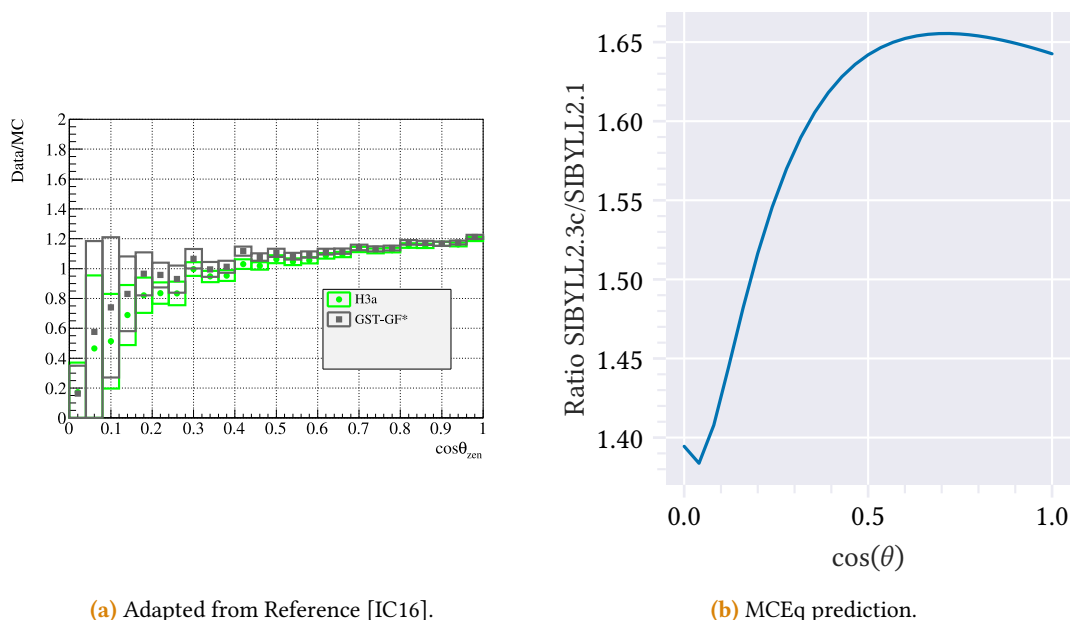
(a) Adapted from Reference [IC16].

(b) MCEq prediction.

Figure C.6: Figure C.6a shows the zenith dependent data/MC ratio reported by Reference [IC16]. While the convergence to a value of 1.2 on the right is expected due to the muon puzzle, the zenith dependence of the mismatch introduces a systematic uncertainty in analyses. Figure C.6b depicts the zenith dependent ratio of the muon flux from MCEq produced with the hadronic interaction model SIBYLL2.3c and SIBYLL2.1 at a muon energy of 10 PeV.

To affirm the correct application of weights to the MC simulation in IceCube, a very small burn dataset of 8 h (on 2020−06−04) is loaded. Most of the measured events in one run are low energy atmospheric muon events and this MC set has very low statistics for that region. To bring the uncertainty for the MC simulation down to a comparable level to the eight hours of data, the effective livetime is investigated depending on the reconstructed energy compared to the actual

livetime in the dataset in Figure C.7. In this, besides the effective livetime, also the number of surviving events after a chosen cut on the reconstructed leading energy are shown. To have the same average uncertainty, a cut in the region where the effective livetime equals eight hours needs to be chosen, which is somewhere above 10^5 GeV. But with this cut only a little more than 100 events survive, so even if the uncertainty is overall on a comparable level than, this would mean that a binning with very few bins has to be chosen. Thus, a cut one order of magnitude lower at 10 TeV is chosen, where the MC uncertainty equals to less than one hour, but a few 10000 events are left.
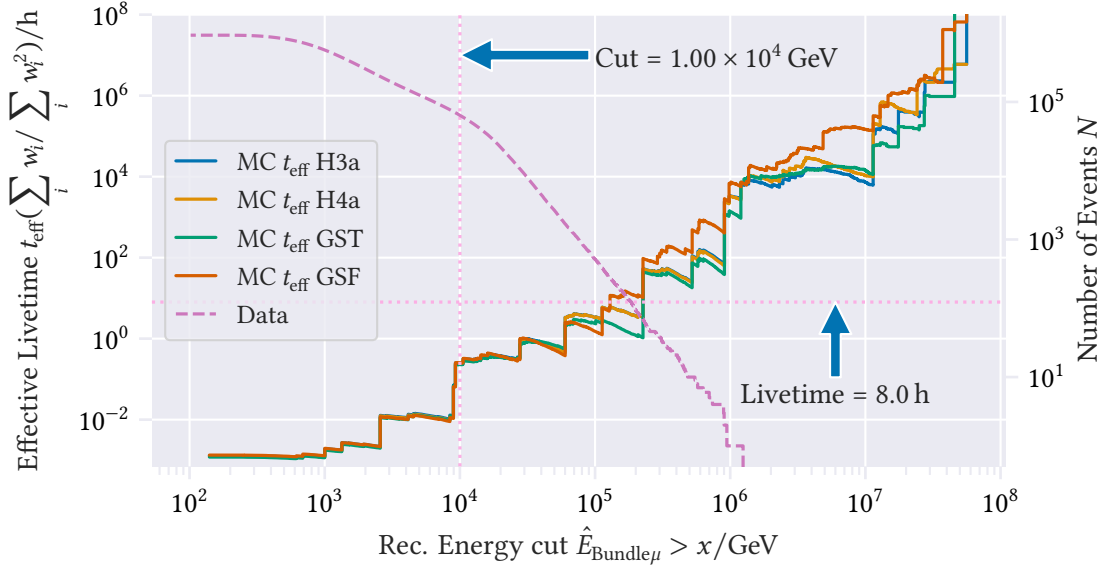
Figure C.7: The effective livetime of the MC dataset and the number of events in the 8 hour data sample as a function of the chosen energy cut on the reconstructed muon bundle energy. To make the error bars of the data and MC sets comparable, a cut of approximately 2×10^5 GeV needs to be chosen. In that case only more than one hundred data events remain, so a cut of 1.00×10^4 GeV is chosen, so the effective lifetime is roughly one order of magnitude below the livetime of the dataset and thus the error bars are approximately 3 times larger on average for the MC set, which is still on a comparable level.

In Figure C.8 four different distributions for various variables, which are not reconstruction related are compared in data and MC for Global Fit GST (GST) and GSF weighting, for the full dataset without an energy cut. The error bars for the experimental data are way smaller than for the MC dataset. Consistency between data and MC, in the tolerance of the uncertainties, although on average the data counts seem to be higher than the MC counts. This is consistent with the muon puzzle.

Looking at the same variables with the 10 TeV cut applied in Figure C.9, the overall agreement is larger. This can have two possible explanations. Either the observed offset in Figure C.8 are a statistical fluctuation due to a few low energy MC events with high weights. The other, more
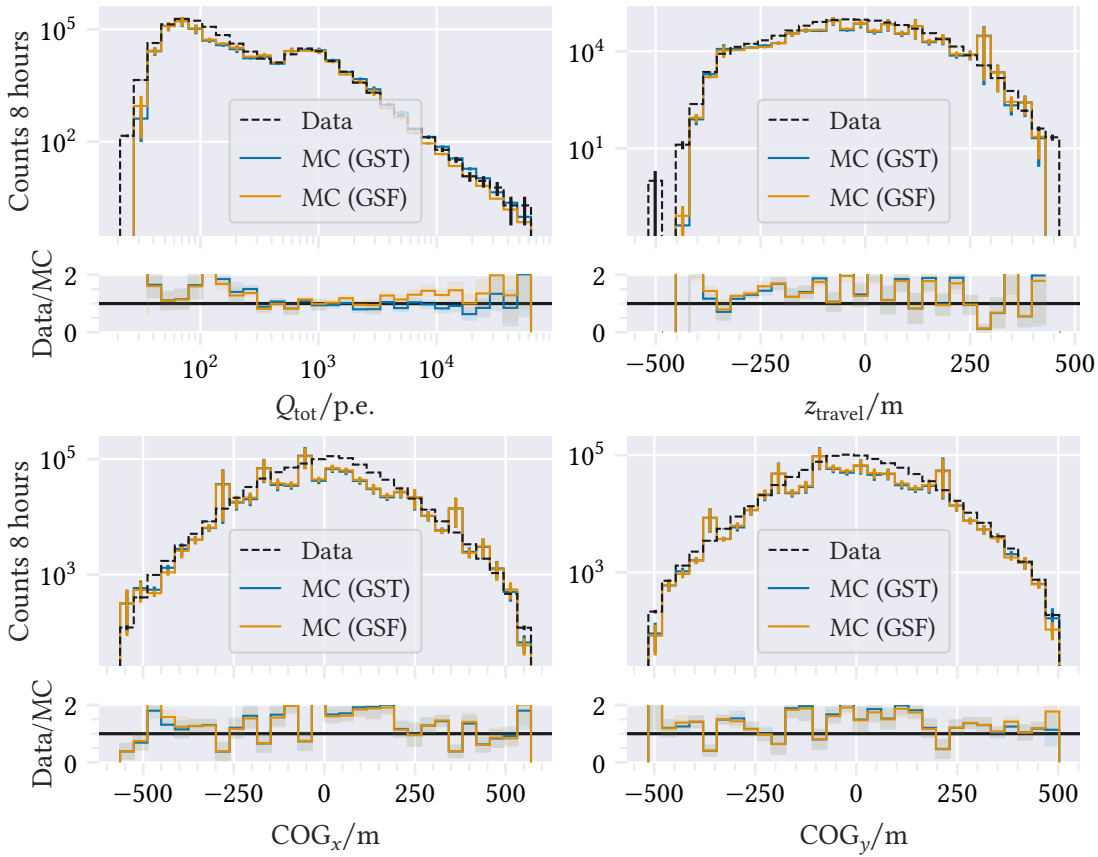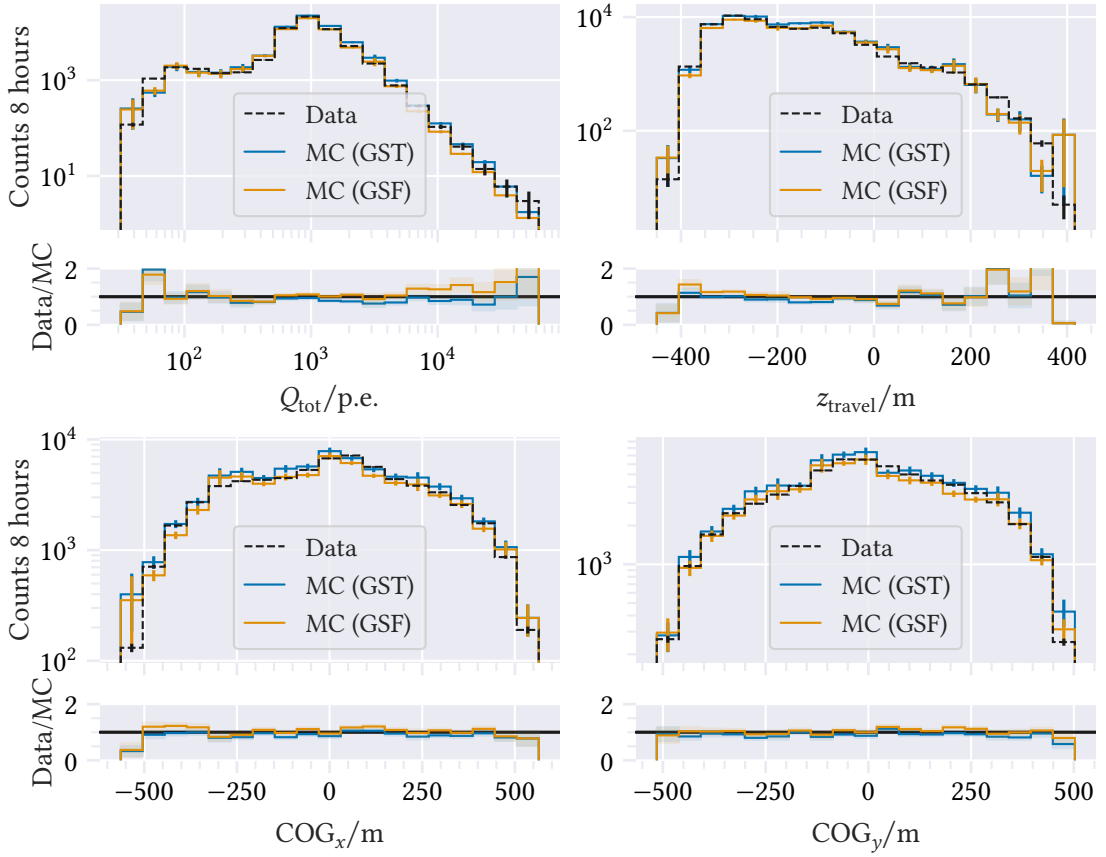
Figure C.8: The distribution of four different variables to assess Data/MC agreement on the burn-sample is displayed. Here, no cut on the bundle energy is applied. Q_{tot} is the total charge deposited in the detector, z_{travel} is the distance on the z-axis between the average position of all Digital Optical Module (DOM)s hit and the first quarter in time of DOMs hit, while the COG variables refer to the charge-weighted center of gravity of an event.

likely, explanation is that the MC simulation describes the high energy events better than the low energy events.

While the data/MC agreement on the summary statistics asserted, that the weighting is producing the correct expected results, the data/MC agreement on reconstructed variables are of special interest, since these are the variables which will be used in the analysis. Also, their calculation is more complicated and especially for the chosen deep learning based reconstruction, it is not possible to easily assess which input features produce which outcome. The bundle energy seems to be reconstructed with approximately the same distribution on MC and experimental data in Figure C.10. There the GSF model seems to produce visibly better agreement for high energies than the GST model. As expected, the leading muon energy is harder to reconstruct, and a large disagreement in the high energy region for this variable in Figure C.11 is seen.

As explained at the beginning of this section, especially the zenith dependent data/MC mismatch

Figure C.9: The distribution of four different variables to assess Data/MC agreement on the burn-sample is shown. Here, a cut on the bundle energy of 1.00×10^4 GeV is applied, which allows the MC set to have error bars on the same order of magnitude. Q_{tot} is the total charge deposited in the detector, z_{travel} is the distance on the z-axis between the average position of all DOMs hit and the first quarter in time of DOMs hit, while the COG variables refer to the charge-weighted center of gravity of an event.

is of interest. Figure C.12 shows the zenith distribution for the whole dataset. It is not unlike Figure C.6a, where a constant offset for low zenith values (high $\cos\theta$) is seen, and the offset shifts towards the horizon. When applying the energy cut at 10 TeV, the agreement gets better. This is shown in Figure C.13.
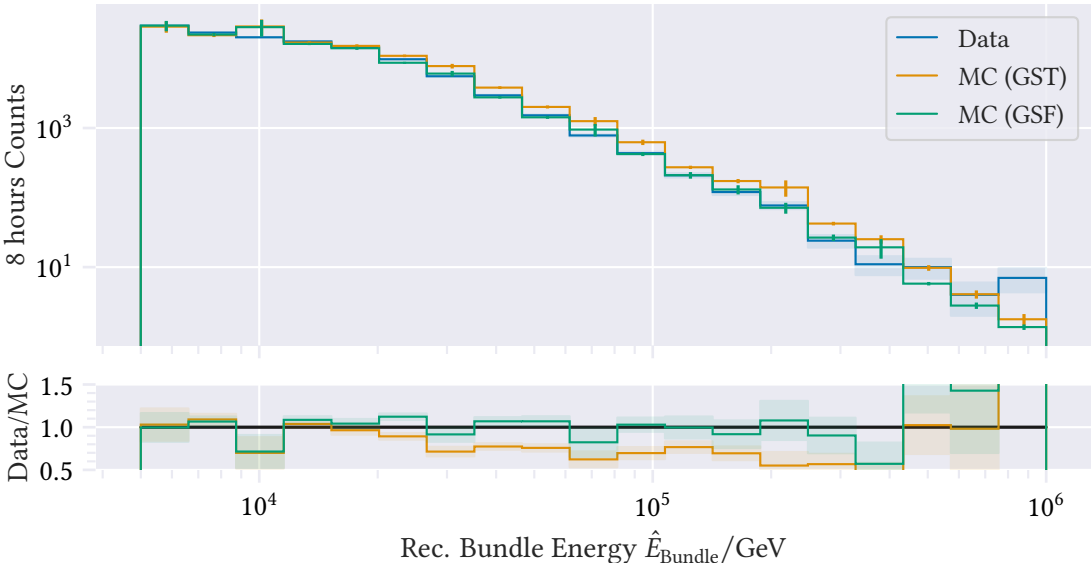
Figure C.10: Muon bundle energy dependent Data/MC comparison on the burn sample.
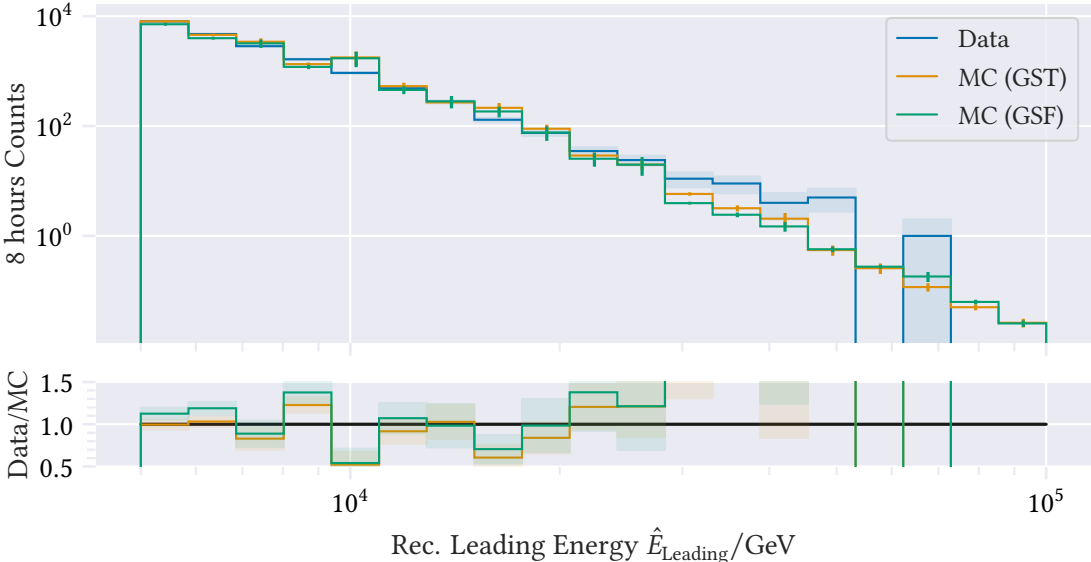
Figure C.11: Leading muon energy dependent Data/MC comparison on the burn sample.
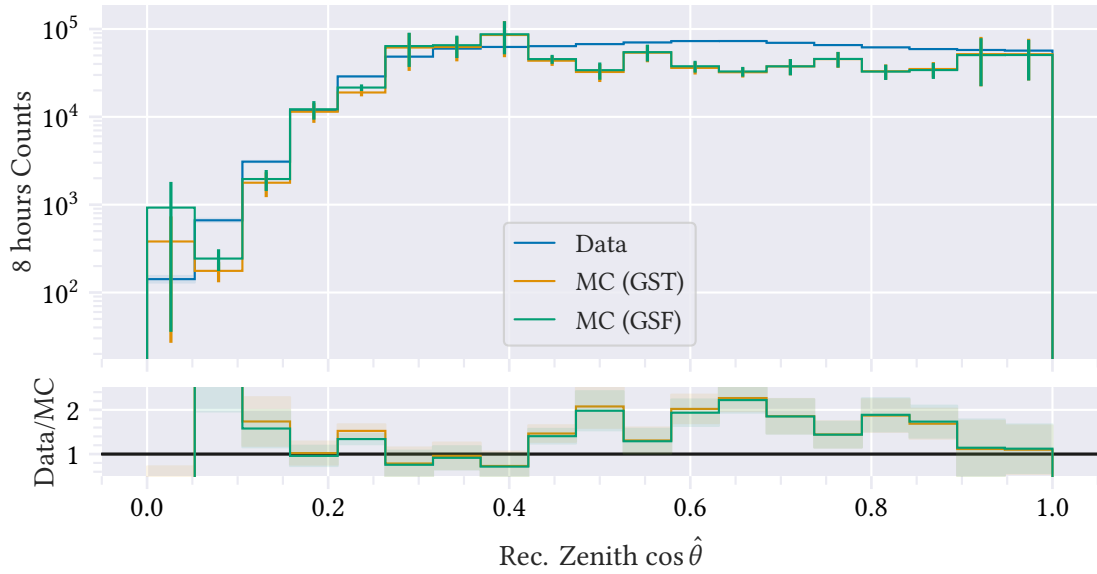
Figure C.12: The zenith distribution of the burn data and MC sample is binned. The lower panel shows the ratio of data and MC. Here no energy cut is applied, so the MC set has low statistics in the low energy region compared to the data. The burn sample corresponds to one run of data-taking, which is approximately 8 hours.
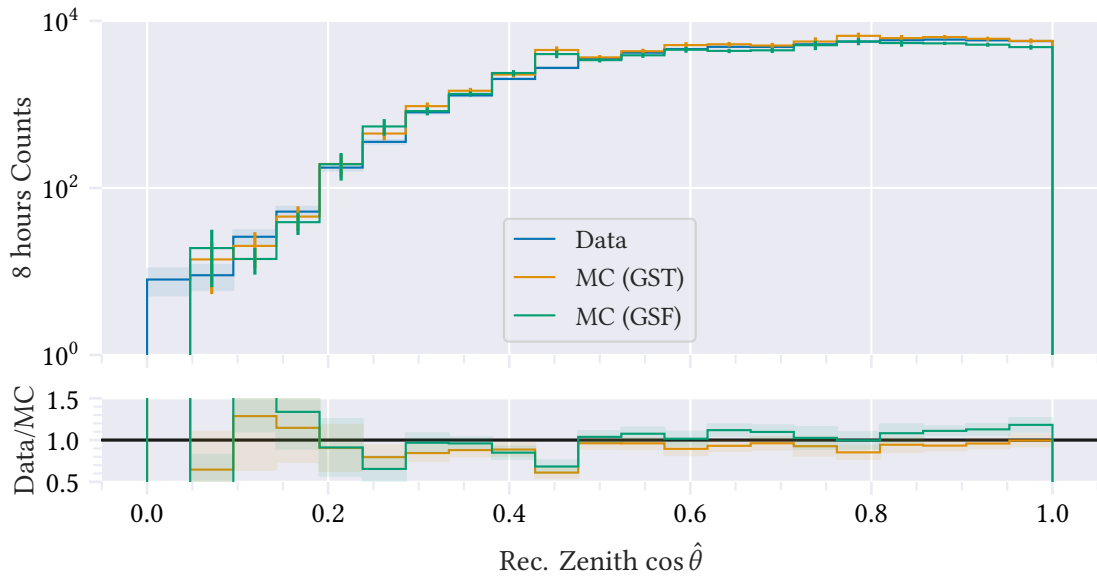
Figure C.13: Data/MC comparison of the zenith distribution after applying an energy cut of 1.00×10^4 GeV is depicted. The burn sample was recorded in 8 hours.

C.3 Sampling

The sampling of a toy MC set with different injected prompt normalizations is shown in Figure C.14.
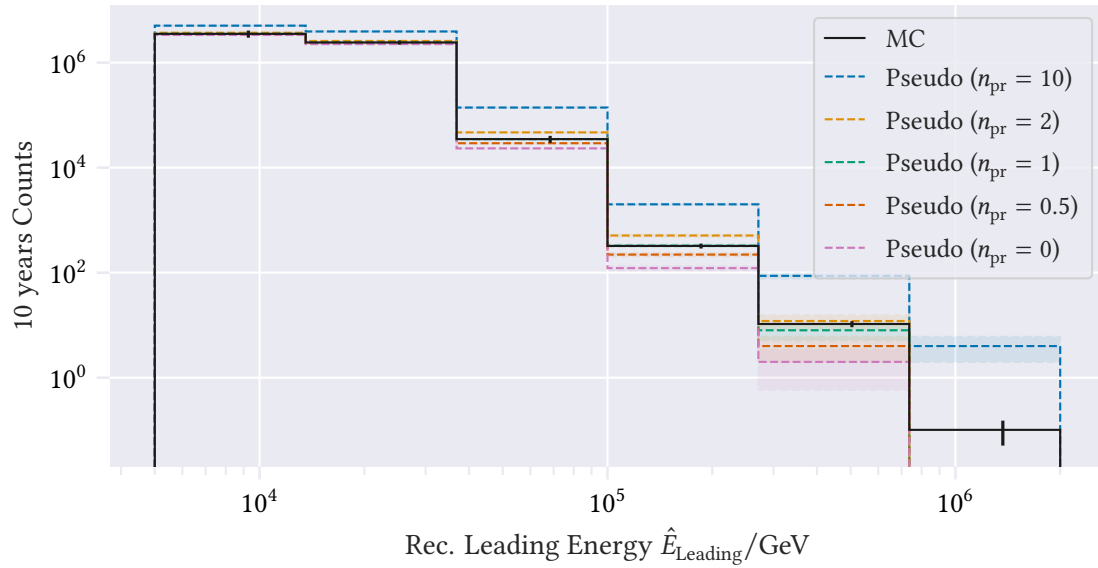
Figure C.14: The expected baseline MC distribution of the leading muon energy for 10 years of data, along with multiple pseudo data sets, sampled from the MC set with different strengths for the prompt component.

Glossary

CERN is the organisation that operates the largest particle physics laboratory in the world in Geneva on the France-Switzerland border. It operates the Large Hadron Collider (LHC), the most energetic particle accelerator in the world. They also invented the World Wide Web, let us thank them for that. 1

CMB cosmic microwave background. 7, 85

COM center of mass. 4, 31

CORSIKA7 is a Monte Carlo air shower simulation software written in `Fortran77`. Originally developed in the '80s for the KASCADE detector, it is now the de facto standard of air shower simulation software. (Acronym: **CO**smic **R**ay **SI**mulations for **KA**scade). iii, 2, 21–30, 33–38, 40, 47, 59, 67, 68

CORSIKA8 is a complete re-write of CORSIKA7 in C++. It is currently in early development and is expected to be released as a first public beta version later in 2023. Compared to its predecessor it will provide, among other enhancements, more flexibility and improved maintainability as well as a modern interface. 24, 30, 31

CR Cosmic Ray. 1, 3–7, 9, 17, 25, 26, 29, 31, 36, 38, 59, 72

DNN Deep Neural Network. 49–51

DOF degrees of freedom. 55

DOM Digital Optical Module. 2, 47, 49, 79, 80

EAS extensive air shower. 1–3, 8, 10–12, 18, 21, 24, 25, 29, 31, 38, 39, 47, 49, 59

EHISTORY extended history. 22–24, 26–30, 37, 41, 59, 68

EM electromagentic. 26, 27

GNN Graph Neural Network. 49

GSF Global Spline Fit. 4, 6, 7, 28, 33, 35, 36, 38, 44–46, 48, 50, 52, 53, 55, 57, 68–70, 73, 74, 76, 78, 79

GST Global Fit GST. 36, 78, 79

GZK The **G**reisen-**Z**atsepin-**K**uz'min cutoff is the hypothetical limit to the energy of cosmic rays at around 50 PeV due to the interaction with photons from the cosmic microwave background (CMB). 7

HGC The **H**adron **G**eneration **C**ounter tracks the number of hadronic interactions and decays in CORSIKA7. 22–24, 27, 68–70

IceCube is a km^3-sized observatory located in the glacier ice at the South Pole. It is the largest neutrino and muon-detector build to date . iii, 1, 2, 17, 22, 26, 39, 42, 47–50, 52, 57, 59, 60, 72–74, 77, 93

LHC Large Hadron Collider. 1, 29, 84

MC Monte Carlo. 2, 3, 8, 10, 18, 21, 22, 24, 25, 27, 29, 30, 32, 37–43, 47–52, 54–56, 59, 60, 72–83

MCEq is a python package that numerically solves the cascade equations to obtain e.g. Lepton fluxes from a given primary flux. (Acronym: **M**atrix**C**ascade**Eq**uations). iii, 11, 18–20, 22–25, 27–30, 32–37, 41, 47, 48, 59, 60, 77

PANAMA is an open source python package to facilitate the usage of CORSIKA7 [Nes23]. It allows to run CORSIKA7 on multiple cores, read the output into PANDAS' dataframes (using `pycorsikaio`[Lin23]), apply weighting to the simulation for multiple primary fluxes and parse the output of CORSIKA's EHIST option. (Acronym: **PAN**das **A**nd **M**ulti-Core Utils for CORSIKA7). iii, 22, 26, 35, 59

pid particle ID. 22–24

QCD Quantum Chromo Dynamics. 11, 31, 32

SNR supernova remnant. 4, 6

Bibliography

[Hes12]   V. F. Hess: "*Über Beobachtungen der durchdringenden Strahlung bei sieben Freiballon-fahrten*". In: *Phys. Z.* 13 (1912), pp. 1084–1091. `www.mpi-hd.mpg.de/hfm/HESS/public/HessArticle.pdf`.

[IC13]   The IceCube Collaboration (M. G. Aartsen et al.): "*Evidence for High-Energy Extraterrestrial Neutrinos at the IceCube Detector*". In: *Science* 342 (2013), p. 1242856. DOI: `10.1126/science.1242856`. arXiv: `1311.5238 [astro-ph.HE]`.

[LIG16]   The LIGO Scientific, Virgo Collaboration (B. P. Abbott et al.): "*Observation of Gravitational Waves from a Binary Black Hole Merger* ". In: *Phys. Rev. Lett.* 116.6 (2016), p. 061102. DOI: `10.1103/PhysRevLett.116.061102`. arXiv: `1602.03837 [gr-qc]`.

[Alv+19]   R. Alves Batista et al.: "*Open Questions in Cosmic-Ray Research at Ultrahigh Energies*". In: *Front. Astron. Space Sci.* 6 (2019), p. 23. DOI: `10.3389/fspas.2019.00023`. arXiv: `1903.06714 [astro-ph.HE]`.

[PA22]   The Pierre Auger Collaboration (P. Abreu et al.): "*Arrival Directions of Cosmic Rays above 32 EeV from Phase One of the Pierre Auger Observatory*". In: *Astrophys. J.* 935.2 (2022), p. 170. DOI: `10.3847/1538-4357/ac7d4e`. arXiv: `2206.13492 [astro-ph.HE]`.

[Alb+22]   J. Albrecht et al.: "*The Muon Puzzle in cosmic-ray induced air showers and its connection to the Large Hadron Collider*". In: *Astrophysics and Space Science* 367.3 (2022), p. 27. DOI: `10.1007/s10509-022-04054-5`.

[MG23]   The Muon g-2 Collaboration (D. P. Aguillard et al.): "*Measurement of the Positive Muon Anomalous Magnetic Moment to 0.20 ppm*". In: (Aug. 2023). arXiv: `2308.06230 [hep-ex]`.

[Aoy+20]   T. Aoyama et al.: "*The anomalous magnetic moment of the muon in the Standard Model*". In: *Physics Reports* 887 (2020). The anomalous magnetic moment of the muon in the Standard Model, pp. 1–166. ISSN: 0370-1573. DOI: `10.1016/j.physrep.2020.07.006`. `www.sciencedirect.com/science/article/pii/S0370157320302556`.

[NA37]   S. H. Neddermeyer and C. D. Anderson: "*Note on the Nature of Cosmic Ray Particles*". In: *Phys. Rev.* 51 (1937), pp. 884–886. DOI: `10.1103/PhysRev.51.884`.

[IC18]   The IceCube Collaboration (M. G. Aartsen et al.): "*Neutrino emission from the direction of the blazar TXS 0506+056 prior to the IceCube-170922A alert*". In: *Science* 361.6398 (2018), pp. 147–151. DOI: 10.1126/science.aat2890. arXiv: 1807.08794 [astro-ph.HE].

[MM18]   The IceCube, Fermi-LAT, MAGIC, AGILE, ASAS-SN, HAWC, H.E.S.S., INTEGRAL, Kanata, Kiso, Kapteyn, Liverpool Telescope, Subaru, Swift NuSTAR, VERITAS, VLA/17B-403 Collaboration (M. G. Aartsen et al.): "*Multimessenger observations of a flaring blazar coincident with high-energy neutrino IceCube-170922A*". In: *Science* 361.6398 (2018), eaat1378. DOI: 10.1126/science.aat1378. arXiv: 1807.08816 [astro-ph.HE].

[IC22]   The IceCube Collaboration (R. Abbasi et al.): "*Evidence for neutrino emission from the nearby active galaxy NGC 1068*". In: *Science* 378.6619 (2022), pp. 538–543. DOI: 10.1126/science.abg3395. arXiv: 2211.09972 [astro-ph.HE].

[IC23a]   The IceCube Collaboration (R. Abbasi et al.): "*Observation of high-energy neutrinos from the Galactic plane*". In: *Science* 380.6652 (2023), pp. 1338–1343. DOI: 10.1126/science.adc9818.

[IC17]   The IceCube Collaboration (M. Aartsen et al.): "*The IceCube Neutrino Observatory: instrumentation and online systems*". In: *Journal of Instrumentation* 12.03 (Mar. 2017), P03012–P03012. DOI: 10.1088/1748-0221/12/03/p03012. doi.org/10.1088%2F1748-0221%2F12%2F03%2Fp03012.

[Rei20]   R. Reimann: "*Search for the sources of the astrophysical high-energy muon-neutrino flux with the IceCube neutrino observatory*". In: (2020). publications.rwth-aachen.de/record/773297.

[Dem+17]   H. Dembinski et al.: "*Data-driven model of the cosmic-ray flux and mass composition from 10 GeV to 10^{11} GeV*". 2017. arXiv: 1711.11432 [astro-ph.HE].

[GER16]   T. K. Gaisser, R. Engel, and E. Resconi: "*Cosmic Rays and Particle Physics*". 2nd ed. Cambridge University Press, 2016. DOI: 10.1017/CBO9781139192194.

[Bir+95]   D. J. Bird et al.: "*Detection of a cosmic ray with measured energy well beyond the expected spectral cutoff due to cosmic microwave radiation*". In: *The Astrophysical Journal* 441 (Mar. 1995), p. 144. DOI: 10.1086/175344.

[Hal22]   F. Halzen: "*The observation of high-energy neutrinos from the cosmos: Lessons learned for multimessenger astronomy*". In: *Int. J. Mod. Phys. D* 31.03 (2022), p. 2230003. DOI: 10.1142/9789811269776_0004. arXiv: 2110.01687 [astro-ph.HE].

[Fer49]   E. Fermi: "*On the origin of the cosmic radiation*". In: *Physical review* 75.8 (1949), p. 1169. journals.aps.org/pr/pdf/10.1103/PhysRev.75.1169.

[TIG96]   M. Thunman, G. Ingelman, and P. Gondolo: "*Charm production and high-energy atmospheric muon and neutrino fluxes*". In: *Astropart. Phys.* 5 (1996), pp. 309–332. DOI: 10.1016/0927-6505(96)00033-3. arXiv: hep-ph/9505417.

[Hör03]   J. R. Hörandel: "*On the knee in the energy spectrum of cosmic rays*". In: *Astroparticle Physics* 19.2 (2003), pp. 193–220. ISSN: 0927-6505. DOI: `doi.org/10.1016/S0927-6505(02)00198-6`. `www.sciencedirect.com/science/article/pii/S0927650502001986`.

[PA07]   The Pierre Auger Collaboration (J. Abraham et al.): "*Correlation of the highest energy cosmic rays with nearby extragalactic objects*". In: *Science* 318 (2007), pp. 938–943. DOI: `10.1126/science.1151124`. arXiv: `0711.2256 [astro-ph]`.

[JF12]   R. Jansson and G. R. Farrar: "*A New Model of the Galactic Magnetic Field*". In: *Astrophys. J.* 757 (2012), p. 14. DOI: `10.1088/0004-637X/757/1/14`. arXiv: `1204.3662 [astro-ph.GA]`.

[Pet61]   B. Peters: "*Primary cosmic radiation and extensive air showers*". In: *Il Nuovo Cimento* 22.4 (Nov. 1961), pp. 800–819. DOI: `10.1007/BF02783106`.

[Gai12]   T. K. Gaisser: "*Spectrum of cosmic-ray nucleons, kaon production, and the atmospheric muon charge ratio*". In: *Astroparticle Physics* 35.12 (July 2012), pp. 801–806. DOI: `10.1016/j.astropartphys.2012.02.010`.

[Hil06]   A. M. Hillas: "*Cosmic Rays: Recent Progress and some Current Questions*". 2006. arXiv: `astro-ph/0607109 [astro-ph]`.

[GST13]   T. K. Gaisser, T. Stanev, and S. Tilav: "*Cosmic Ray Energy Spectrum from Measurements of Air Showers*". 2013. arXiv: `1303.3565 [astro-ph.HE]`.

[Gre66]   K. Greisen: "*End to the cosmic ray spectrum?*" In: *Phys. Rev. Lett.* 16 (1966), pp. 748–750. DOI: `10.1103/PhysRevLett.16.748`.

[ZK66]   G. T. Zatsepin and V. A. Kuzmin: "*Upper limit of the spectrum of cosmic rays*". In: *JETP Lett.* 4 (1966). `http://jetpletters.ru/ps/1624/article_24846.pdf`, pp. 78–80.

[ABG11]   R. Aloisio, V. Berezinsky, and A. Gazizov: "*Ultra high energy cosmic rays: The disappointing model*". In: *Astroparticle Physics* 34.8 (Mar. 2011), pp. 620–626. DOI: `10.1016/j.astropartphys.2010.12.008`.

[Hei36]   W. Heitler: "*The quantum theory of radiation*". Vol. 5. International Series of Monographs on Physics. Oxford: Oxford University Press, 1936.

[Mat05]   J. Matthews: "*A Heitler model of extensive air showers*". In: *Astroparticle Physics* 22.5 (2005), pp. 387–397. ISSN: 0927-6505. DOI: `10.1016/j.astropartphys.2004.09.003`.

[GEV18]   S. Grimm, R. Engel, and D. Veberic: "*Heitler-Matthews model with leading-particle effect*". In: *PoS* (2018), p. 299. `s3.cern.ch/inspire-prod-files-b/b39cb824e0b6d73b69ac4610b1789500`.

[Mon14]   J. Montanus: "*An extended Heitler–Matthews model for the full hadronic cascade in cosmic air showers*". In: *Astroparticle Physics* 59 (2014), pp. 4–11. ISSN: 0927-6505. DOI: `10.1016/j.astropartphys.2014.03.010`. `www.sciencedirect.com/science/article/pii/S0927650514000383`.

[KFK23]   T. Kozynets, A. Fedynitch, and D. J. Koskinen: "*Angular distributions of atmospheric leptons via two-dimensional matrix cascade equations*". In: *PoS* ICRC2023 (2023), p. 516. DOI: `10.22323/1.444.0516`.

[Fed15]   A. Fedynitch: "*Cascade equations and hadronic interactions at very high energies*". PhD thesis. KIT, Karlsruhe, Dept. Phys., 2015. `cds.cern.ch/record/2231593/files/CERN-THESIS-2015-371.pdf`.

[PDG22]   The Particle Data Group Collaboration (R. L. Workman et al.): "*Review of Particle Physics*". In: *PTEP* 2022 (2022), p. 083C01. DOI: `10.1093/ptep/ptac097`.

[Fed+15] A. Fedynitch et al.: "*Calculation of conventional and prompt lepton fluxes at very high energy*". 2015. arXiv: `1503.00544 [hep-ph]`.

[Fey69]   R. P. Feynman: "*Very High-Energy Collisions of Hadrons*". In: *Phys. Rev. Lett.* 23 (24 Dec. 1969), pp. 1415–1417. DOI: `10.1103/PhysRevLett.23.1415`.

[GMS15]   M. V. Garzelli, S. Moch, and G. Sigl: "*Lepton fluxes from atmospheric charm revisited*". In: *Journal of High Energy Physics* 2015.10 (Oct. 2015). DOI: `10.1007/jhep10(2015)115`.

[Bha+15] A. Bhattacharya et al.: "*Perturbative charm production and the prompt atmospheric neutrino flux in light of RHIC and LHC*". In: *Journal of High Energy Physics* 2015.6 (June 2015). DOI: `10.1007/jhep06(2015)110`.

[Bai+22] W. Bai et al.: "*Forward production of prompt neutrinos from charm in the atmosphere and at high energy colliders*". In: (Dec. 2022). arXiv: `2212.07865 [hep-ph]`.

[RD]   Í. Rapp-Arrarás and J. M. Domingo-Santos: "*Functional forms for approximating the relative optical air mass*". In: *Journal of Geophysical Research: Atmospheres* 116.D24 (). DOI: `10.1029/2011JD016706`.

[LHCb22] The LHCb Collaboration (R. Aaij et al.): "*Measurement of prompt charged-particle production in pp collisions at a centre-of-mass energy of 13 TeV*". In: *Journal of High Energy Physics* 2022.1 (Jan. 2022). DOI: `10.1007/jhep01(2022)166`.

[US 93]   U.S. Department of Energy: "*DOE Fundamentals Handbook*". Vol. 1. Jan. 1993. `www.navsea.navy.mil/Portals/103/Documents/NNPTC/Physics/doe_phys_nuc.pdf`.

[Meß22]   J. Meßner: "*High-energy atmospheric muons with IceCube-Gen2*". Bachelorthesis. 2022.

[Nes23]   L. Neste: "*PANAMA (**PAN**das **A**nd **M**ulti-Core Utils for CORSIK**A**7)*". Version 0.5.5. July 28, 2023. `github.com/the-ludwig/panama`.

[Lin23]   M. Linnhoff: "*pycorsikaio*". Version 0.3.3. July 29, 2023. `github.com/cta-observatory/pycorsikaio`.

[IC23b]   The IceCube Collaboration (K. Meagher): "*IceTray*". Version 1.7.1. Aug. 1, 2023. `github.com/icecube/icetray-public`.

[KH93]   J. Knapp and D. Heck: "*Extensive Air Shower Simulation with CORSIKA: A User's Manual*". Kernforschungszentrum Karlsruhe, 1993. `web.iap.kit.edu/corsika/usersguide/usersguide.pdf` (visited on 07/22/2020).

[HE13]   D. Heck and R. Engel: "*The EHISTORY and MUPROD Options of the Air Shower Simulation Program CORSIKA*". Tech. rep. Karlsruher Institut für Technologie (KIT), 2013. DOI: `10.5445/IR/1000034601`.

[RU19]   M. Reininghaus and R. Ulrich: "*CORSIKA 8 – Towards a modern framework for the simulation of extensive air showers*". In: *EPJ Web of Conferences* 210 (2019). Ed. by I. Lhenry-Yvon et al., p. 02011. DOI: `10.1051/epjconf/201921002011`.

[HR23]   T. Huege and M. Reininghaus: "*The particle-shower simulation code CORSIKA 8*". 2023. arXiv: `2308.05475 [astro-ph.HE]`.

[Eng+19]   R. Engel et al.: "*Towards a next generation of CORSIKA: a framework for the simulation of particle cascades in astroparticle physics*". In: *Computing and Software for Big Science* 3 (2019), pp. 1–12. DOI: `10.1007/s41781-018-0013-0`.

[RUP21]   M. Reininghaus, R. Ulrich, and T. Pierog: "*Air shower genealogy for muon production*". In: *Proceedings of 37th International Cosmic Ray Conference — PoS(ICRC2021)*. Sissa Medialab, July 2021. DOI: `10.22323/1.395.0463`. `doi.org/10.22323%2F1.395.0463`.

[Rei23]   M. Reininghaus: "*Air shower genealogy*". DPG SMuK23. 2023. `www.dpg-verhandlungen.de/year/2023/conference/smuk/part/t/session/92/contribution/6`.

[IC23c]   The IceCube Collaboration (K. Meagher, K. Rawlins, and L. Neste): "*SimWeights: Pure python library for calculating the weights of Monte Carlo simulation for IceCube.*" Version 0.1.1. Aug. 1, 2023. `github.com/icecube/simweights`.

[KU12]   K.-H. Kampert and M. Unger: "*Measurements of the cosmic ray composition with air shower experiments*". In: *Astroparticle Physics* 35.10 (2012), pp. 660–678. ISSN: 0927-6505. DOI: `10.1016/j.astropartphys.2012.02.004`.

[Bug+89]   E. V. Bugaev et al.: "*Prompt Leptons in Cosmic Rays*". In: *Nuovo Cim. C* 12 (1989), pp. 41–73. DOI: `10.1007/BF02509070`.

[Bug+98]   E. V. Bugaev et al.: "*Atmospheric muon flux at sea level, underground and underwater*". In: *Phys. Rev. D* 58 (1998), p. 054001. DOI: `10.1103/PhysRevD.58.054001`. arXiv: `hep-ph/9803488`.

[Ill+11]   J. I. Illana et al.: "*Atmospheric lepton fluxes at very high energy*". In: *Astropart. Phys.* 34 (2011), pp. 663–673. DOI: `10.1016/j.astropartphys.2011.01.001`. arXiv: `1010.5084 [astro-ph.HE]`.

[Fed+19]   A. Fedynitch et al.: "*Hadronic interaction model Sibyll-2.3c and inclusive lepton fluxes*". In: *Physical Review D* 100.10 (Nov. 2019). DOI: `10.1103/physrevd.100.103018`.

[Rie+20]   F. Riehn et al.: "*Hadronic interaction model Sibyll 2.3d and extensive air showers*". In: *Phys. Rev. D* 102.6 (2020), p. 063002. DOI: `10.1103/PhysRevD.102.063002`. arXiv: `1912.03300 [hep-ph]`.

[LHCb16]   The LHCb Collaboration (R. Aaij et al.): "*Measurements of prompt charm production cross-sections in pp collisions at $\sqrt{s} = 13$ TeV*". In: *JHEP* 03 (2016). [Erratum: JHEP 09, 013 (2016), Erratum: JHEP 05, 074 (2017)], p. 159. DOI: `10.1007/JHEP03(2016)159`. arXiv: `1510.01707 [hep-ex]`.

[RS]   E. Rodrigues and H. Schreiner: "*Particle*". DOI: `10.5281/zenodo.2552429`. `github.com/scikit-hep/particle`.

[Baa16]   D. Baack: "*Data Reduction for CORSIKA*". Tech. rep. 2. E5b, Faculty Physic, TU Dortmund, June 2016. `github.com/tudo-astroparticlephysics/Cor-Plus Plus`.

[Wil38]   S. S. Wilks: "*The Large-Sample Distribution of the Likelihood Ratio for Testing Composite Hypotheses*". In: *The Annals of Mathematical Statistics* 9.1 (1938), pp. 60–62. DOI: `10.1214/aoms/1177732360`.

[Koe+13]   J.-H. Koehne et al.: "*PROPOSAL: A tool for propagation of charged leptons*". In: *Computer Physics Communications* 184.9 (2013), pp. 2070–2090. DOI: `10.1016/j.cpc.2013.04.001`.

[IC19]   The IceCube Collaboration (M. Aartsen et al.): "*Efficient propagation of systematic uncertainties from calibration to analysis with the SnowStorm method in IceCube*". In: *Journal of Cosmology and Astroparticle Physics* 2019.10 (Oct. 2019), pp. 048–048. DOI: `10.1088/1475-7516/2019/10/048`.

[Søg+23]   A. Søgaard et al.: "*GraphNeT: Graph neural networks for neutrino telescope event reconstruction*". In: *Journal of Open Source Software* 8.85 (2023), p. 4971. DOI: `10.21105/joss.04971`.

[Hue23]   M. Huennefeld: "*icecube/dnn_reco*". Version v1.0.1. June 2023. DOI: `10.5281/zenodo.8003189`.

[IC21]   The IceCube Collaboration (R. Abbasi et al.): "*A convolutional neural network based cascade reconstruction for the IceCube Neutrino Observatory*". In: *Journal of Instrumentation* 16.07 (July 2021), P07041. ISSN: 1748-0221. DOI: `10.1088/1748-0221/16/07/p07041`.

[Bra23]   B. Brandt: "*A deep learning based angular reconstruction of atmospheric muons in IceCube*". Bachelorthesis. 2023.

[Flo23]   L. Flottau: "*A deep learning based reconstruction of high-energetic muons in IceCube*". Bachelorthesis. 2023.

[ASR88]   M. Abramowitz, I. A. Stegun, and R. H. Romer: "*Handbook of mathematical functions with formulas, graphs, and mathematical tables*". 1988. `personal.math.ubc.ca/~cbm/aands/frameindex.htm`.

[IC16]   The IceCube Collaboration (M. Aartsen et al.): "*Characterization of the atmospheric muon flux in IceCube*". In: *Astroparticle Physics* 78 (May 2016), pp. 1–27. DOI: `10.1016/j.astropartphys.2016.01.006`.

[Ahn+09]   E.-J. Ahn et al.: "*Cosmic ray interaction event generator SIBYLL 2.1*". In: *Phys. Rev. D* 80 (2009), p. 094003. DOI: `10.1103/PhysRevD.80.094003`. arXiv: `0906.4113 [hep-ph]`.

Acknowledgments

Eidesstattliche Versicherung

(Affidavit)

Neste, Ludwig

Name, Vorname
(surname, first name)

205317

Matrikelnummer
(student ID number)

☐ Bachelorarbeit
(Bachelor's thesis)

☑ Masterarbeit
(Master's thesis)

Titel
(Title)

Prompt Atmospheric Muons: An Analysis Concept with IceCube

Ich versichere hiermit an Eides statt, dass ich die vorliegende Abschlussarbeit mit dem oben genannten Titel selbstständig und ohne unzulässige fremde Hilfe erbracht habe. Ich habe keine anderen als die angegebenen Quellen und Hilfsmittel benutzt sowie wörtliche und sinngemäße Zitate kenntlich gemacht. Die Arbeit hat in gleicher oder ähnlicher Form noch keiner Prüfungsbehörde vorgelegen.

I declare in lieu of oath that I have completed the present thesis with the above-mentioned title independently and without any unauthorized assistance. I have not used any other sources or aids than the ones listed and have documented quotations and paraphrases as such. The thesis in its current or similar version has not been submitted to an auditing institution before.

Dortmund, 30.09.2023

Ort, Datum
(place, date)

Unterschrift
(signature)

Belehrung:
Wer vorsätzlich gegen eine die Täuschung über Prüfungsleistungen betreffende Regelung einer Hochschulprüfungsordnung verstößt, handelt ordnungswidrig. Die Ordnungswidrigkeit kann mit einer Geldbuße von bis zu 50.000,00 € geahndet werden. Zuständige Verwaltungsbehörde für die Verfolgung und Ahndung von Ordnungswidrigkeiten ist der Kanzler/die Kanzlerin der Technischen Universität Dortmund. Im Falle eines mehrfachen oder sonstigen schwerwiegenden Täuschungsversuches kann der Prüfling zudem exmatrikuliert werden. (§ 63 Abs. 5 Hochschulgesetz - HG -).

Die Abgabe einer falschen Versicherung an Eides statt wird mit Freiheitsstrafe bis zu 3 Jahren oder mit Geldstrafe bestraft.

Die Technische Universität Dortmund wird ggf. elektronische Vergleichswerkzeuge (wie z.B. die Software „turnitin") zur Überprüfung von Ordnungswidrigkeiten in Prüfungsverfahren nutzen.

Die oben stehende Belehrung habe ich zur Kenntnis genommen:

Official notification:
Any person who intentionally breaches any regulation of university examination regulations relating to deception in examination performance is acting improperly. This offense can be punished with a fine of up to EUR 50,000.00. The competent administrative authority for the pursuit and prosecution of offenses of this type is the Chancellor of TU Dortmund University. In the case of multiple or other serious attempts at deception, the examinee can also be unenrolled, Section 63 (5) North Rhine-Westphalia Higher Education Act (*Hochschulgesetz, HG*).
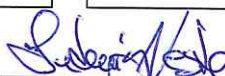
The submission of a false affidavit will be punished with a prison sentence of up to three years or a fine.

As may be necessary, TU Dortmund University will make use of electronic plagiarism-prevention tools (e.g. the "turnitin" service) in order to monitor violations during the examination procedures.

I have taken note of the above official notification:*

Dortmund, 30.09.2023

Ort, Datum
(place, date)

Unterschrift
(signature)

*Please be aware that solely the German version of the affidavit ("Eidesstattliche Versicherung") for the Bachelor's/ Master's thesis is the official and legally binding version.